Molecular layer deposition and protein interface patterning for guided cell growth

Manuel Glass

Schlüsseltechnologien / Key Technologies
Band / Volume 215
ISBN 978-3-95806-463-8

Mitglied der Helmholtz-Gemeinschaft

JÜLICH
Forschungszentrum

Schriften des Forschungszentrums Jülich
Reihe Schlüsseltechnologien / Key Technologies Band / Volume 215

Forschungszentrum Jülich GmbH
Institute of Complex Systems
Bioelectronics (ICS-8)

Molecular layer deposition and protein interface patterning for guided cell growth

Manuel Glass

Schriften des Forschungszentrums Jülich
Reihe Schlüsseltechnologien / Key Technologies Band / Volume 215

ISSN 1866-1807 ISBN 978-3-95806-463-8

Bibliografische Information der Deutschen Nationalbibliothek.
Die Deutsche Nationalbibliothek verzeichnet diese Publikation in der
Deutschen Nationalbibliografie; detaillierte Bibliografische Daten
sind im Internet über http://dnb.d-nb.de abrufbar.

Herausgeber und Vertrieb:	Forschungszentrum Jülich GmbH Zentralbibliothek, Verlag 52425 Jülich Tel.: +49 2461 61-5368 Fax: +49 2461 61-6103 zb-publikation@fz-juelich.de www.fz-juelich.de/zb
Umschlaggestaltung:	Grafische Medien, Forschungszentrum Jülich GmbH
Druck:	Grafische Medien, Forschungszentrum Jülich GmbH
Copyright:	Forschungszentrum Jülich 2020

Schriften des Forschungszentrums Jülich
Reihe Schlüsseltechnologien / Key Technologies, Band / Volume 215

D 38 (Master Köln, Univ., 2020)

ISSN 1866-1807
ISBN 978-3-95806-463-8

Vollständig frei verfügbar über das Publikationsportal des Forschungszentrums Jülich (JuSER)
unter www.fz-juelich.de/zb/openaccess.

Abstract

This thesis describes the design, assembly and structural and functional characterization, of bio-(medical) applicable interfacial layers with molecular controlled architectures on solid substrates. The interaction between the living world of cells, tissue, or whole organisms and the (organic or inorganic) materials world of technical devices such as implants, sensors, or medical parts requires a proper construction and detailed structural (and functional) control of this organism-machine interface. Therefore, a possible way how to get from an optimal molecular layer deposition (MLD) to guided cell growth is developed in this work.

By integrating a heater to an already existing MLD setup and an optimization of the deposition temperature we could improve the gas phase deposition process of GLYMO (3-Glycidyloxypropyl)-trimethoxysilane) yielding a faster formation of self-assembled monolayers (SAMs) and a better quality of GLYMO SAMs. This was confirmed by ex-situ analysis, e.g. fluorescence microscopy, referenced ellipsometry, and surface potential measurements.

With the gas phase MLD, lithography, and lift-off processes functionalization of SiO_2 surfaces with GLYMO SAMs and patterned ploy-L-lysine proteins (PLL) could be achieved. This enables to generate various micropatterns that support cell adhesion, neurite outgrowth, and the formation of a geometrically defined networks of neurons.

Finally, guided growth was demonstrated via rat cortical neuron cultures on the GLYMO-PLL patterned surfaces. On first sight, the neuron growth was clearly guided, i.e. neurons grow on PLL but not on GLYMO. However, we also noticed that on certain areas which should be coated with PLL, no cells were present. It seemed that in these areas during the lithography PMMA is cracked due to the e-beam exposure and partially binds to the GLYMO. This cracked PMMA hinders the PLL to bind to GLYMO and therefore only in places, where PLL dries out during the coating, PLL is present in the GLYMO-PLL pattern. These effects are observed via fluorescence imaging for the PLL coating and for the cell growth.

In conclusion, the modified deposition process at elevated temperatures in combination with the developed interface pattering process via a combination of a molecular layer of GLYMO and the protein PLL might be suitable for guidance of neuronal growth, despite the problem of a PMMA blocking layer which seem to be generated during the lithography. This shortcoming could be overcome by an additional step in which the blocking layer is remove.

Index of Abbreviations

APTES	(3-Aminopropyl)-triethoxysilane
DIV	Days in vitro
DP	Deposition pressure
DT	Deposition time
GIXD	Grazing incidence X-ray diffraction
GLYMO	(3-Glycidyloxypropyl)-trimethoxysilane
MLD	Molecular layer deposition
PDT	Post deposition treatment
PLL	Poly-L-lysine
RSE	Referenced spectroscopic ellipsometry
RT	Room temperature
SAM	Self-assembled monolayer
SEM	Scanning electron microscopy
SHG	Second harmonic generation
SSO	SiO_2 terminated Si

Contents

1 Introduction

Throughout history, mankind has tried - successful or less successful - to “repair” or replace damaged or diseased parts of the human body in order to repair and restore its functionality. Implant materials used were for instance selected according to its availability and with the devoping understanding of the concept of biocompatibility and its suitability. Nowdays we can see the evolution of new concepts and the next generation of biomaterials.

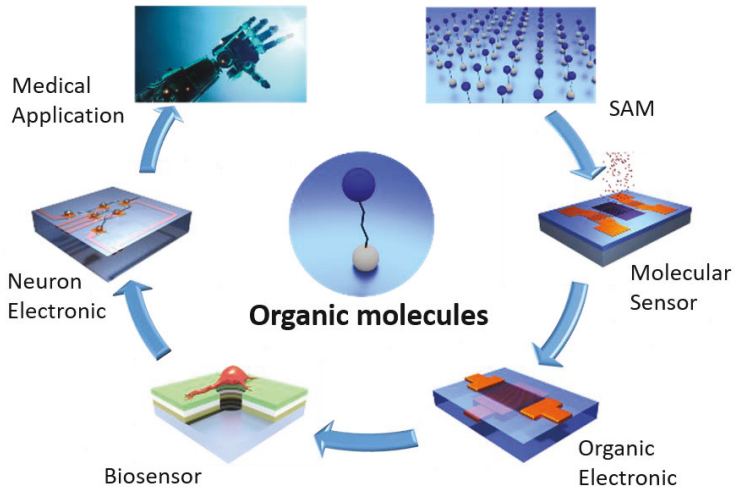

Figure 1: Development of bioelectronic application. From simple layers to complex medical applications.

The first traces of attempts to repair and replace parts of the body date back several thousand years, long before understanding the concepts of sterilization or biocompatibility. The materials used to replace body parts have changed throughout history, from seashells in the Mayan period to commercial materials such as polymers, metals and ceramics in the time of the surgery after the Second World War to technical materials developed for biological applications in modern times. Here we find silicones, hydrogels and bio-functional materials like molecular nanostructures. The latter is typically based on polymers, synthetic membranes or other nanoscale self-assembled monolayers and is functionalized with biomolecules such as proteins, peptides or other organic molecule compositions. These (supra)molecular systems and materials will not only be useful as implant coatings in tissue engineering and regenerative medicine, but they can also be used for the development of bioelectronic interfaces and in the field of hybrid systems that can function as biofuel cells, biosensors and biocomputing devices. These molecular nanostructures might help to solve some of today's biomedical challenges and might represent a next generation of bio and medical application due to their potential for application-specific tailoring and tuning of their properties.

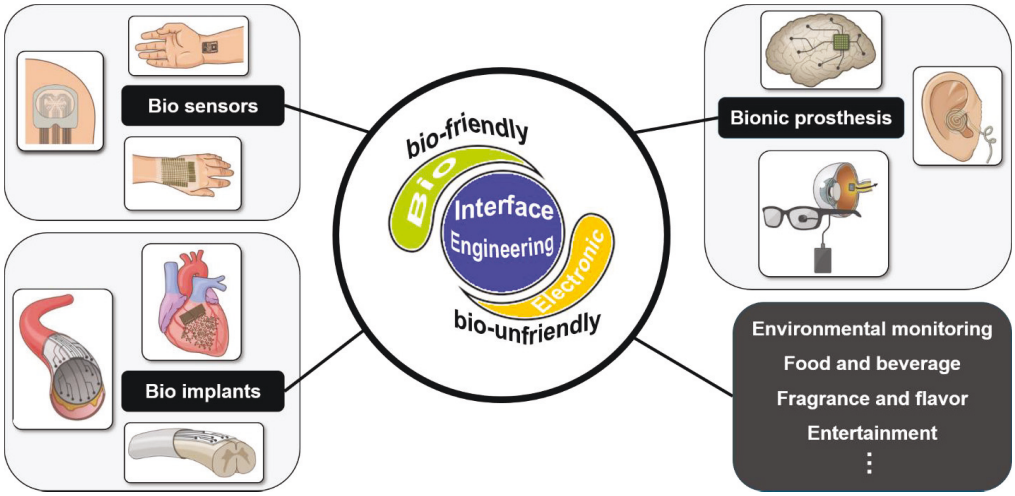

Figure 2: Generic overview of bioelectronic applications ranging from biosensors, bioimplants and bionic prosthesis to other commercial applications such as environmental monitoring [36].

In order to design these molecular structures in a controlled fashion, however, it is necessary to understand the buildup process of molecular nanoscale assemblies, and to characterize the material properties as a function of the process parameters themself. This work should contribute to this knowledge. With our molecular layer deposition setup, used and optimized in this work, the buildup of the materials can be controlled and monitored. The resulting layers can be characterized by various ex situ methods as a function of different deposition characteristics (e.g. temperature, pressure, deposition time). The diverse technologies used in this research enable the evaluation of functional effects of, for example, subsequent cell adhesion and guided cell growth.

To put it in a nutshell, the aims of this thesis are:

- Optimization of an existing molecular layer deposition setup to achieve a better quality of the produced layer and tailor these layers toward bio application
- Development of a patterning process that allows guided cell growth based on the molecular layers

Therefore,

- **Chapter 2** provides a basic introduction to the physics behind self-assembled monolayers.
- **Chapter 3** explains the different experimental methods:
    i. referenced spectroscopic ellipsometry
    ii. fluorescence microscopy
    iii. surface potential measurement
    iv. and sample production steps.

The results are organized in three separate chapters:

- **Chapter 4** shows the benefit of the heater for the gas phase deposition (in terms of layer quality) and the deposition of self-assembled monolayers of GLYMO on SiO_2 surfaces.
- **Chapter 5** analyzes the lithography and lift-off technique for protein (PLL) patterned films sample on self-assembled monolayer.
- **Chapter 6**, finally, demonstrates the biocompatibility versus toxicity of the patterned layers and, furthermore, studies the resulting guided neuronal cell growth.

As a last point

- **Chapter 7** provides a summary.

2 Theoretical Background

In this chapter I provide a short introduction to the theoretical background of possible intermolecular bonds and their bonds to oxide surfaces. Beforehand, I briefly give a definition of self-assembled monolayers, the silane (3-Glycidyloxypropyl)-trimethoxysilane (GLYMO) is described and its interaction with Poly-L-Lysine (PLL) is explained and the impact of temperature on the SAM formation is discussed.

2.1 Self-Assembled Monolayer (SAM)

A self-assembled monolayer (SAM) consists of highly ordered molecules which form a monolayer of a thickness of several Ångström. The molecules of such a layer consist of a functional group, a backbone and a head group (Figure 3 (a)). Since after deposition of a SAM the new surface is defined by the functional group of the molecules, its properties (e.g. wetting angle, surface potential, reactivity, etc.) are modified. This makes molecular monolayers a powerful tool to alter the surface of a substrate and make it, for instance, suitable for cell cultures [1]. The functional group can also be used to prove the existence of the SAM or to bind to a second layer which could for instance be a protein. Via a chain called backbone the functional group is connected to the head group (Figure 3 (a)). The backbone typically consists of a hydrocarbon chain. The backbone interacts with the adjacent molecules via Van der Waals force (Figure 3 (b)), with a typically interaction of several kJ/mol for each CH_2 unit cell [2].

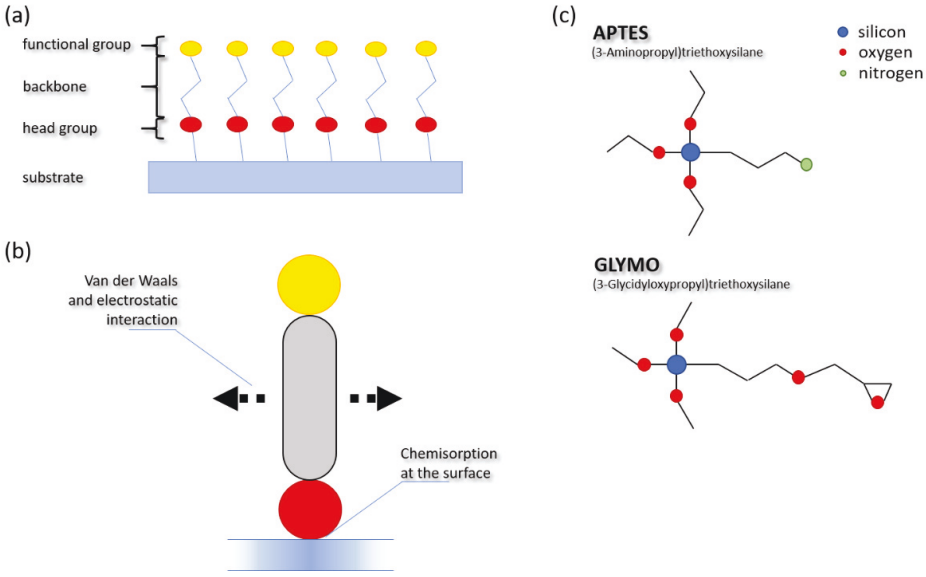

Figure 3: Schematics of (a) self-assembled molecules, (b) inter molecular forces and their bond to the surface, and (c) the molecules GLYMO and APTES.

The head group is very important since it connects the molecules to the substrate surface. The head group should bind chemically (covalently) to surfaces with a binding energy of several hundred kJ/mol. Depending on the substrate, an appropriate head group should be selected. The substrates used in this thesis are SiO_2 (≈ 25 nm) terminated Si (SSO) and the molecule is the silane GLYMO ((3-Glycidyloxypropyl)-trimethoxysilane) with a head group that binds to SiO_2. The functional group of GLYMO is ethylene oxide, an epoxy group (Figure 3 (c)). GLYMO is very similar to another silane, APTES ((3-Aminopropyl)-triethoxysilane), which is widely used for fabrication of SAMs [3] [4] [5] [6] [7] [8] [9]. The chemical structure (Figure 3 (c)) and some physical properties (size, weight, evaporation point) of APTES are very similar to that of GLYMO. Therefore, in some cases APTES is used for comparison with GLYMO in this thesis.

2.2 Binding Interaction

In Figure 4 (a)-(c) the different options for the binding of molecules to the substrate are sketched. In reality, molecules connect to a surface in different ways (Figure 4 (d)) [3].

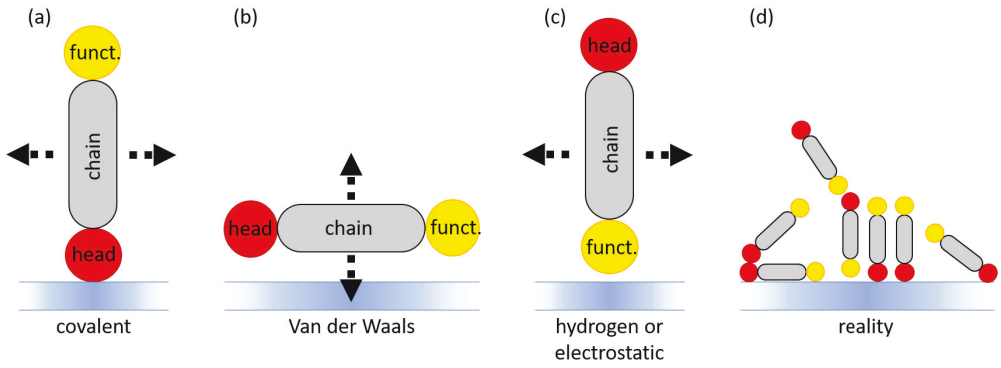

Figure 4: Binding options of self-assembled molecules; head, chain, and funct. symbolizes the head group, chain, and functional group of the molecule.

The possible binding interactions that are relevant in this thesis are:

i. **Van der Waals force:** The weakest of the atomic bonding interaction is the Van der Waals force (0.4-4.0 kJ/mol). It occurs between atoms or molecules whose valence shells are completely occupied by electrons (e.g. noble gases), because repeatedly dipole moments are generated and destroyed due to the fluctuations of their electron shells. A dipole moment is introduced due to fluctuations into an adjacent atom. This atom then induces a dipole moment in the first on, so that the dipole moments no longer fluctuate and stabilize.

ii. **Ionic bonds:** The generation of an ion bond requires electron affinity on the one hand and ionization energy on the other. If the ionization energy for one atom is lower (i.e. electrons can be easily removed from the atom) and another atom has a high electron affinity (i.e. additional electrons bind easily to these atoms to fill their electron shells), both atoms can attract to each other. So, the ionic bond is based on the electrostatic interaction between oppositely charged ions. In molecular deposition, the substrate surface and the head group of the molecule should be oppositely charged. The interaction is typically of the order of ≈ 20 kJ/mol.

iii. **Covalent bonds:** For covalently bonded atoms the valence electrons are shared, therefore new electron orbitals are built. The shared electrons create an attractive force of typically >60 kJ/mol. Covalently bonded molecules are non-conductive because the conductance requires free or displaced electrons. Only exceptions are conjugated covalent bonds (e.g. graphene) [10].

iv. **Hydrogen bonds:** Hydrogen bonds are a combination of ionic and covalent bonds. When a covalent bond is formed between an atom of high electronegativity (e.g., oxygen or nitrogen) and hydrogen, hydrogen almost completely donates the electron. The result is a positively charged hydrogen to which a second electronegative atom can ionically bind if it has previously been covalently bound to another atom. Only two atoms can be connected by a hydrogen bond due to the size of the proton [10]. The strength of the hydrogen bond is about 12-30 kJ/mol.

For completeness, a fifth interaction between atoms should be mentioned, the metallic bond. This bonding will not be explained in this work, since this binding force is not relevant in our experiments.

2.3 GLYMO and PLL

The epoxy silane GLYMO ((3-Glycidyloxypropyl)trimethoxysilane) (Figure 5) is an organofunctional trialkoxysilane that leads to a surface dominated by epoxide rings. GLYMO can be covalently attached to the hydroxyl group (silanol after activation) of SiO_2 under the release of methanol. Epoxysilane coating is a perfect method for immobilizing proteins (and DNA) onto the solid surface. The coupling mechanism relies on the fact that epoxide rings are high reactive towards amino groups [11].

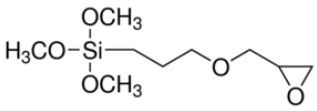

Figure 5: Chemical structure of GLYMO.

Amino groups can be found on functional targets in form of N-termini of proteins, or as side chains of certain amino acid residues (e.g. Lysine). Under physiologic conditions the amino groups carry

a positive charge and are therefore usually facing outwards of the globular protein structure, making them accessible for the coupling reaction [12]. During the incubation most proteins will form a covalent bond with the ring structure of the epoxysilane [12].

Poly-L-Lysine (PLL), sketched in Figure 6, is a synthetic molecule that increase cell adhesion by altering the net charge of the surface without stimulating biological activity. PLL is a synthetic molecule and is therefore free of potential impurities of biological origin. Applications include cultivation of transfected cells and fastidious cell lines, serum-free or serum-reduced cell culture and general improvement of cell binding e.g. during washing steps. In addition, PLL improves the survival of many neuronal cells in culture.

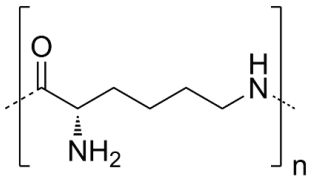

Figure 6: Chemical structure of PLL.

Since the GLYMO epoxysilane, due to the epoxy rings as a functional group, is toxic to cells and the positively charged biofriendly amino acid chain PLL, binds covalently to the functional group of GLYMO, this actually enables options to use GLYMO for a guided cell growth. The contrast between a toxic epoxysilane coating with GLYMO in combination with an additional coating with the highly biofriendly PLL offers a simple way to direct the cell growth. Based on these considerations the interface patterning via a combination of a molecular layers of GLYMO and PLL for guided cell growth is one of the final aims of this thesis.

2.4 Temperature related Issus

The driving forces for the self-organization of organic adsorbates on surfaces are synergistic interaction between

(1) Interface interaction
(2) intermolecular tail-tail interactions and
(3) headgroup-substrate interaction

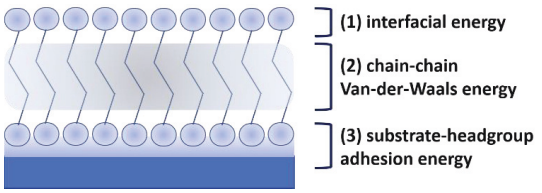

Figure 7: SAM energetic, synergies between substrate-headgroup interactions, intermolecular chain-chain interactions and interfacial energy changes determine the arrangement and equilibrium structure of well packed SAMs.

associated with the formation of a monolayer phase interface [13]. In Figure 7 the three classes of energetic contributions to monolayer organization are sketched. Although this general description of thermodynamics is widely accepted, details of how the synergy between these energetic factors determines the densest, near-equilibrium structure are still discussed [5] [3].

For the exemplary case of alkanethiols on an Au surface, the strong metal-sulfur interaction (Au-S) of ≈ 45 Kcal/mol serves as the primary determinant for self-organization. This is reinforced by intermolecular tail-tail interactions. Lateral Van der Waals interactions between the aliphatic chains result in ≈ 1.5 kcal/mol per methylene (CH_2) group in the chain. An additional stabilization

results from the surface energy changes resulting from the exposure of the functional group at the interface between air. These interaction energies drive the order of organosulfur compounds at the Au surface.

However, many SAMs can be produced from both solution and gas phase. Gas phase growth generally requires a more expensive experimental setup (i.e. normally a vacuum chamber etc.), but also offers some advantages, such as better control of the cleanliness of the environment, substrate and substances and their respective temperatures, and the applicability of in situ experiments. Because of these advantages and the reproducibility of high-quality film, the gas phase deposition method was used in this work. The control parameters (temperature, pressure, time, etc.) in the gas phase deposition play a crucial role in the SAM formation of organosAulfides and organosilanes [14]. Therefore, a thorough analysis of the SAM system of organosilanes on oxide substrates has certainly to include the effect of temperature. Generally, upon increasing the temperature of the molecules and substrates, different processes can occur (e.g. phase transition, desorption, or dissociation of the molecules). Additionally, at moderate temperatures, temperature annealing effects such as defect healing or domain size growth may be important. Furthermore, the relative distribution of covalent bonds, hydrogen bonds and electrostatic interactions might change under the influence of heat.

Moreover, it has often been reported that the first adsorption step provides coverage of 80 % to 90 %, typically on a time scale in the order of minutes. To describe the surface coverage $\Theta(t)$, in a first approximation, the Langmuir growth curve can be taken, which is characterized by the growth rate $R(T,p)$ being proportional to the number of available sites:

$$\frac{d\Theta}{dt} = R(T,p)(1-\Theta(t))$$

which gives rise to the simple growth law:

$$\Theta(\mathrm{t}) = 1 - e^{R(T,p)\cdot t} \qquad 2\text{-}1$$

An example is shown in Figure 8.

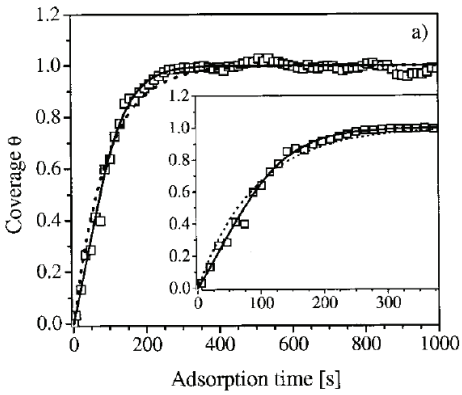

Figure 8: Dodecanthiol from hexane solution evaporated on Au film. The dotted line corresponds to the simple Langmuir growth (2-1). Somewhat better fits (solid line) include small modifications of the model. Taken from [35].

The dependence on the control parameter Temperature T which is related to growth rate $R(T,p)$ and furthermore to the surface coverage is therefore very important, and for GLYMO gas-phase deposition on SSO will be analyzed in this thesis.

In order to contribute to a more fundamental understanding, the investigation of these temperature-related issues are of great importance for any SAM-based technological application.

3 Experimental Methods

In this chapter, the “GLOBUS” setup, developed for molecular layer deposition, the extension of the setup:

- an optical heater
- a corresponding temperature sensor (the design and lithography of the sensor)

and the additional ex-situ methods:

- Reference Spectroscopic Ellipsometry (RSE)
- Fluorescence Microscopy
- Surface potential measurement device “SurPASS”

for characterizing the molecular layers, are described.

Furthermore, the interface patterning process which combines a molecular layer deposition of GLYMO in combination with patterned coating with PLL for guided cell growth is introduced. Finally, information about the neuron culturing process are given.

3.1 Chemical Cleaning of Samples

The cleaning of the sample surface is important because the formation of SAMs on the substrate depends strongly on the surface quality [6].

i. Firstly, the substrates are cleaned 5 minutes in acetone (≥99.9%, Sigma-Aldrich) in an ultrasonic bath (highest power).

ii. Secondly, they are cleaned 5 minutes in isopropyl alcohol (2-propanol, ≥99.5%, Sigma-Aldrich) in an ultrasonic bath (highest power).

iii. Finally, the substrates are dried with nitrogen.

3.2 Gas-phase Deposition (MLD) Setup GLOBUS

The main deposition device for this research work is the MLD setup GLOBUS. This device is under constant development to improve its variability, precision and capability for MLD processes.

It consists mainly of glass to prevent a chemical reaction with the deposited molecules that can occur with many metals. It is also important to reduce the internal surface area, since vaporized molecules can condense at any small unevenness and glass tends to minimize its surface roughness and thus the total surface to which molecules can bind.

GLOBUS can be divided into three parts:

i. the ozone generator for the activation process,
ii. the deposition chamber in which the deposition takes place and
iii. the molecular sources.

Further parts include inlets for nitrogen gas connection and oxygen gas and a pump system consisting of valve, prepump and turbopump. The extension of the setup which was added during this work includes an optical heater and a corresponding temperature sensor (described in chapter 3.3). This extension enables depositions at elevated temperatures ranging from room temperatures to approx. 125°C.

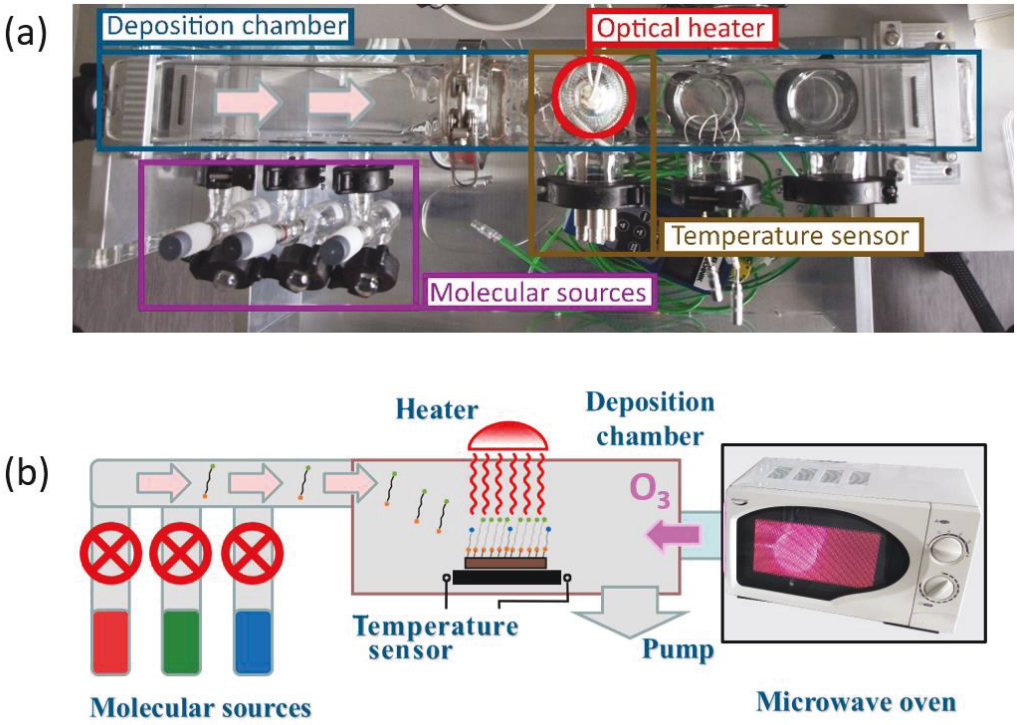

Figure 9: MLD setup GLOBUS for SAM deposition from the gas phase without breaking the vacuum: (a) Image of the GLOBUS system with deposition chamber, molecular sources and optical heater (with temperature sensor). (b) schematic presentation of the GLOBUS with the optical heater directly placed over the samples and the temperature sensor beneath.

The setup is automated using a computer and a proprietary LabVIEW program. The complete deposition process can be subdivided into three parts:

i. firstly activation,
ii. subsequently deposition and
iii. the post deposition treatment.

These steps are described in the section below.

3.2.1 Activation and Silanization

Silanization consists of grafting a layer of silane molecules onto a surface. Silanes are categorized based on their functional end group. In this thesis, a layer of epoxy silane (GLYMO) are created onto a SiO_2 surface. After the chemical cleaning with acetone and isopropyl alcohol of the samples, the activation process is carried out with ozone generated by a microwave oven. This leads to further cleaning and removal of unwanted molecules from the substrates and for the silanization needed activation process. The microwave works maximum power (800 W) for 3 minutes. Ozone, a strong oxidizing agent, reacts with organic molecules on the surface and removes them. It also reacts with the SiO_2 surface. During the activation, the ozone removes oxygen in the SiO_2 top layer which leads to a reconstruction of the silanol surface bonds. The reaction is as follows:

$$SiO_2 + O_3 \rightarrow SiO + 2O_2$$

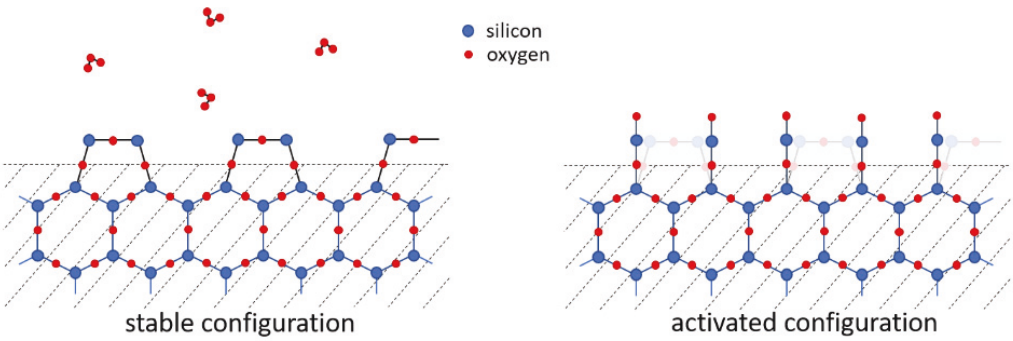

Figure 10: Schematic of the ozone activation process of the SiO_2 surface.

The result is a freshly "activated" structure at the surface as sketched in Figure 10. The free Si-O bonds are not stable and decay to the more stable Si-O-Si bonds in a time of approx. 2 ½ days (chapter 4.3). The SiO_2 surface is activated in order to enhance the binding probability of silanes and thus enables a coverage of the surface with the organic molecules. Examples for a GLYMO deposition after activation are given in Figure 11.

Activation with an oxygen plasma could lead in the ideal case to a homogeneous and dense covering of the SiO_2 surface with silanes. However, recent research on silanes have pointed out that the binding process at the surface is much more complicated [15] [16]. There is always a distribution of covalent bonds, hydrogen bonds and electrostatic interactions. Furthermore, there exists an extent of cross-linking among the silane molecules. In few words, various bindings are possible (comparison Figure 11) and this strongly depends on the deposition process parameters themselves.

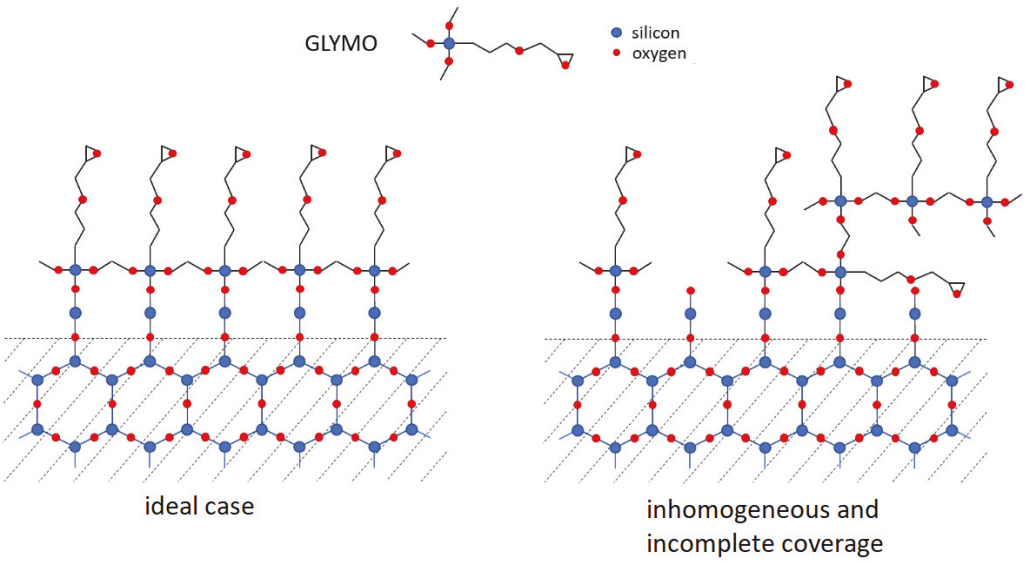

Figure 11: Sketch of a GLYMO deposition after activation. Left, the ideal case of a homogeneous and dense coverage with GLYMO. Right, example of an inhomogeneous and incomplete coverage with GLYMO.

At this point APTES shall be used for comparison with GLYMO. In a recent publication of M. Zhu et al [15] different types of interactions between APTES molecules and silicon dioxide substrates are stated (see Figure 12). This group carried out silanization in anhydrous toluene and as well in the vapor phase at elevated temperatures. They quote that aminosilane-derived layers prepared in solution are multilayers in nature, and those produced in the vapor phase have monolayer characteristics. This emphasizes our approach to gas phase deposition of GLYMO.

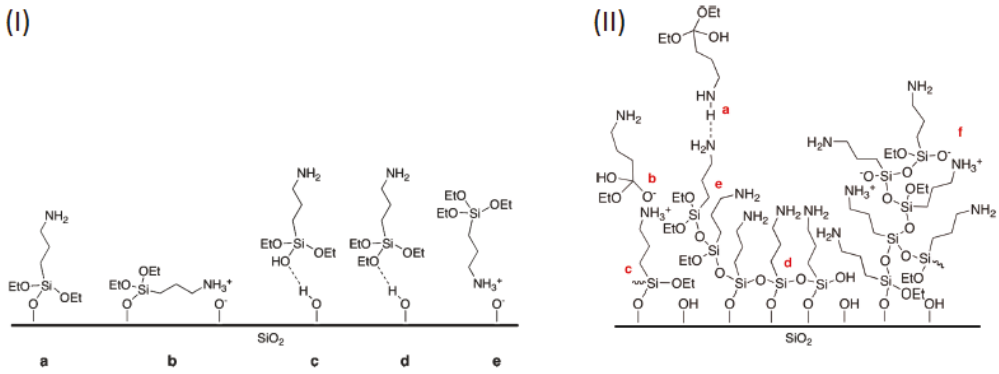

Figure 12: Taken from [15]. (I) Different types of interactions between APTES molecules and SiO_2 substrates: (a) a covalently attached APTES molecule with its amine group extending away from the interface, (b) a covalently attached APTES molecule with its amine group interacting with a surface silanol group, and (c-e) weakly bounded APTES molecules. (II) An APTES-derived layer with structural irregularities: individual silane molecules can be incorporated into the layer via (a) hydrogen bonding, (b) electrostatic attraction, (c) covalent bonding with the substrate, and (d) horizontal and (e) vertical polymerization with neighboring silanes; (f) oligomeric/polymeric silanes can also react/interact with functionalities present at the interface.

3.2.2 Complete Deposition Procedure

The following table gives an overview of the standard deposition process which is established in our work group in comparison with the modified deposition process which is used in this thesis.

step	Standard Deposition	New Process
1	inserting the samples and pumping the system to 10^{-5} mbar	
2	applying oxygen flow (100 sccm) to 0.9 mbar for the ozone generator	
3	starting the microwave for ozone cleaning and activation (3 min, 800 W)	
4	applying nitrogen flow (30 sccm) to the DP: (0.1 mbar)	applying nitrogen flow (110 sccm) DP: (0.9 mbar)
5	deposition start by opening the GLYMO source for 1 hour and **at room temperature**	deposition start by opening the GLYMO source for 1 hour and **heater on for 2 hours**
7	Deposition stop by closing GLYMO source (DT: 1 hour)	
8	stop nitrogen flow (**PDT: 24 h at 10^{-5} mbar & room temp**.)	(**PDT: 1 h at 0.9 mbar & elevated temp.**) heater off after 2 hours
9	removing sample (**process time ≈ 25 h**)	removing sample (**process time ≈ 2 h**)

In summary, the differences between the two deposition processes are:

	Standard Deposition	New Process
DP	0.1 mbar	0.9 mbar
DT	1 hour	1 hour
PDT	24 hours	1 hour
Temperature	RT	from RT to 125°C

Thus, the modified process is much faster due to the elevated process temperature.

3.3 Optical Heater & Temperature Sensor for the MLD

The deposition device used in this research work is the MLD setup GLOBUS. This device is under constant development, the extension of the setup which was added during this work includes an optical heater and a sample carrier connected with a specially designed temperature sensor for in-situ temperature measurement. The sensor itself is generated by lithography and lift-off technology in the Helmholtz Nano Facility (HNF).

3.3.1 Overview of the Extensions

The extensions added to the GLOBUS system to implement a controlled heating and in-situ temperature measuring system include the three following parts:

i. a sample and temperature sensor holder
ii. an optical heater and
iii. a temperature sensor.

The temperature sensor is mounted to the sample holder, which also serves as an electrical conductor. The holder is connected to a KF40 vacuum flange with coaxial feedthroughs (with BNC connections) and added to the GLOBUS system. The samples are placed directly on the temperature sensor. The holder offers space for four 10 mm x 10 mm samples. Detailed pictures of all parts are given in Figure 13.

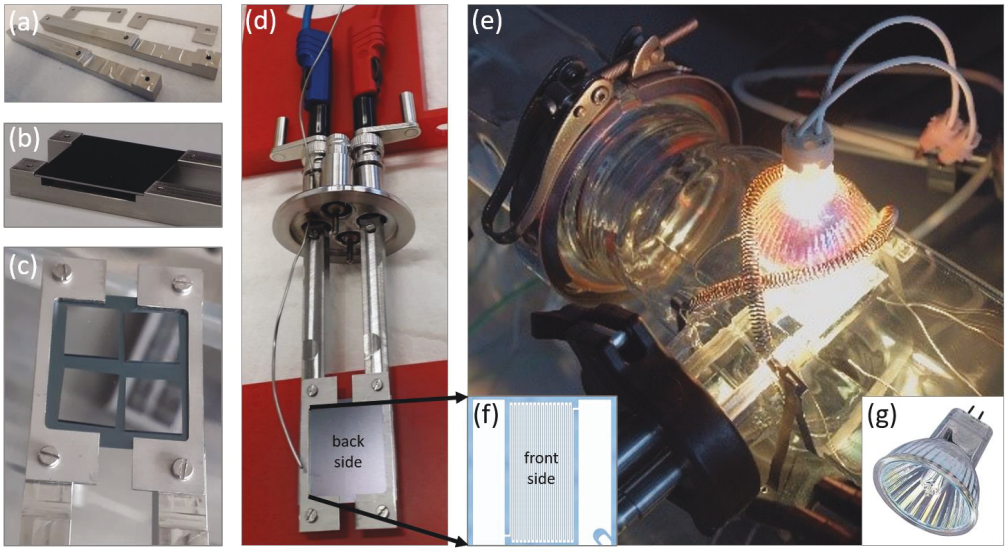

Figure 13: (a) Sample and temperature sensor holder, (b) temperature sensor mounted upside down on the sample holder to guarantee a small and defined contact area with the holder, (c) mounted sample holder with 4 SSO samples placed directly on the temperature sensor (sensor upside down), (d) complete system connected to KF 40 flange (e) system mounted into GLOBUS with optical heater in operation, (f) temperature sensor and (g) optical heater (from Osram®)

3.3.2 E-beam Lithography

The institute uses two different lithography methods, electron beam lithography and optical lithography. Due to its high flexibility, electron beam lithography is a better choice for our purpose. The resolution of the electron beam lithography is down to 10 nm [17]. Depending on the method, optical lithography has a 10-100 times lower resolution.

To improve the accuracy of the electron beam lithography for future projects, its electron energy has been recently increased from 50 keV to 100 keV. Therefore, the electron dose had to be adjusted for the new voltage of 100 keV. Hence, a small dose test is presented. First a test pattern sample was designed (Figure 14) including structures ranging from 3 µm to 1000 µm. This pattern is repeated 15 times deposited on a 10 mm x 10 mm SSO substrate and each pattern is exposed with different doses ranging from 360 µC/cm^2 to 920 µC/cm^2. The evaluation of the resulting structure is based on two different imaging methods, a first inspection with an optical microscope, followed by a SEM (scanning electron microscope) analysis. An overview of the pattern is given in Figure 14. The red box marks the spot of the picture, which was analyzed by optical microscopy for each dose.

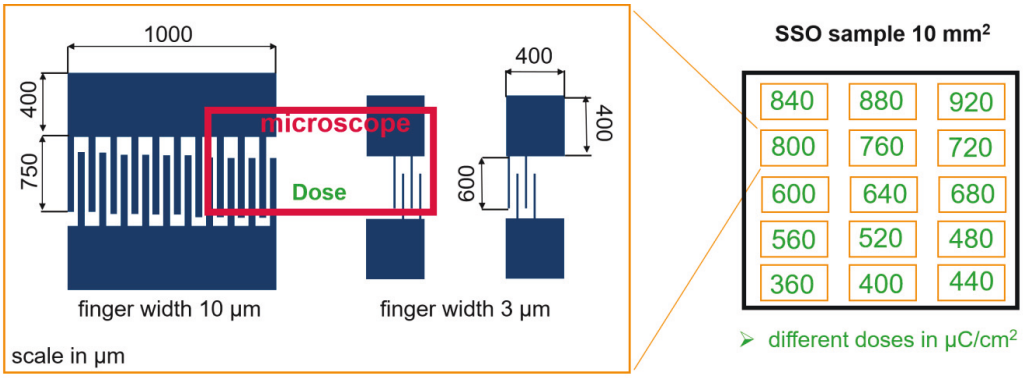

Figure 14: Dose test pattern design with pattern sizes ranging from 3 µm to 1000 µm. 15 different doses beginning from 360 µC/cm² to 920 µC/cm² were chosen. Structure deposited on SSO.

The dose test pattern is manufactured using electron beam lithography with 100 keV electron energy and Ti/Pt lift-off technique on the SSO substrate according to a special recipe. The different steps of the recipe are outlined in Figure 15 and described in detail next to it.

(1) **Cleaning**: The first step is to clean the surface. The SSO substrates are immersed for 5 minutes in an ultrasonic bath at highest performance in acetone. The process is repeated with propanol to remove the acetone.

(2) **Photoresist**: The photoresist poly(methyl methacrylate) (PMMA AR-P 669.07) is spin-coated onto the substrate at 4000 rpm for 60 s. The substrate should be completely covered with resist and the thickness of the PMMA should be about 700 nm. After spin-coating, the sample should be placed on a 120°C hot plate as quick as possible and left there for 30 min. On the way from the spin coater to the hot plate, the back of the substrate is brushed over acetone-soaked paper to prevent the sample from being burned onto the hot plate.

(3) **Electron-beam writing**: For e-beam writing, a mask is designed with AutoCAD or similar programs. The electron beam writer VISTEC EBPG 5000 plus is used. The e-beam cracks polymers in the PMMA at locations exposed to the beam. E-beam energy is 100 keV.

(4) **Development of PMMA**: The cracked polymers of PMMA are removed with a developer solution. Therefore, the sample are immersed for 90 s in the developer AR600-55. The sample then remains in propanol for 30 s. Subsequently, the sample is dried with nitrogen gas. Now only the inverted pattern is left over.

(5) **Ti/Pt deposition**: For the metallic structure, first Ti is deposited as an adhesive layer and then Pt on top. Both metals are evaporated and cover the PMMA and the open areas. The thickness of the Ti layer is 5 nm, the thickness of the Pt layer is 45 nm.

(6) **Lift-off**: To obtain the final structure, the PMMA with the Ti/Pt layer must be removed (lift-off). The sample is placed in acetone in an ultrasonic bath (lowest power) for 1 min. At the end, the acetone is removed with propanol (1 min ultrasonic bath lowest power) and dried with nitrogen gas. The final structure remains.

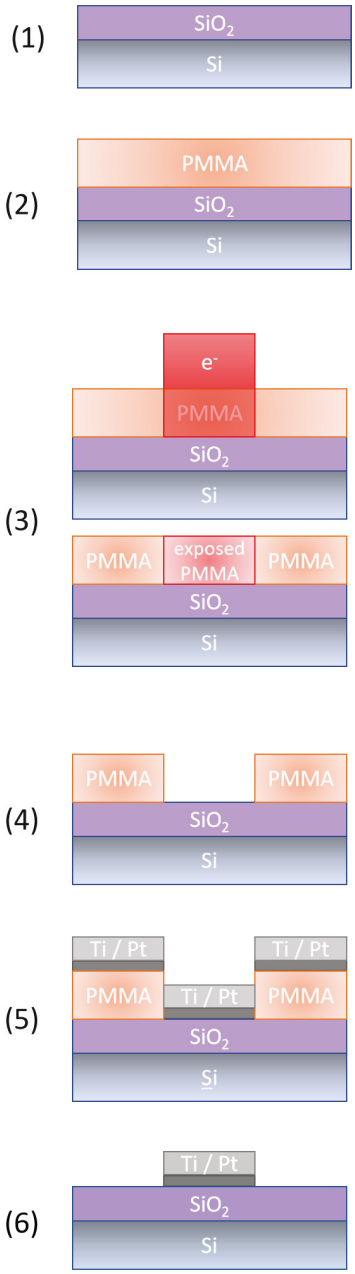

Figure 15: Sketch of the different steps of the sample preparation

After preparation a selection of the dose test pattern is shown in Figure 16.

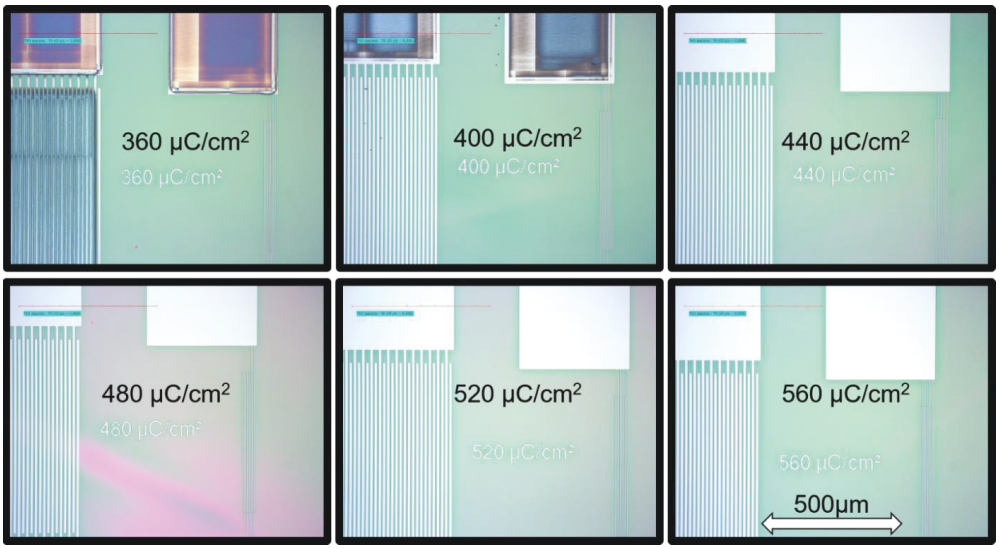

Figure 16: Optical microscope pictures of identical structures obtained for different doses of the 100 keV e-beam ranging from 360 µC/cm² to 560 µC/cm².

It is clearly visible that a dose below 440 µC/cm² is not sufficient to crack the polymer structure of the PMMA and generate a reasonable structure. In the big and even in the small structure PMMA is a left-over. 440 µC/cm² can be considered to be a minimum dose.

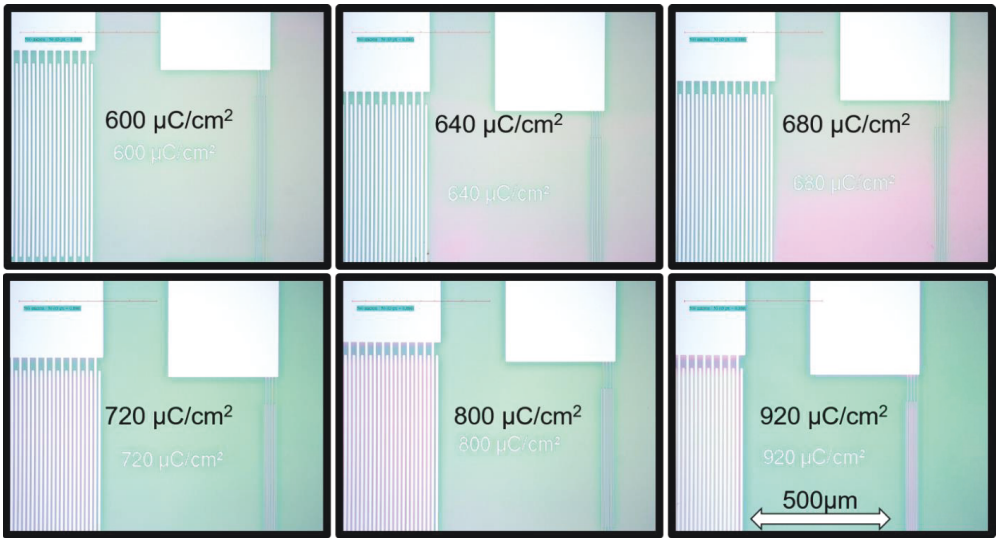

Figure 17: Optical microscope pictures of identical structures obtained for different doses of the 100 keV e-beam ranging from 600 µC/cm² to 920 µC/cm².

According to Figure 17 no upper limit for a suitable dose could be obtained via optical microscopy. The highest contrast and thus the cleanest demarcation of the structure was achieved with a dose between 440 µC/cm^2 and 560 µC/cm^2 as shown in a close-up in Figure 18

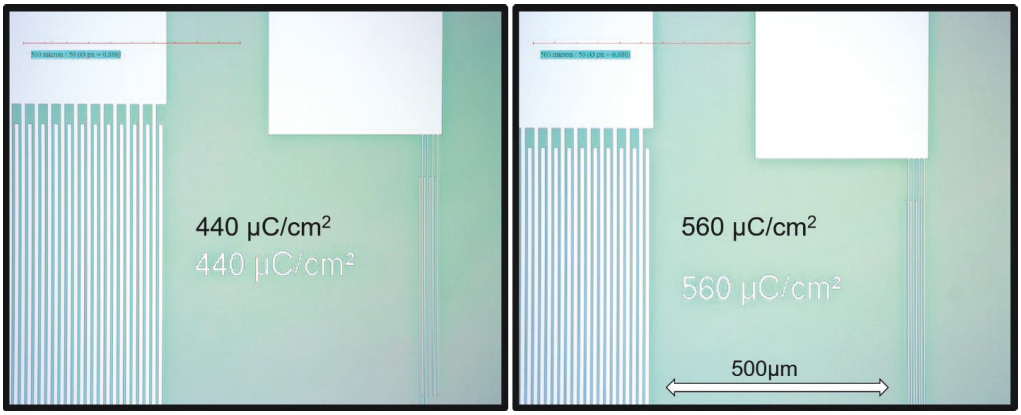

Figure 18: Optical microscope pictures with the highest contrast from identical structures generated with two different doses of 400 µC/cm² and 560 µC/cm².

With the use of the optical microscope we could set a lower limit of 440 µC/cm^2. With the SEM picture the width of the finger structure (nominal width 10 µm) were measured. Two examples are given in Figure 19.

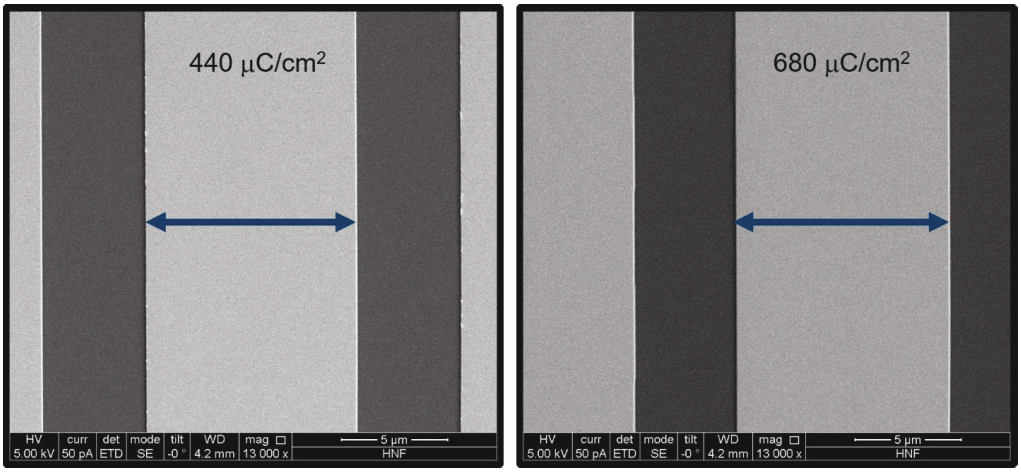

Figure 19: SEM pictures of the 10 µm fingers for two different e-beam doses, 440 µC/cm² and 680 µC/cm².

With the help of the SEM measurement, it could be shown that the fingers get broader with the dose of the e-beam (Figure 20). Below 500 µC/cm^2, the width is smaller than the nominal width of 10 µm and above 520 µC/cm^2, the width is larger than 10 µm. Considering the lower limit of 440 µC/cm^2 the best dose for structuring via e-beam lithography on SiO_2 terminated Si substrates seems to be 500 µC/cm^2. For the further lithography processes this dose was used and set as an optimum.

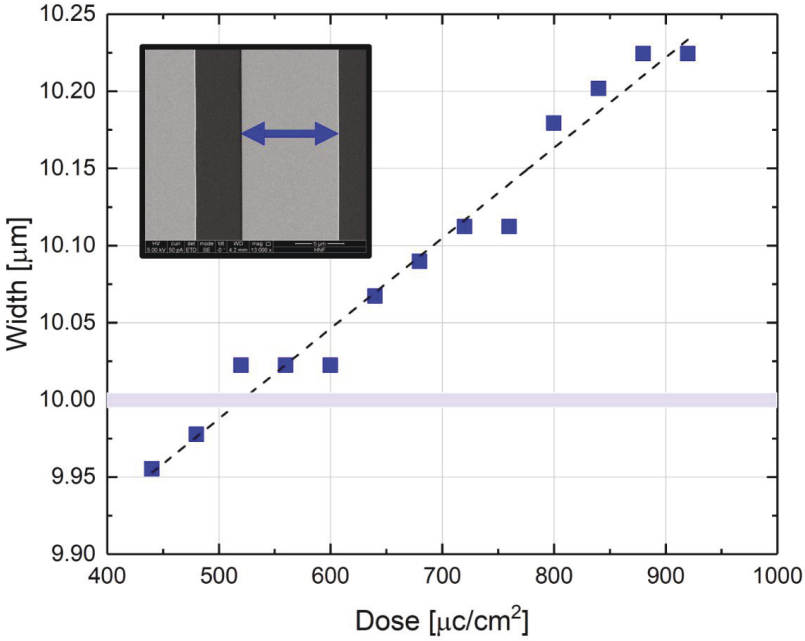

Figure 20: Finger width analyzed via SEM as a function of the dose. The nominal width is 10 µm. The dashed line displays the fit of the measured thickness values.

3.3.3 Temperature Sensor

The temperature sensor was manufactured using electron beam lithography and Ti/Pt lift-off technique on SSO (30 mm x 30 mm) according to the recipe introduced in the section before. For the sensor a special design was developed (using AutoCAD 2013) consisting of two 2.9 mm x 6.5 mm contact areas which are connected via a meander patterned line which has a width of 200 µm and length of ≈ 0.5 m (see Figure 21). The thickness of the sensor is 50 nm (5 nm Ti and 45

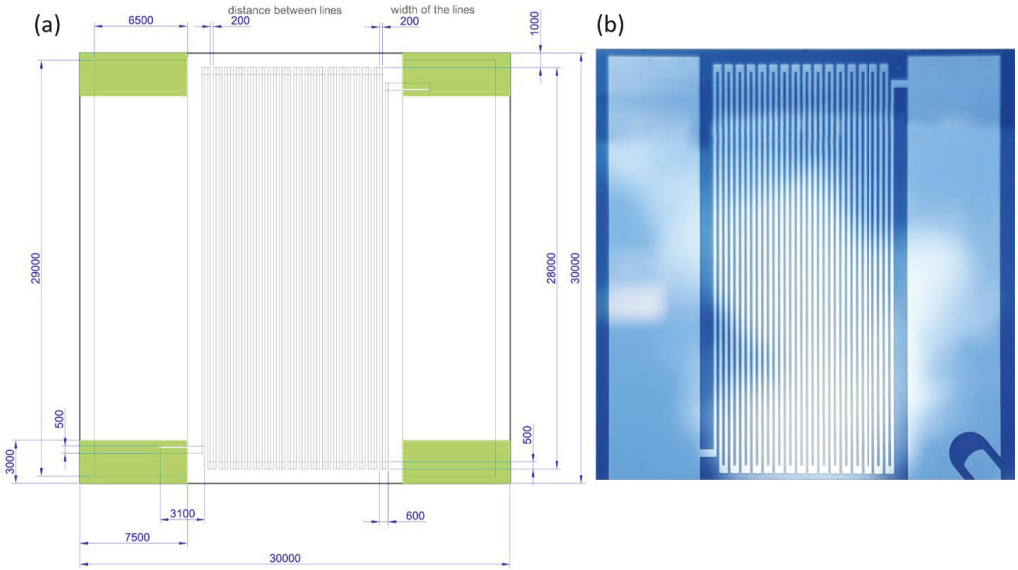

Figure 21: (a) AutoCAD design for the e-beam writing in µm scale (the green areas show the contact area to the holder), (b) the finished sensor with a size of 30 x 30 mm².

nm Pt). The green areas in the schematic (Figure 21 (a)) represent the contact area to the holder.

The meander design was chosen to achieve a high electrical resistance of the temperature sensor structure. The resistance R of a given material is proportional to the electrical resistivity ρ (of the material) and length l, but inversely proportional to the cross-sectional area A:

$$R = \rho(T) \cdot \frac{l}{A} \qquad 3\text{-}1$$

Since for Pt $\rho(T)$ is proportional to the temperature for $T \geq 100\,\mathrm{K}$, we can obtain the temperature of the sensor via a simple calibration. For a first approximation, we can use the electrical resistivity of Pt at room temperature ($\rho = 2.6 \cdot 10^{-7}\Omega\mathrm{m}$ [18]). With the length of the meander structure $l \approx 0.5\,\mathrm{m}$ and the cross-sectional area $A = 10^{-11}\mathrm{m}^2$, a nominal electrical resistance of $R \approx 13\,\mathrm{k}\Omega$ at room temperature is expected. This value is in good agreement with the actual measured value of $R \approx 16\,\mathrm{k}\Omega$, considering that in our case there is an additional titanium layer under the platinum layer (the specific electrical resistance of titanium is eight times higher than that of platinum [18]).

Nevertheless, the electrical resistance of the temperature sensor is the dominant part in the sensor setup, the resistance of holder, flange and wires can be set to zero in a first approximation. This is advantageous for the later calibration of the sensor and the associated in-situ temperature measurement, because the temperature measurement is then only determined by the linear resistance-vs.-temperature behavior of meander patterned Pt line.

3.3.4 Temperature Calibration

After the manufacturing of the temperature sensor, the sensor was annealed at 180 °C for 2 hours. Due to the increased mobility of the atoms at elevated temperatures, structural defects can be compensated, and the morphology of the Ti/Pt conductors can be improved. Since the temperature sensor is used in a range from room temperature to over 125 °C and the measurements must be reproducible, it is important that its linear behavior between temperature and electrical resistance of Pt does not change between measurements. To calibrate the temperature sensor, the electrical resistance at room temperature and at 100 °C was measured. For resistance measurement at 100 °C, the sensor was placed in a copper box (Figure 22) and heated for one hour to 100 °C. The box serves as thermal insulation. It is assumed that the sensor was fully in thermal equilibrium and thus the resistance value at 100 °C can be perfectly used for calibration.

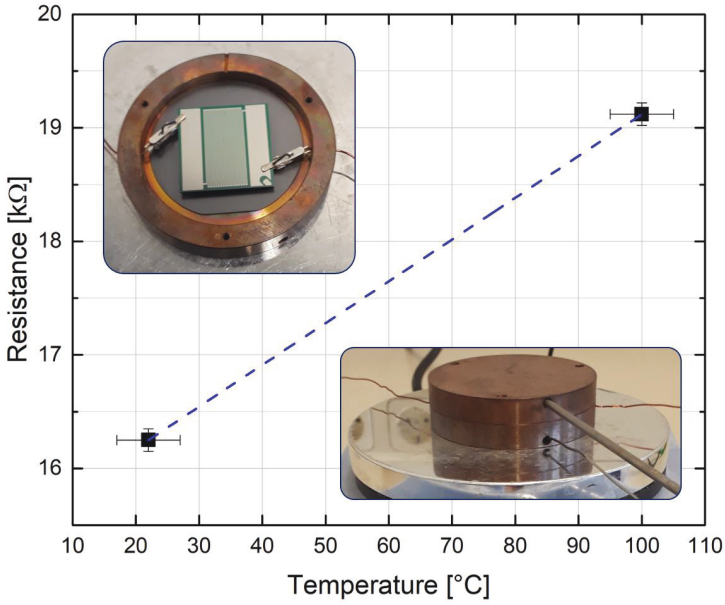

Figure 22: Calibration curve of the Ti/Pt temperature sensor. Electrical resistance as a linear function of the temperature. The photos show the copper box, in which the temperature sensor was stored for the resistance measurement at 100 °C

The resulting calibration curve is shown in Figure 22 and is described by a linear function.

$$R(T) = T \cdot 0.037\ {}^{\mathrm{k\Omega}}/_{^{\circ}\mathrm{C}} + 15.44\ \mathrm{k\Omega} \qquad 3\text{-}2$$

Following the calibration, the resulting temperature of the sensor is given by:

$$T(R) = \frac{R - 15.44\ \mathrm{k\Omega}}{0.037\ {}^{\mathrm{k\Omega}}/_{^{\circ}\mathrm{C}}} \qquad 3\text{-}3$$

In a next step, the optical heater was operated with three different powers and the resulting electrical resistance of the temperature sensor in GLOBUS at 0.9 mbar was measured (Figure 23). From this data, the maximal electrical resistance (respectively the maximal temperature) could be measured as a function of the heating power. The linear fit of the data Figure 23 (b) provides the dependence of the sensor temperature on the power P of the lamp:

$$T(P) = P \cdot 1.865\ {}^{^{\circ}\mathrm{C}}/_{\mathrm{W}} + 22.97\ ^{\circ}\mathrm{C} \qquad 3\text{-}4$$

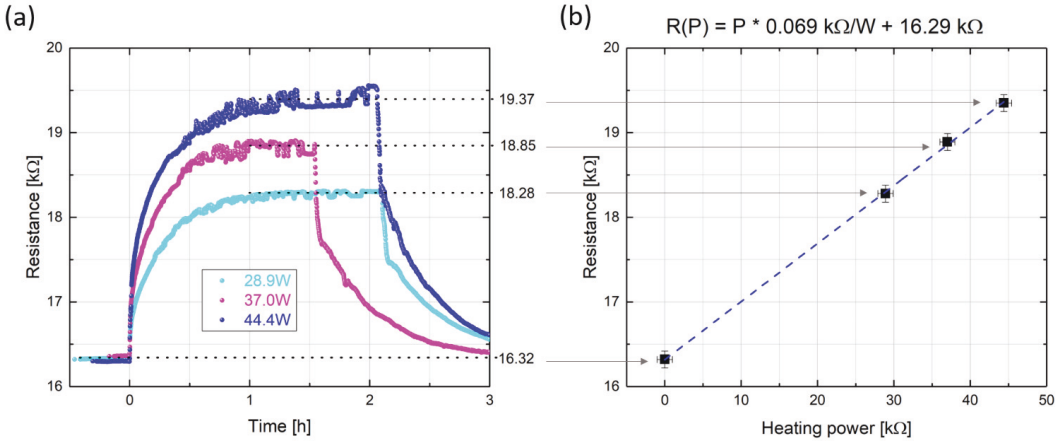

Figure 23: (a) Electrical resistance of the temperature sensor in the GLOBUS as a function of time for different heating powers. In all three cases, the maximum temperature plateau is reached after 1 hour. (b) Electrical resistance after temperature stabilization of the sensor as a function of heating power and linear fit of the data.

3.4 Ex-situ Analysis

Ex-situ measurements are necessary to analyze the self-organized monolayers. The following ex-situ methods, used for this thesis, are presented in this chapter.

i. Ellipsometry is a widely used techniques for characterizing the thickness of layers in general.
ii. The streaming potential technique is used to analyze the electronic properties of the molecular layers.
iii. Fluorescence microscopy is used to visualize PLL/FITC and neurons on the surface of the samples.

3.4.1 Referenced Spectroscopic Ellipsometry (RSE)

Ellipsometry is a very sensitive optical method that has been used to obtain information about surfaces for about a hundred years. It exploits the fact that the state of polarization of light can change when the light beam is reflected from a surface. If the surface is covered with a thin film, the entire optical system of film and substrate influences the change in polarization. It is therefore possible to derive information about the film properties, in particular the film thickness. Therefore, the referenced spectroscopic ellipsometer "*nanofilm_rse"* made by ACCURION GmbH was used (Figure 24).

Figure 24: Photo of the referenced spectroscopic ellipsometer nanofilm_rse (ACCURION GmbH).

As said, the RSE is a special ellipsometer type that compares the sample with a reference. In this way, the ellipsometric difference between sample and reference can be measured. Due to the orientation of the reference, none of the optical components have to be moved or modulated during the measurement, and the entire high-resolution spectrum can be obtained in a single image measurement. In this way, 100 spectra per second are acquired. The synchronized x-y stage allows the acquisition of maps of the film thickness within a few minutes.

The working principle is sketched in Figure 25 below. The collimated, linear polarized white light is reflected at an incidence angle of (AOI) of 60° from the reference sample which is rotated by 90° around the main beam axis. Afterwards the light is reflected by the sample at the same AOI. The light passes through an analyzer and is detected by a spectrometer.

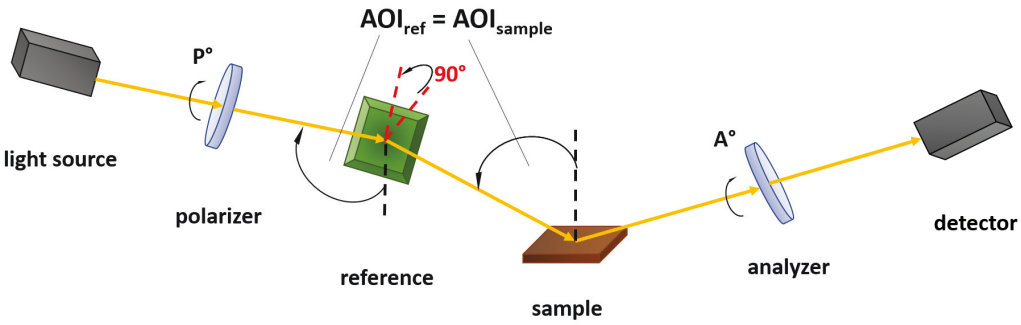

Figure 25: Pathway of light of a Referenced Spectroscopic Ellipsometer. The linear polarized white light is reflected from the reference at an angle of incidence of 60°. The reference is rotated by 90° referring to the beam axis. Thus, the p- and s-polarized components of light interchange in relation to the sample. If the sample and the reference are identical, the outgoing light is linear polarized.

In case of homogeneous, isotropic samples, their behavior can be described by the Jones-Matrix:

$$R_{sam} = \begin{pmatrix} r_{s,sam} & 0 \\ 0 & r_{p,sam} \end{pmatrix}, \qquad 3\text{-}5$$

where r_s and r_p are determined by the Fresnel equations. The light gets reflected at a reference which is rotated by 90° with respect to the beam axis. This can be described by a rotation matrix:

$$R_{ref}^{rot} = \begin{pmatrix} \cos\alpha & \sin\alpha \\ -\sin\alpha & \cos\alpha \end{pmatrix} \begin{pmatrix} r_{s,ref} & 0 \\ 0 & r_{p,ref} \end{pmatrix} \begin{pmatrix} \cos(-\alpha) & \sin(-\alpha) \\ -\sin(-\alpha) & \cos(-\alpha) \end{pmatrix} = \begin{pmatrix} r_{p,ref} & 0 \\ 0 & r_{s,ref} \end{pmatrix} \qquad 3\text{-}6$$

For a reflection coefficient of $r_{i,sam} = r_i + \delta r_i$ with $r_i = r_{i,ref}$ and $i = s, p$, the total reflection matrix becomes:

$$R_{total} = R_{ref}^{rot} \cdot R_{sam} = r_p r_s \left(\begin{pmatrix} 1 & 0 \\ 0 & 1 \end{pmatrix} + \begin{pmatrix} \delta r_p / r_p & 0 \\ 0 & \delta r_s / r_s \end{pmatrix} \right) \qquad 3\text{-}7$$

If the reference is equal to the sample, the second term in equation 3-7 is zero and the identity matrix remains. Thus, the luminous flux can be quenched with the polarizer and analyzer crossed. This shows that the rotated reference compensates for the polarization effects of the sample, it acts as an ideal compensator for all wavelengths, which is a significant advantage over conventional compensator designs.

If the sample differs from the reference, the second term in equation 3-7 is not equal to zero and the emitted light is elliptically polarized. The spectrum of light passing through the analyzer contains information about the difference between the sample and the reference, such as a variation in film thickness.

The software of referenced spectroscopic ellipsometer *nanofilm_rse* was delivered from ACCURION GmbH as well and consist of three taps, which in principle allows all adjustments of the measurement. An overview of the software taps and their possible configurations are sketched in the following list:

Recipe Manager:

- set layer stack
- measurement task
- reference manager
- recipe generation
- auto-optimization of device settings
- simulation of system response

Measurement:

- live display of overview camera and current spectra
- ROI-Editor
- pattern-Editor
- motor control
- automatic sample alignment

Image Viewer

- result window
- 2D/3D-View
- histogram, line profile
- view options
- easy access to spectral data

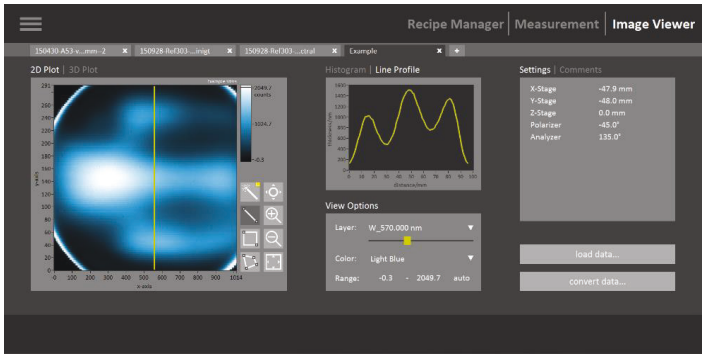

By scanning the sample before deposition and using a three-phase model of silicon, silicon dioxide and air (or two-layer model of silicon and silicon dioxide), the thickness of the initial SiO_2 layer is evaluated (in our case typically ≈ 23 nm). After the deposition of molecules, the sample is again scanned using the same model (i.e. we ignore possible differences in the dielectric properties of the molecules and SiO_2). The thickness of the molecular layer can be calculated by comparing the two measurements, d_1 and d_2, since the optical refractive indexes of silicon dioxide (η_{SiO2} = 1.458) and GLYMO (η_{GLYMO} = 1.429) just differ slightly, leading to a RSE determined thickness:

$$d_{molecule} = d_2 - d_1 \qquad 3\text{-}8$$

Figure 26 shows a typical example of a 10 x 10 mm² SSO sample covered with GLYMO.

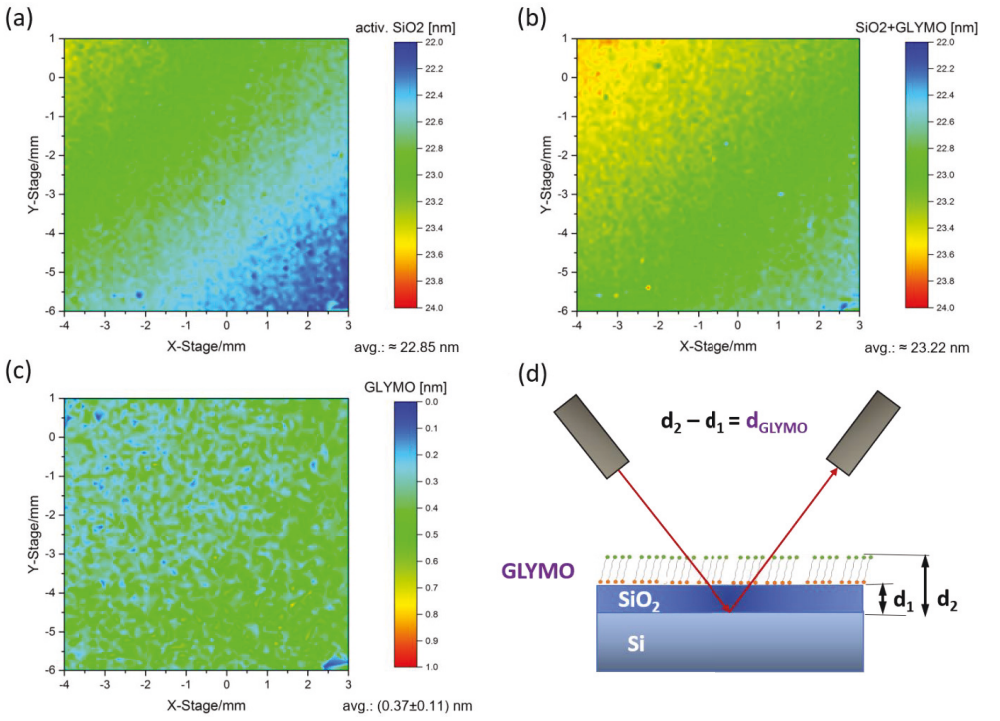

Figure 26: (a) Measurement of an activated SSO substrate without molecules before the deposition. (b) Measurement of the SSO substrate with molecules after the deposition. (c) The resulting contour plot of the thickness of the GLYMO monolayer determined via ellipsometry on SSO substrate according to eq. 3-8. Average values and standard deviation are obtained from the resulting data points. (d) Schematic measurement principle of the SSO with molecules and corresponding sizes of the substrate, SiO_2 layer and GLYMO molecules.

According to literature the thickness of a GLYMO monolayer is approx. 0.3 nm [8] which agrees with our measurement of (0.37±0.11) nm as shown in Figure 26.

The RSE device was only installed at the beginning of this year in the Helmholtz Nano Facility (HNF) of the Forschungszentrum Jülich and is a quiet new tool to analyze surfaces there. In order to complete the description of the new device, all important specifications are listed below:

SPECIFICATION	
Instrument Type	Referenced Spectroscopic Ellipsometer
Angle of Incidence	Fixed 60° or 70°
Spectral Range	450-900 nm, 1.2 nm resolution
Data Rate	100 full spectra per second, continuous
Spot Size	50x100 µm microspot at AOI=60°
Film-Thickness Resolution	typ. 0.1 nm
Film-Thickness Reproducibility	typ. < 0.4 % standard deviation
Light Source	110 mW supercontinuum laser, class 3b, $M^2 = 1.1$
Detector	2048-channel Czerny-Turner spectrometer, 16 bit, 100 Hz
Polarizing Optics	Two high quality Glan-Thompson prisms, motorized, 0.001° resolution
Alignment	Two-axis horizontal sample alignment
X-Y-Z-Positioning	Motorized X-Y-Stage with 100 mm range, max. 14 mm/s, motorized Z-positioning in instrument head with 40 mm range
Data Processing	LUT-based data processing for live fitting of film-thicknesses
Software	Including control software for easy access to motorized components, spectrometer and all measurement parameters; including modeling software
PC	Ready to use PC running on Windows 7, pre-installed control and modelling software
Power Supply	100-240 V, 50/60 Hz
Environmental Conditions	Operating temperature range: 15-30 °C Humidity: 20-80 %RH

3.4.2 Surface Potential Measurements

In this thesis, the streaming current method was used to determine the so-called ζ potential of our films, which is correlated with the surface charge.

In general, solid surfaces in contact with a polar medium show certain surface charges caused by ionization, ionic adsorption and ionic dissolution at the interface. These charges influence the neighboring ions in the polar medium. The rearrangement of the charges at the solid surface and the balancing charges in the medium are usually described by the electrical double layer model (EDL model).

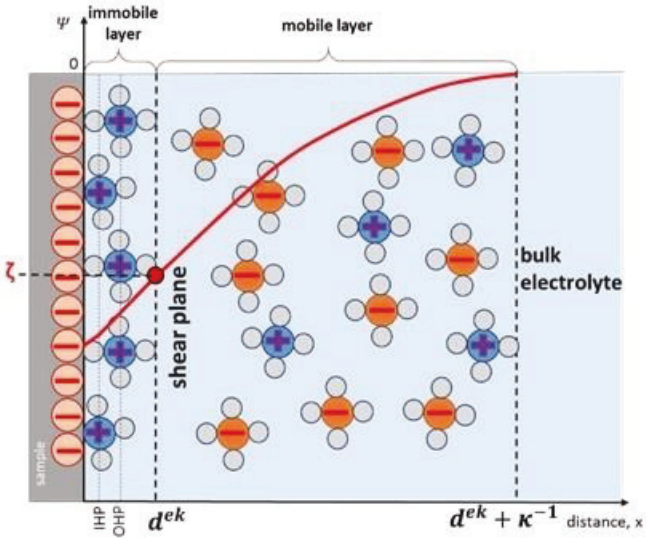

Figure 27: The electric double layer (EDL) as schematic visualization according to the Gouy-Chapman-Stern-Grahame-Theory.

The EDL consists of a mobile layer and an immobile layer (see Figure 27). The redistribution of ions in the EDL generates the electrical potential (red line in Figure 27) near the charged surface. The boundary between the immobile layer and the mobile layer is called the shear plane. The electrical potential at the solid surface is difficult to measure directly. However, the electrical potential at the shear plane, known as the ζ potential, can be measured and is therefore a very important property of the solid-liquid interface. It is given by:

$$\zeta = \Psi(d^{ek}) \qquad 3\text{-}9$$

In the immobile layer, the potential changes linearly with distance x, while in the moving layer it varies exponentially with x:

$$\Psi(x) = \Psi(d^{ek}) \cdot e^{-\kappa(x-d^{ek})} \qquad 3\text{-}10$$

In this thesis, the streaming current method is chosen to determine the ζ potential. In principle, our device consists of a microchannel consisting of two parallel planar sample surfaces with channel height h, width w, cross-section $A = h \cdot w$ and length L (see Figure 28).

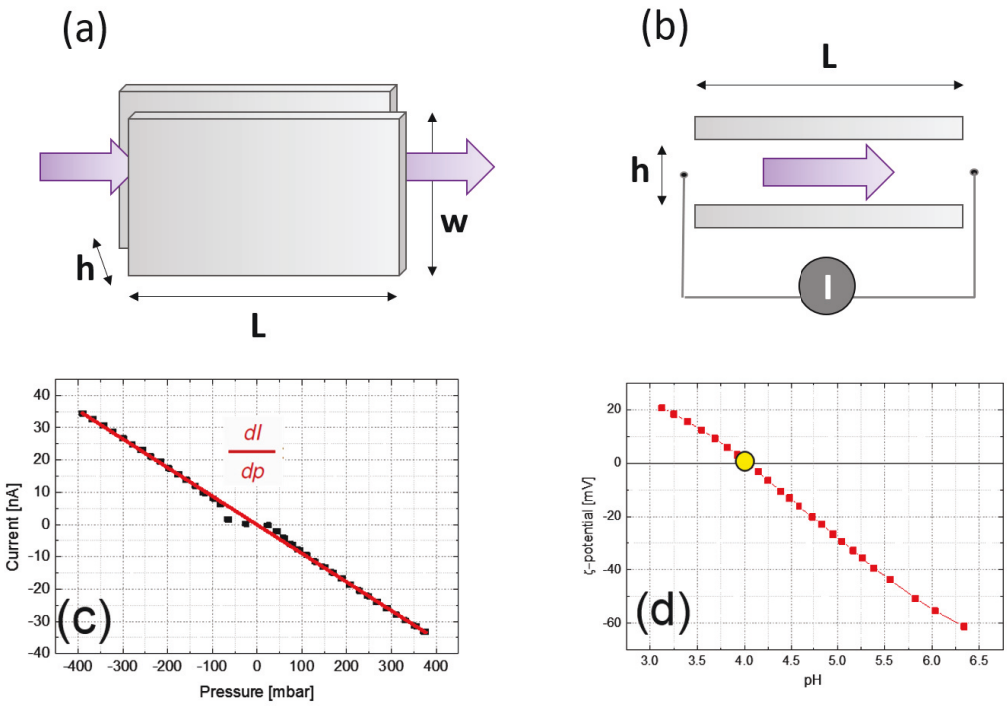

Figure 28: (a) Parallel plate microchannel for the flow rate measurement, (b) sketch of the measuring principle, where arrows indicate the flow direction (c) an example of a flow measurement, (d) the resulting evaluations of the ζ potential based on eq. 3-12.

When an electrolyte is forced to flow through the microchannel under an applied hydrostatic pressure Δp between the two ends of the microchannel, the counter ions in the moving layer of the EDL are carried downstream, resulting in an electric current in the pressure-driven flow direction. This current is called streaming current:

$$I_{str} = -\frac{\varepsilon\varepsilon_0\zeta}{\eta}\cdot\frac{A}{L}\cdot\Delta p \qquad 3\text{-}11$$

where η and ε represent the dynamic viscosity and relative dielectric constant, respectively, of the liquid. The current I_{str} can be recorded with measuring electrodes at both ends of the capillary, which are connected via a small external resistance under short-circuit conditions.

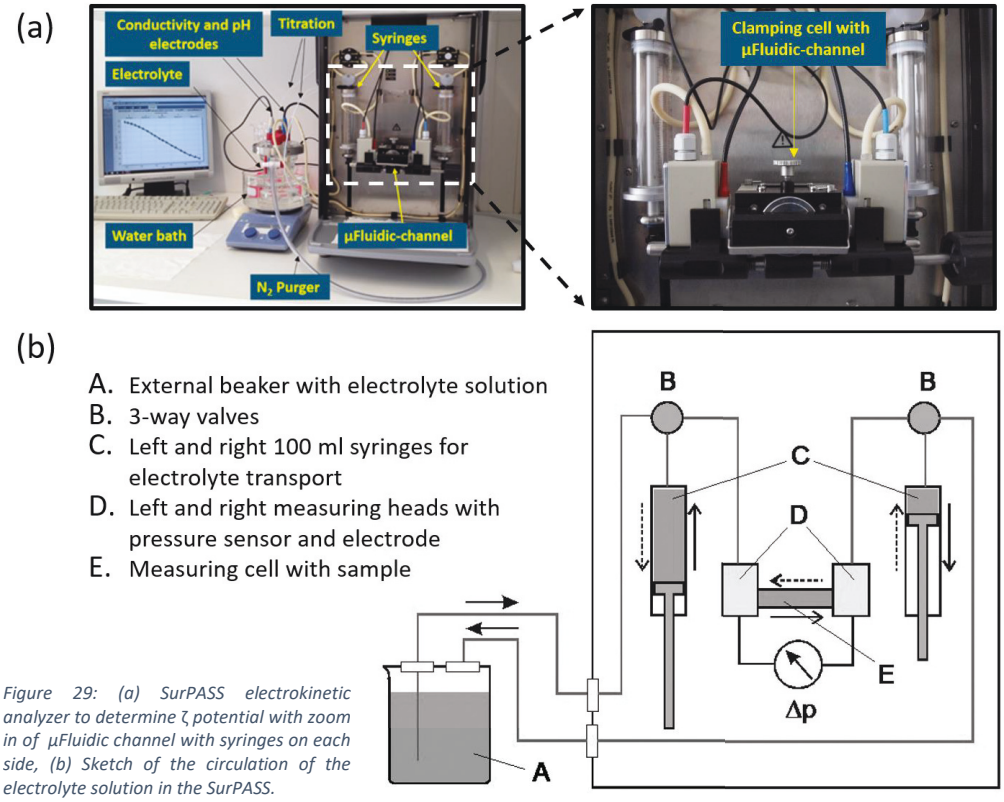

Figure 29: (a) SurPASS electrokinetic analyzer to determine ζ potential with zoom in of µFluidic channel with syringes on each side, (b) Sketch of the circulation of the electrolyte solution in the SurPASS.

To analyze the surface potential of the molecular layer, we use a modified electrokinetic analyzer (SurPASS, AntonPaar Germany GmbH, see Figure 29). A pair of identical flat substrates (10 mm × 10 mm) is placed in a clamping cell with the surfaces to be analyzed facing each other and forming a microfluidic channel. In order to obtain a large signal, a small distance ($h \approx 70$ µm) is chosen between the two plane-parallel surfaces, which still permits laminar flow of the electrolyte. The ζ potential is determined by measuring the pressure dependence of the current (Figure 28 (c)) using the Smoluchowski equation, to obtain the following equation:

$$\zeta = \frac{dI}{dP} \cdot \frac{\eta L}{\varepsilon \varepsilon_0 A}, \qquad 3\text{-}12$$

where P is the pressure required to generate the laminar flow and I is the resulting current measured between two electrodes located on each side of the measuring cell [19]. The resulting ζ potential represents the potential at the shear plane between the immobile (Helmholtz layer) and the mobile layer and is a measure of the surface potential [20].

3.4.3 Fluorescence Microscopy

In this thesis, fluorescence microscopy was used for the visual detection and analysis of

i. PLL in combination with fluorescent markers FITC
ii. substrates covered with monolayers of GLYMO and
iii. living and dead neuronal cells modified with fluorescent dyes.

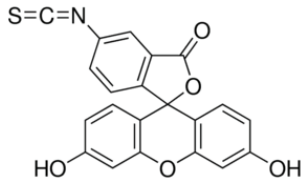

Figure 30: Fluorescein isothiocyanate (FITC) with chemical formula: $C_{21}H_{11}NO_5S$

The absorption and subsequent emission of light by organic and inorganic specimens is typically the result of fluorescence or phosphorescence. Fluorescence describes the almost simultaneous absorption and emission (usually less than one microsecond delay). The emission lasts longer with phosphorescence after the excitation light is extinguished. The basic function of a fluorescence microscope is to irradiate the sample with a desired and specific wavelength and then separate and collect the much weaker emitted fluorescence. In a properly configured microscope, only the light emitted by the sample should be detected to superimpose the resulting high contrast fluorescent structures against a very dark background. The detection limits are generally determined by the darkness of the background, and the excitation light is typically several hundred thousand to one million times brighter than the emitted fluorescence.

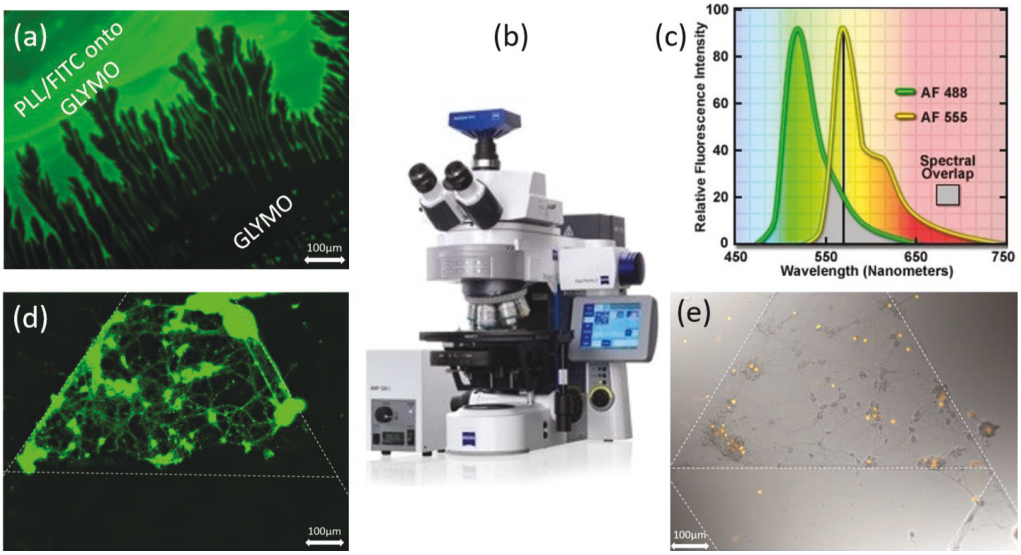

Figure 31: (a) Example of an fluorescence microscope image of a SSO substrate covered with GLYMO and partially marked with PLL+FITC drop, shown is an image of the drop border (b) image of fluorescence microscope "ZEISS ApoTome", (c) Fluorophore emission profiles for 488nm (live cells) and 555nm (dead cells), (d) example of an image of stained live neurons and (e) image of stained dead neurons.

The intensity peak of the fluorophore emission (or absorption) is usually lower in wavelength and intensity than that of the excitation peak, and the emission spectrum is often a mirror image (or almost) of the excitation curve, but shifted to longer wavelengths (see Figure 31 (c)). The effective separation and detection of excitation and emission wavelengths in fluorescence microscopy is achieved by the correct selection of filters to block or pass certain wavelength bands in the ultraviolet, visible and near infrared spectral range.

In this work we used a Zeiss-Apotome-Microscope (Figure 31 (b)) and the Zen software. The fluorescence microscopy technique was used in two different experiments which are described in detail below.

PLL/FITC marked Intensity Analysis: PLL is a synthetic polymer, a homopeptide commonly used to coat tissue cultures as a binding factor to improve cell adhesion. Fluorescein isothiocyanate (FITC) is an original fluorescein molecule functionalized with an isothiocyanate-reactive group and replacing a hydrogen atom on the lower ring of the structure. This derivative is reactive to nucleophiles including amine and sulfhydryl groups on proteins. To visualize the PLL coating by fluorescence microscopy, we used a PLL-FITC solution. This PLL-FITC solution (P3069, Sigma-Aldrich) was mixed with milli-q water to a final concentration of 10 µg/mL. The samples were coated with one drop (45 µl) of the solution and kept at room temperature for 1 hour avoiding any exposure of light. The remaining drop was then removed from the surface by rinsing with milli-q water and thus, the remaining protein which was not bound to the SAM was washed away. The sample was then purged in a N_2 stream for drying. After the entire process was completed, the adhesion of the PLL to the supports (e.g. coated with a molecular layer of GLYMO) can be visualized by fluorescence microscopy. Usually three images from different areas of each sample are taken with an exposure time of 1500 ms and an illuminance of 3.04 V from a Zeiss HXP light source.

Later, in order to obtain representative values for the intensity of the fluorescence, averaged intensities for areas of 45 µm × 45 µm of each picture were taken and evaluated with the Zen software.

Live-Dead Imaging: In the case of neurons (Figure 31 (d) & (e)), live-dead staining was performed 1 µg/mL Calcein-AM and 2 µM Ethidium Homodimer (both Life Technologies) in supplemented cell growth medium to stain live and dead cells in green and red, respectively. Cells and dyes were incubated for 15 minutes in an incubator at 37 °C. Samples were observed and pictures were taken through the Zeiss-Apotome-Microscope using Zen software.

After staining, images of the cells were taken, and cell statistics were performed (via Zen software).

3.5 Patterned Neuronal Culture

Functionalization of solid surfaces with proteins by patterning provides powerful strategies to generate active bio interfaces. Using lithographic procedures and lift-off techniques, cell-attractive molecules can be applied to cell-repulsive or toxic surfaces. This enables to generate various micropatterns that support cell adhesion, neurite outgrowth, and the formation of a geometrically defined network along the permissive regions. In such networks of reduced complexity, signal transduction and signal processing can be studied under various experimental conditions. The following chapter presents the surface structuring approach chosen in the thesis and gives short details on neuron cultivation as well as an overview of the evaluation methods of neuron growth.

3.5.1 Patterning of Molecular Layers with Lithography and Lift-off Technique

The pattering design chosen in this thesis is given in Figure 32.

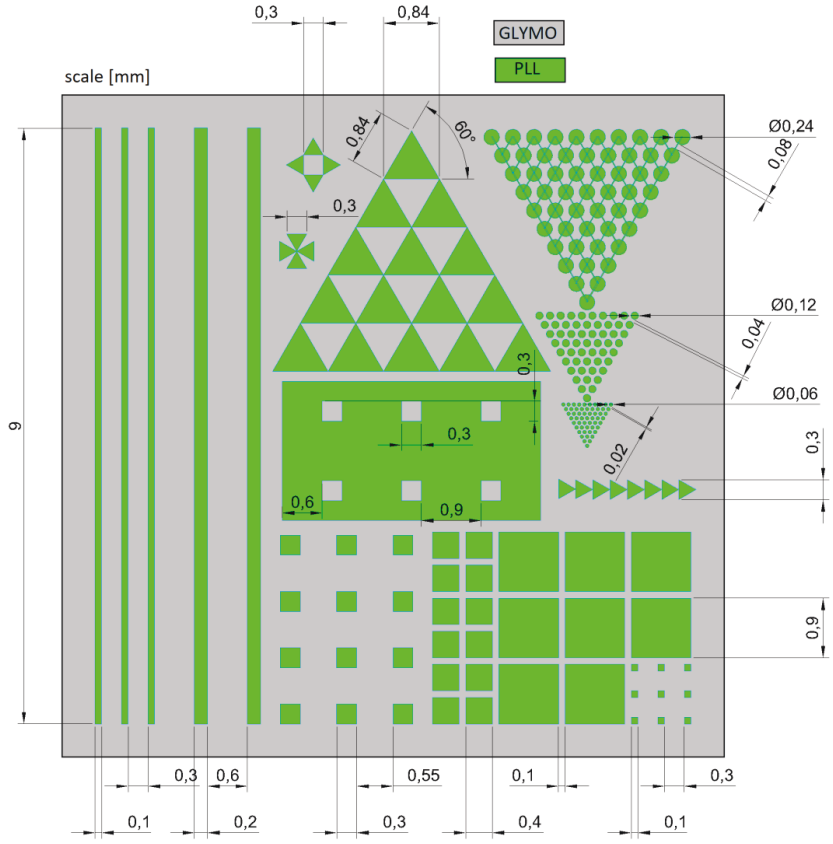

Figure 32: Design of the 10 mm x 10 mm SSO chip patterned with GLYMO and PLL. The green areas represent the patterned PLL on a GLYMO SAM (grey).

The green areas in Figure 32 represent PLL areas on a GLYMO SAM (white area), which will be deposited via gas phase MLD according to section 3.2.2. Several structures are combined. Squares and bars are examples for guided cell growth in a certain direction. Congruent triangles are suitable structures for unidirectional single cell electrophysiology studies and the smallest structure, the 20 µm diameter circles, are eligible structures for single neuron cell study.

The interface patterning via a combination of a self-assembled GLYMO layer and a patterned layer of PLL for guided cell growth was done according to the electron lithography and lift-off process of the temperature sensor (section 3.3.2). SiO_2 (≈ 23 nm) terminated Si is used as substrate. In all cases, the molecules are deposited in GLOBUS (section 3.2.2). In Figure 33, the structuring process of the molecular GLYMO layer in combination with PLL for guided cell growth is sketched and consists of the following steps:

(1) Cleaning and activation of the sample with ozone
(2) GLYMO deposition
(3) Spin-coating of PMMA
(4) E-beam lithography
(5) Development
(6) PLL deposition
(7) Lift-off
(8) Further experiments (e.g. cell culture)

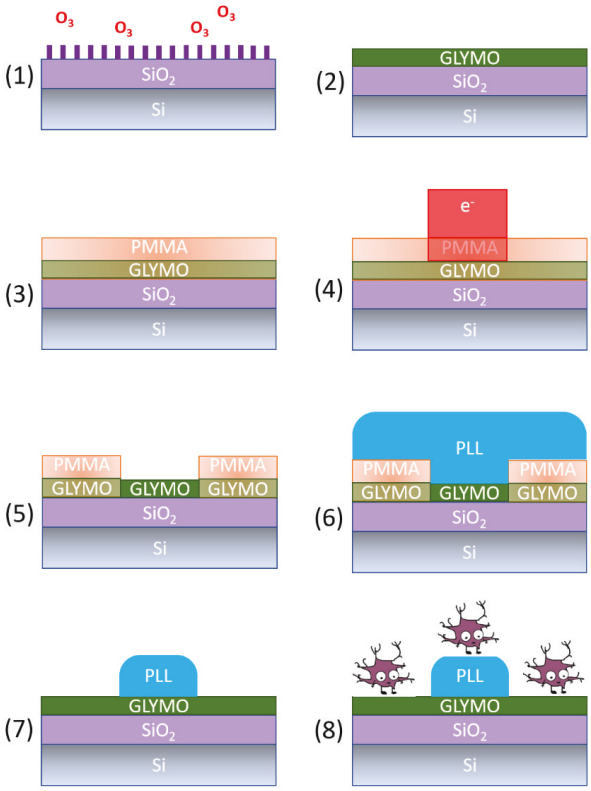

Figure 33: A schematic sketch of the different pattering steps for guided neuron growth.

3.5.2 Neuronal Cell Culture

Cortical neurons were obtained from E18 Wistar rat embryos. Briefly, the cortex was cut from embryonic brain tissue and digested with trypsin-EDTA at 37°C, 5% CO_2 and 100% humidity for 15 minutes. To remove trypsin, the cortex was washed five times with neurobasal medium (Life Technologies GmbH, Germany) supplemented with 1% B27 (Life Technologies, Germany), 0.5 mM L-glutamine and 50 µg/ml gentamicin. The cortex was then carefully dissociated with a 1 mL pipette allowing the cell clumps to settle for 2 minutes at room temperature. The supernatant

was diluted in supplemented neurobasal medium and the cells plated with ≈ 25k cells/cm². The medium was completely changed 4 hours after plating. In the following days the medium was half changed twice a week. The animal work was carried out with permission of the Landesumweltamtes für Natur-, Umwelt- und Verbraucherschutz Nordrhein-Westfalen, Recklinghausen, Germany.

3.5.3 Neuron Density Analysis

To calculate the neuron density, the mean pixel size per neuron (516 pixels) is firstly determined from the origin image (Figure 34 (a)) by taking 10 different single neurons. Then a threshold value for the emission light of the living cells is set. This filter is applied to identify all pixels below this threshold and display them in blue (see Figure 34 (b)). The remaining green pixels were summarized and divided by the average pixel size of a neuron. From the number of neurons per image area the average neuron density can be calculated. An example of two 900 µm x 900 µm ($1.947 \cdot 10^6$ pixels) areas are given below. Pixels are counted via Zen software.

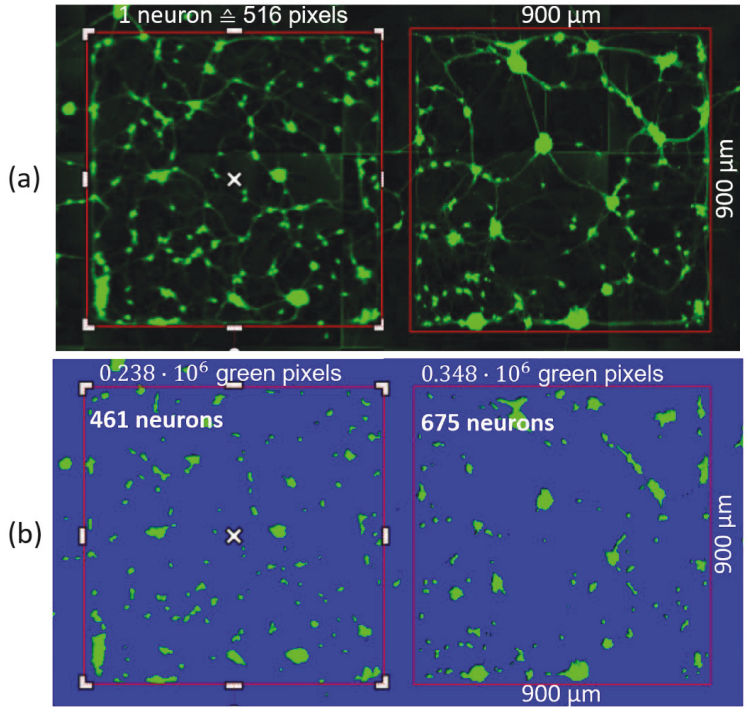

Figure 34: (a) Image of a GLYMO and PLL pattered substrate (patterned according to chapter 3.5) coated with cortical rat neurons. Live cells are marked with calcein-AM (green). Shown are two the squares structures with a side length of 900 µm, DIV 6. (b) Identical structure as in image (a) but background subtracted so that just the fluorescence marked neuron pixels are visible.

4 Gas-Phase Deposition of GLYMO at Elevated Temperatures

One of the major aims of this work was to improve the existing molecular layer deposition (MLD) process by integrating a heater to the MLD setup. The enhancement and optimization of the deposition temperature was expected to improve the deposition process and thus might lead to:

- a faster formation of SAMs (i.e. reduction of the post deposition time) and
- a better quality of the resulting monolayer.

Therefore, an optical heater was installed which allowed to vary the temperature of the substrate from room temperature to more than 120°C (see section 3.3.4). In order to monitor the impact of the process temperature on the formation and quality of the SAM, the post-deposition treatment was reduced from 24h to 1h. The resulting properties of the molecular layer are analyzed via RSE, fluorescence microscopy and surface potential measurements (long term and titration experiments). In all cases 10 mm x 10 mm SiO_2 terminated Si substrate were used with a SiO_2 thickness of ≈23 nm, the silane for the deposition was GLYMO and the MLD preparation parameters are given in section 3.2.2.

4.1 Referenced Spectroscopic Ellipsometer (RSE)

The optical thickness of the GLYMO layer was measured via ellipsometry after the deposition at given temperature and post-deposition time of 1h. For a detailed description of the deposition see chapter 3.2. Figure 35 shows two examples of RSE analyzes of GLYMO films deposited at room temperature and 106°C. On first sight, both samples show a homogeneous coating with GLYMO with an average thickness which nicely agrees with the literature value of (0.3±0.05) nm [8].

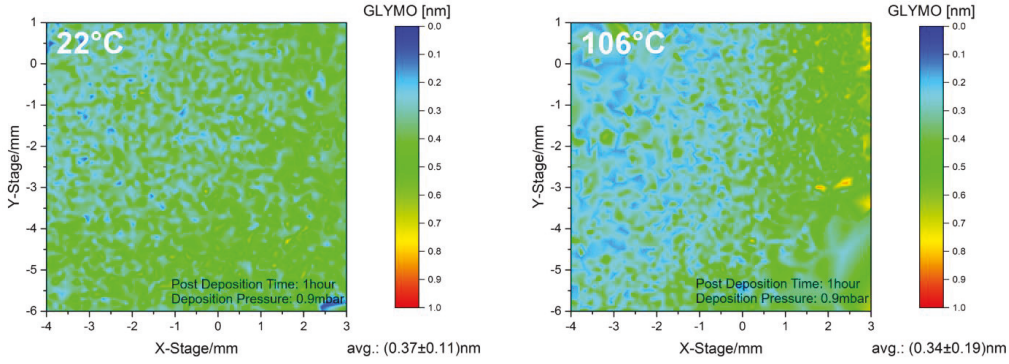

Figure 35: RSE images of GLYMO layers obtained via gas phase deposition with 1 h deposition and 1 h post deposition time at 0.9 mbar for temperatures of 22°C and 106°C.

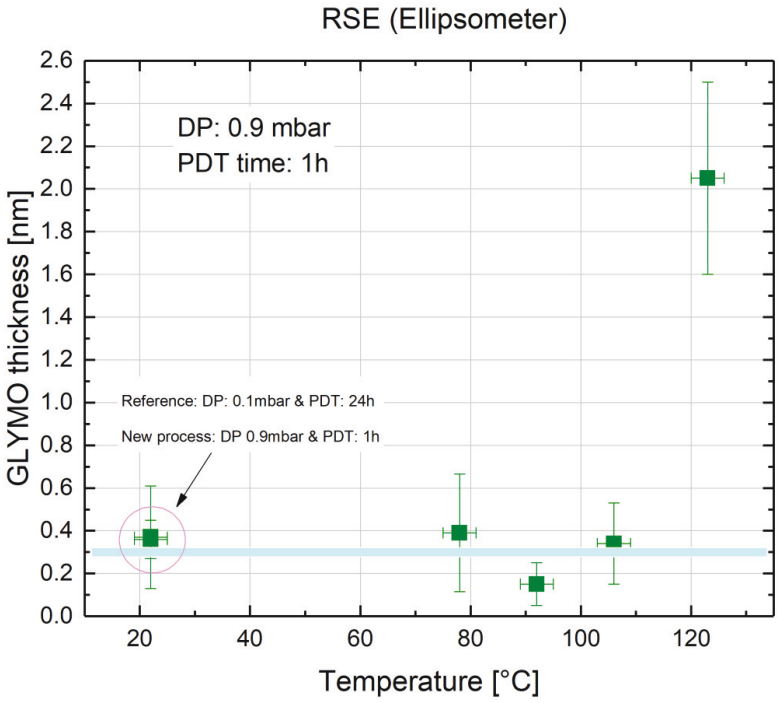

Figure 36: Overview of the layer thickness of GLYMO films deposited at different temperatures obtained via RSE. Except for one reference deposition at room temperature, the deposition time was always 1 h.

Figure 36 shows an overview of the optically determined thicknesses of the GLYMO films. Up to ≈110°C, the data agree with the literature value. However, at a temperature of 123 °C the layer thickness increased drastically (see also Figure 37). It is known that Si-C bonds in silanes are broken at temperature above 400 K (≈127 °C) (by splitting off alkyl groups) [21]. Therefore, it can be expected that the molecular structure of GLYMO is broken during the heating process and a layer of carbon (or even silicon) is deposited/formed on the SiO_2 surface. This could lead to the observed increase of the deposited layer of about 2 nm. The exact value of the thickness of this layer might differ from the given value, since the analysis with the two layer model of Si and (SiO_2 + GLYMO) is no longer valid, because the optical refractive index of carbon ($\eta_C = 2.699$) and silicon dioxide ($\eta_{SiO2} = 1.458$) with GLYMO ($\eta_{GLYMO} = 1.429$) differs drastically. This is also reflected in the large error of the data point for the deposition at 123°C. The evaluated thickness of approx. 2 nm is no longer meaningful. Further measurements to determine the element composition would be necessary in order to develop a better RSE model. However, since this does not provide any further information with regard to the optimization of the GLYMO deposition, no further analysis of the element composition was carried out.

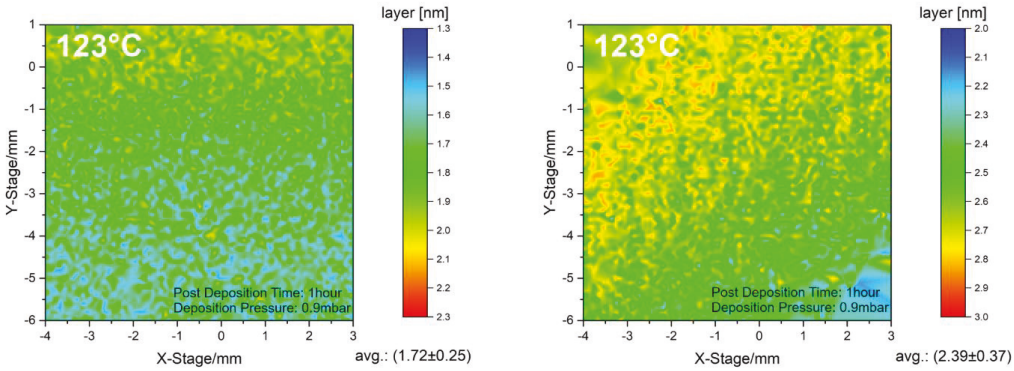

Figure 37: Examples of RSE contour plots of the thickness for two GLYMO films obtained via gas phase deposition with 1 h deposition and 1 h post deposition time at 0.9 mbar and 123°C.

In conclusion of these RSE analyses we can state, that thin GLYMO layers with a RSE thickness of ≈0.3 nm are formed up to temperatures of ≈110 °C within 1 h of deposition and 1 h of post-deposition treatment. Above ≈120 °C significantly thicker films (RSE thickness of ≈2 nm) are formed which do not consist of GLYMO. They most likely consist of the remains of the molecule, i.e. carbon or silicon. However, the RSE results do not provide any information on the quality of the layer or even the SAM formation. Moreover, the optical thickness of the GLYMO layers deposited at room temperature with 1 h and 24 h post deposition time show comparable thicknesses (see Figure 38), although we know, that a long time (typically 24h) is necessary to form a SAM of GLYMO [22]. Therefore, it is necessary to perform additional characterization to analyze the quality of the samples.

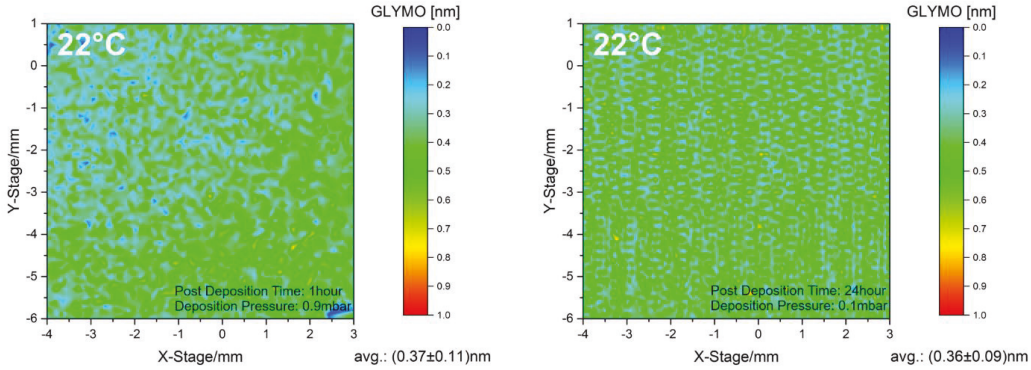

Figure 38: Comparison of RSE data obtained for the GLYMO layer thickness deposited at room temperature with 24h (DP: 0.1mbar) and 1h (DP: 0.9mbar) post deposition time.

In the following chapters fluorescence microscopy and surface potential analysis provide more insight on the film quality.

4.2 Fluorescence Microscopy

In the previous chapter the layer thickness of GLYMO deposited at various temperatures on SiO_2 was discussed. The thickness based on the RSE measurements cannot be used to analyze the layer quality or molecular density of the GLYMO layer. Fluorescence microscopy represents a tool to monitor the change of the molecular GLYMO layer. As described in section 3.4.3, three areas of 45 µm x 45 µm from each sample (coated with GLYMO and PLL/FITC) were taken to analyze the intensity of the fluorescence signal (see Figure 39).

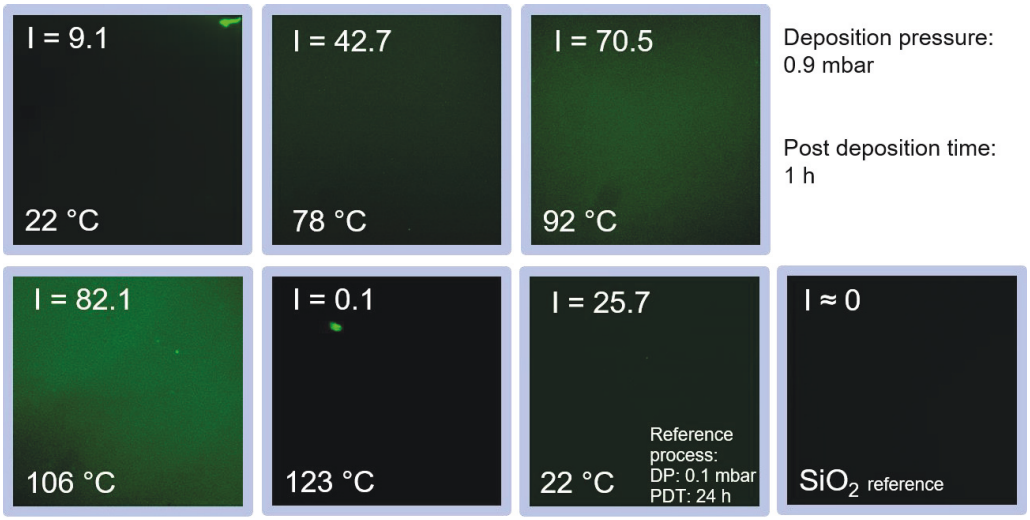

Figure 39: Fluorescence microscope images of areas of 0.5 mm x 0.5 mm samples (SiO_2 terminated Si) after MLD of GLYMO and coating with PLL/FITC. All pictures are taken with exposure time of 1.5 s and are evaluated with ImageJ software. The numbers provide the deposition temperatures, the average intensity I is given at the top left position.

PLL with FITC was deposited onto the molecular layers by coating the film with a drop (50 µl) of a PLL/FITC solution (1 mg/ml) and keeping the sample protected from exposure to light at room temperature for 1 hour. After deposition, the PLL/FITC that was not bound to the molecular layer, was removed by rinsing with milli-q water for several seconds and subsequently dried with a flow of nitrogen. The PLL binds to the epoxy functional group of GLYMO. As a consequence, the amount of PLL/FITC increases with an increasing amount of bound GLYMO, which then is visible in the intensity of the fluorescence signal.

There is a clear correlation of the fluorescence intensity and the deposition temperature (see Figure 40). Apparently, temperature has an effect of the molecular density of covalently bounded GLYMO. In contrast to the RSE measurements, where the optical thickness of physiosorbed and the covalently bounded GLYMO molecules are equally measured, it is expected that PLL binds to the epoxy functional group of GLYMO and that after rinsing with milli-q water just the covalently bounded GLYMO molecules (plus PLL) are left on the SiO_2 surface. The SiO_2 reference sample

doesn´t show any fluorescence, as expected, because the PLL with FITC marker doesn't bind to the SiO_2 surface (I ≈ 0).

Figure 40 shows the fluorescence intensity of the PLL/FITC marked GLYMO layers as a function of the temperature. Generally, the increase of deposition temperature leads to an increase of intensity up to a temperature of ≈ 110 °C. It starts with I = 9.1 at room temperature and finally reaches I = 82.1 at 106°C. However, at higher temperatures (123 °C) the signal drops dramatically to I = 0.1. No PLL with FITC seems to be present on the sample for this deposition temperature. As discussed in chapter 4.1, Si-C bonds in silanes are most likely broken at elevated temperature above 400 K (≈ 127 °C). Therefore, it can be expected that the deposited GLYMO molecules are broken during the deposition and a layer of carbon (or even silicon) was formed on the SiO_2 surface. PLL with FITC cannot bind on this surface and after rinsing with milli-q water the fluorescence marker was removed and no fluorescence is measured.

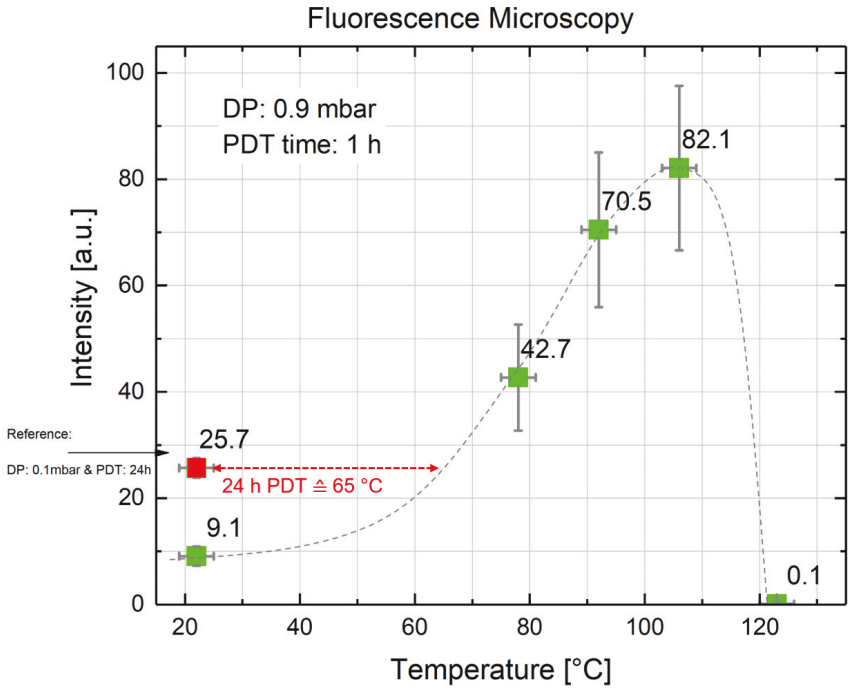

Figure 40: Fluorescence intensity of the PLL/FITC marked GLYMO as a function of the deposition temperature. The dashed guide for the eye line connects the samples with a 1h PDT time.

In chapter 4.1 it was shown that the optical thickness of the GLYMO layers deposited at room temperature with 1h (DP: 0.9 mbar) and 24 h (DP: 0.1 mbar) post deposition time are comparable. The fluorescence indicates as well that in both cases GLYMO is deposited on the SiO_2 surface.

However, the intensity and therefore the density of covalently bounded GLYMO is much higher for the sample with the longer PDT. It is I = 25.7 for a 24 PDT (similar to 1 h PDT for a process temperature of ≈ 65°C) in contrast to I = 9.1 for a 1 h PDT. This points out that:

- Firstly, the post deposition time plays an important role in the SAM formation process. If more time is given to the system, the layer quality will increase in terms of covalently bounds and removal of physiosorbed GLYMO and a SAM will be formed.
- Secondly, instead of enhancing the time of the PDT, the temperature can be enhanced. An increase of the deposition temperature from room temperature to 106°C leads to an increase of the fluorescence intensity by a factor of 9 (I = 9.1 to I = 82.1), whereas we only obtain an increase of the signal by a factor of ≈ 3 (I = 9.1 to I = 25.7) if we enhance the PDT time from 1 h to 24 h. Thus, the enhancement of the deposition temperature is definitely more efficient. Moreover, the reduction of process time is most important for any type of application.

Finally, we have to examine the stability of resulting GLYMO layers, which is another indication for the presence of SAMs. This is described in the next chapter.

4.3 Surface Potential Measurements

The electrokinetic potential (ζ potential) is an important interfacial property which affects a large number of natural phenomena like electro kinetics, electrocatalysis, corrosion, adsorption, crystal growth, colloid stability or flow characteristics. Therefore, during this work, the ζ potential was used:

i. To prove the deposition of GLYMO
ii. To analyze the stability of the layer (another indication for SAM formation), and
iii. To characterize the molecular layer of GLYMO.

It turned out to be very ambitious to correlate surface potential and quality of the molecular layer of GLYMO, since the functional group of GLYMO (ethylene oxide) is typically neutral in contact with electrolyte and therefore might hardly affect the surface potential. Moreover, the activation of the SiO_2 strongly affects the surface potential. Additionally, pre-adjustments of the measuring setup like gap size adjustment and flow check (see section 3.4.2) are already invasive procedures which could add contaminations and remove physiosorbed GLYMO molecules from the surface. Nevertheless, the work was done and will be presented in the following. Let´s start with the simplest case, the ozone activated SiO_2 surface.

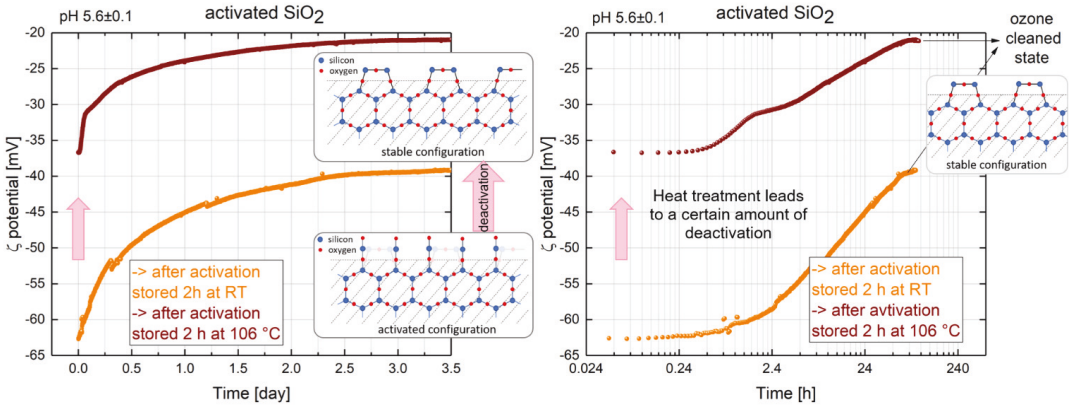

Figure 41: ζ potential of ozone activated SiO_2 after 2h storage at RT (0.9 mbar, orange) and 106°C (0.9 mbar, brown) in a linear (left) and in a semilogarithmic plot (right).

Figure 41 illustrates the impact of the temperature on the "deactivation" of activated SiO_2. As such it simulates the impact of temperature on the substrate without the molecular layer. The figure shows a comparison of the development of the ζ potential of ozone activated (3 min) SiO_2 surfaces after storing it for 2 h in vacuum (0.9 mbar) at room temperature or at elevated temperature of 106 °C. In both cases, we see the typical relaxation of the activation of the SiO_2 surface which takes days [22]. However, for room temperature it starts at a lower potential (≈ -63 mV) whereas a starting potential of ≈ -39 mV is observed after heating the sample for 2 h to

106 °C. The heated sample seems to have completely lost the activation after approximately 3 days when it reaches the final value of ≈ -22 mV of cleaned SiO_2, whereas the sample stored at room temperature seems to still be partially activated even after 3 days (ζ potential of ≈ -38 mV).

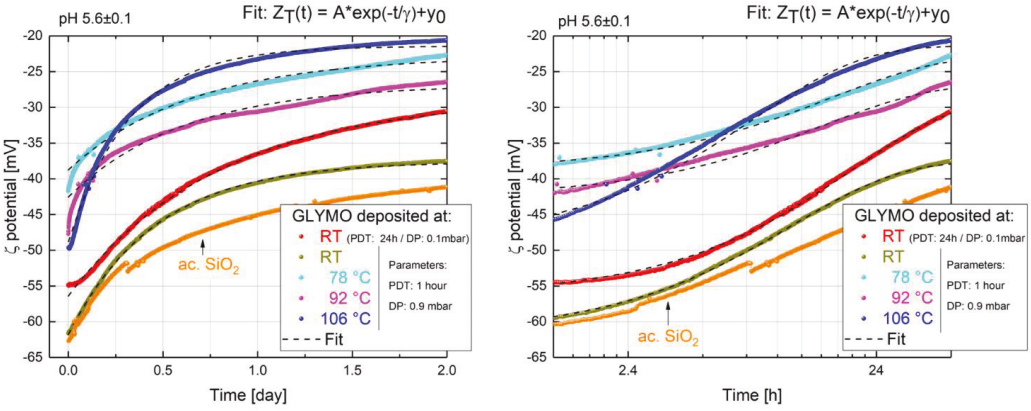

Figure 42: ζ potential of SiO_2 with GLYMO layer measured directly after the deposition process in linear (left) and semilogarithmic (right) form. Additionally, the activated SiO_2 (room temperature) and fits (dashed lines) of the data are given.

Figure 42 shows a comparison of the time dependent measurement of the ζ potential for GLYMO films deposited at different temperatures. For comparison, data for activated SiO_2 (room temperature) is added. All curves show a similar increase of the ζ potential in time which is typical for the relaxation of the surface activation. However, the general voltage level of the curves is different for each curve. The lowest ζ potential is observed for the activated SiO_2 without GLYMO, followed by the room temperature deposited films starting with 1 h PDT time followed by 24 h PDT time. The highest ζ potentials are observed for the films deposited at elevated temperatures.

The time dependence of the ζ potential can be approximated by a relaxation law according to:

$$\zeta_T(t) = A \cdot exp\left(^{-t}/_{\gamma}\right) + y_0 \qquad 4\text{-}1$$

The resulting fits are shown in Figure 42. Figure 43 displays the temperature dependence of $\zeta_T(t)$ at the start of the measurement, on day 1 and day 2. In addition, the temperature dependence of the decay constant γ is shown.

All $\zeta_T(t)$ values show a similar increase of the ζ potential in time which is typical for the relaxation of the surface activation. As previously discussed, samples stored at room temperature seem to still be partially activated after 2 (to 3) days, whereas the heated samples seem to have mainly lost the activation after approximately 2 (to 3) days when they reach the final value of the ozone cleaned state (between ≈ -30 mV to-22mV). The room temperature deposited film with 1 h PDT has approximately the same $\zeta_T(t)$ value after 2 days (≈ -37.9 mV) as the room temperature

deposited film with 24 h PDT after 1 day (≈ -36.5 mV), which coincides with the 24 h longer time of deactivation for this.

The decay constant γ for the films deposited at elevated temperatures shows a linear tendency. The higher the process temperature the faster is the SAM formation. Surprisingly, the decay constant (γ = 20.2 h) of the sample with 24 PDT at room temperature would fit ideally to a sample with 1 h PDT and process temperature of ≈ 65°C (Figure 43 (d)). This confirms the observation of the fluorescence microscopy in the previous chapter, where the fluorescence intensity for the sample with 24 PDT and room temperature was similar to that for 1 h PDT and process temperature of ≈ 65°C. Moreover, the decay constant γ = 20.2 h for 24 h PDT and room temperature agree with literature values [22].

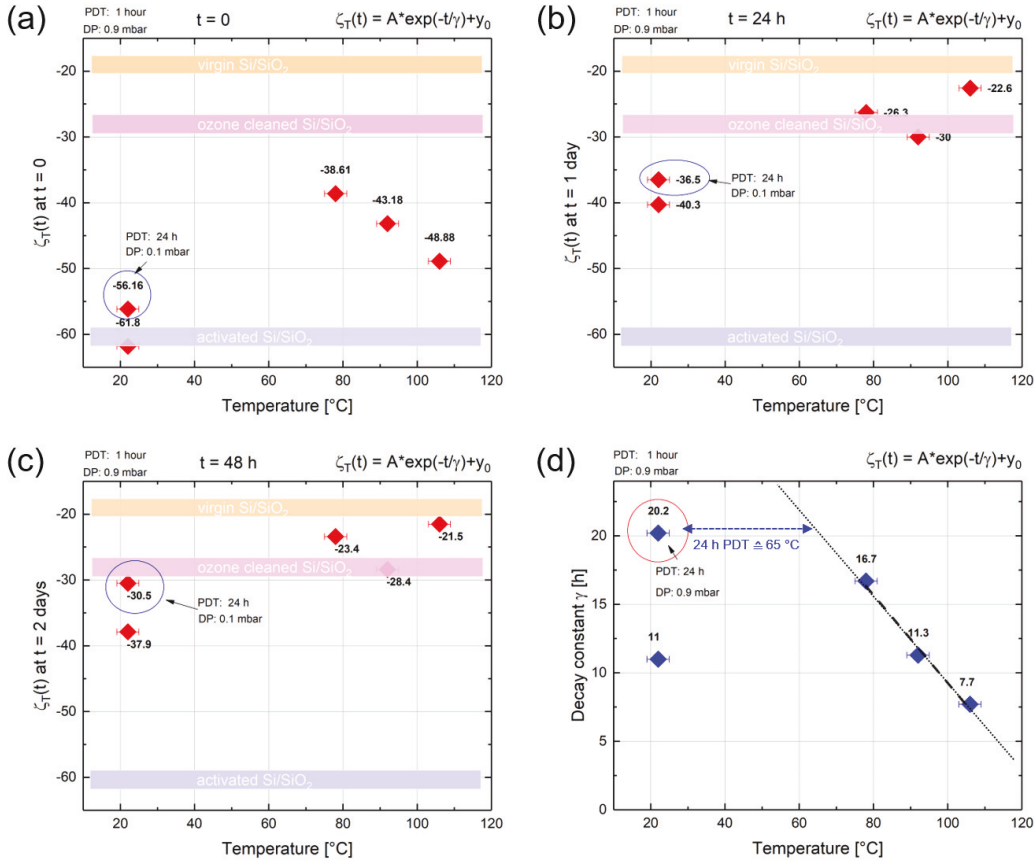

Figure 43: $\zeta_T(t)$ values for SiO_2 with GLYMO layer as function of different process temperatures (a) directly after the deposition process, (b) after 1 day and (c) after 2 days. The decay constant γ of the fit function $\zeta_T(t)$ as a function of the process temperature is given in (d).

Finally, titration experiments are performed on the GLYMO layers after they had been exposed to the electrolyte (1 mM KCl) for at least 6 days. The pH dependence of the ζ potential is shown in Figure 44. The main message of this plot is, that in contrast to all other films, the GLYMO film deposited at room temperature with 1 h PDT shows an extremely low ζ potential which is comparable to the ozone activated SiO_2 without GLYMO. Already an increase of the PDT time to 24 h leads to a significant increase of the ζ potential. We therefore conclude that it is necessary either to provide a long PDT or an elevated deposition temperature to achieve a chemical binding of the GLYMO and from a GLYMO SAM. These measurements confirm the observation of the fluorescence microscopy given in the previous chapter and demonstrate that the GLYMO films are very stable.

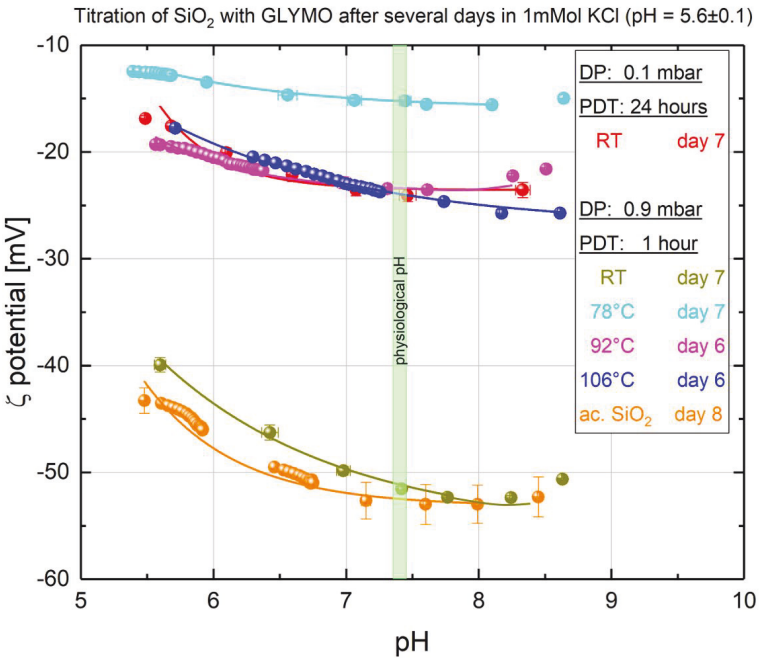

Figure 44: Titration curves of the ζ potential of GLYMO layers deposited on SiO_2 measured 6 to 7 days after gas phase deposition. For comparison the activated SiO_2 (without GLYMO) titration 8 days after activation is added.

4.4 Conclusion

One of the major aims of this work was to improve the molecular layer deposition (MLD) process by integrating a heater to the existing MLD setup. The enhancement and optimization of the process temperature lead to an improvement of the deposition process of GLYMO yielding:

- a faster formation of SAMs (reduction of the PDT from 24 h to 1 h) and
- a better quality of the resulting monolayer.

The work was able to provide further important conclusions:

- A process temperature around 106 °C provides the best results in terms of GLYMO SAM stability and density.
- It is necessary to either provide a long PDT or an elevated deposition temperature to form a chemically bound GLYMO SAM.
- The impact of the temperature on the "deactivation" of activated SiO_2 could be demonstrated.
- At temperatures above 123 °C Si-C bonds in GLYMO are broken and a layer of carbon or silicon seems to form on the substrate.

5 Interface Patterning with GLYMO and PLL

The understanding of the interface between cells and implantable surfaces is one of the keys for the coupling of electrically excitable cells and bioelectronic devices. In the past various approaches to manipulate the cell interaction with biocompatible or bioincompatible surfaces have been introduced in order to control cell growth. There are still many questions, how a surface can ideally be controlled for this purpose. Therefore, the major task in this work was to design, create and prove a patterning method which allows guided cell growth. In chapter 4 the gas phase deposition of GLYMO was discussed and a fast and reproducible MLD process was introduced. The modified gas phase deposition with a process temperature of 106°C (described in section 3.2.2) is used in the following experiments for the deposition of GLYMO on 10 mm x 10 mm SSO substrates (with a SiO_2 thickness of ≈ 23 nm). The samples were patterned with lithography and coated with PLL (described in chapter 3.5.1) in order to grow cortical rat neurons on it. The results of the complex pattering process with GLYMO and PLL are introduced in this chapter, the resulting cell experiments are presented in chapter 6.

5.1 PLL on chemically bound GLYMO SAMs

For the structuring process, for the guided growth, it´s important to start with a stable PLL layer on unpatterned samples. Therefore, a simple PPL drop experiment analyzed with RSE and a long-term ζ potential stability test with SurPASS were performed.

5.1.1 Thickness of PLL on GLYMO

As mentioned in chapter 2.3 the amino group of PLL binds chemically to the epoxy functional group of GLYMO. Therefore, a drop of PLL was deposited on a chemically bounded GLYMO SAM on SiO_2 and for comparison another drop of PLL was deposited on SiO_2 (process described in section 3.5.1). Consequently, the PLL should bind to the molecular layer of GLYMO but not to the plain SiO_2 surface. This behavior is indeed observed (Figure 45).

The PLL binds chemically to the GLYMO SAM but can easily be removed by rinsing with milli-q water from the SiO_2 surface. The simple RSE two layer model for Si and SiO_2, which is described in chapter 3.4.1, is used to obtain the RSE images in Figure 45. This is reasonable since the optical refractive index of GLYMO and PLL (η_{GLYMO} = 1.429; η_{PLL} = 1.414 [23]) doesn't differ drastically from the refractive index of SiO_2 (η_{SiO2} = 1.458). On the GLYMO SAM a PLL layer of roughly 1 nm thickness was observed, whereas on the SiO_2 surface only the dried edges of the PLL drop ("coffee ring effect") could be observed. These measurements confirm the observation of the fluorescence microscopy given in the chapter 4.2.

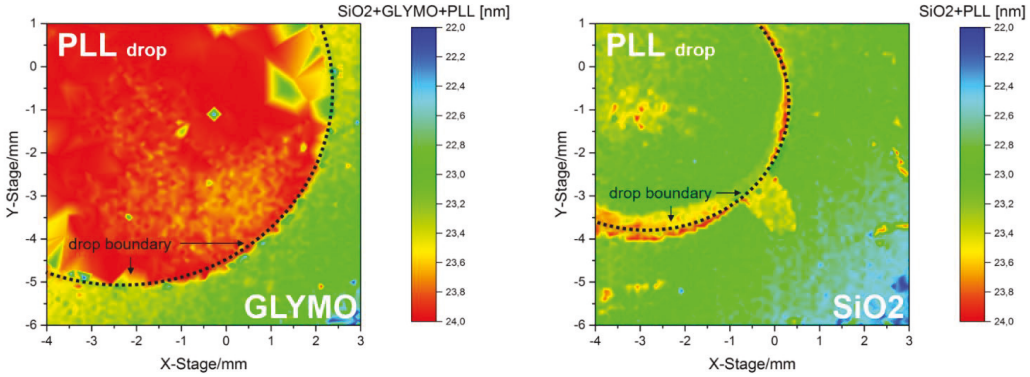

Figure 45: PLL drop of 30 µl (1 mg/ml) on a molecular layer of GLYMO (left) with a PLL thickness of approximately 1 nm and on SiO_2 (right), where just the dried "coffee ring" is visible. In both cases the PLL coating took 1 hour and both samples were rinsed for a few seconds with milli-q water after the coating.

5.1.2 ζ Potential of PLL

In order to analyze the stability of the PLL layer and its impact on the surface potential, ζ potential measurements were carried out on 4 different systems:

a. Activated SiO_2 (after activation stored for 2h at 106 °C and 0.9 mbar)
b. GLYMO (deposited according to section 3.2.2 at a process temperature of 106°C)
c. Activated SiO_2 (after activation stored for 2h at 106 °C and 0.9 mbar) and subsequently coating with PLL (according to section 3.4.3)
d. GLYMO (deposited according to section 3.2.2 at a process temperature of 106°C) and subsequently coating with PLL (according to section 3.4.3)

Right afterwards the samples were placed into the SurPASS device for ζ potential measurements. The results are shown in the Figure 46.

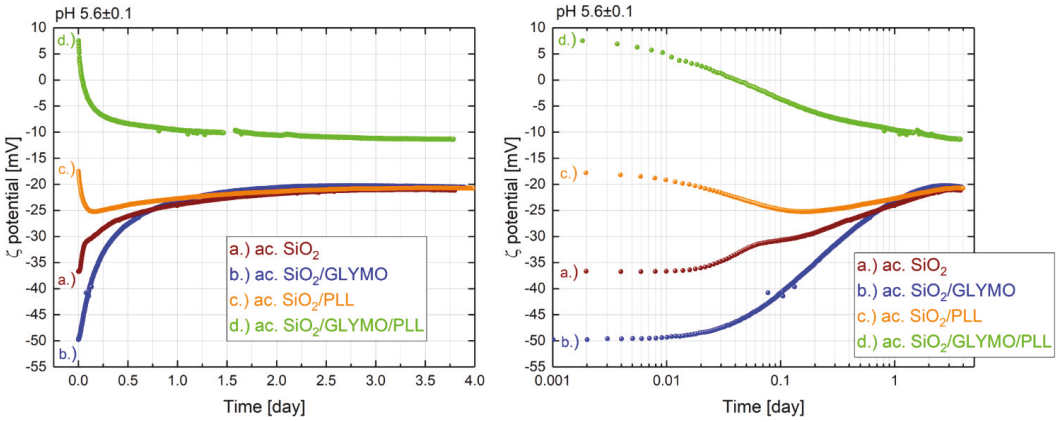

Figure 46: ζ potential of a.) activated SiO_2, b.) SiO_2 with GLYMO layer, c.) activated SiO_2 with PLL coating, d.) SiO_2 with GLYMO layer and PLL coating in linear and semilogarithmic form.

Figure 44 shows two mechanisms:

i. The first mechanism leads to an increase of ζ similar to the behavior of the surface potential of activated SiO_2. It represents the "deactivation" of the underlying activated SiO_2.
ii. The second mechanism leads to an increase of ζ and represents the removal of PLL molecules from the surface, starting with the first exposure to the electrolyte.

The following statements can then be derived for the measured curves:

- The curves (a) and (b), activated SiO_2 and activated SiO_2/GLYMO are dominated by the first mechanism (as already described in chapter 4.3). Here we only observe the deactivation of the substrate.
- Curve (c), activated SiO_2 with PLL is determined by both mechanisms. First, the removal of the PLL molecules from the surface is dominant, starting with the first exposure to the electrolyte (the ζ potential drops from -17 mV to -25 mV) until after about 4.5 hours both mechanisms more or less compensate each other and (the ζ potential increases slowly). After about 24 hours, the ζ potential of the activated SiO_2 determines the behavior (PLL seems to be completely removed). Curve (c) now has the same behavior as curves (a) and (b). All three curves rise until they end at value ≈ -20 mV (ozone cleaned state) after approximately 2 days.
- Curve (d) (activated SiO_2 with GLYMO and PLL) is determined by the mechanism of the removal of PLL molecules from the surface for the complete time. After approx. 24 hours the ζ potential is absolute constant at a final value of -10 mV (the influence of deactivation of activated SiO_2 is not discernible). The enhancement of the ζ potential by 10 mV to a stable value of -10 mV after approximately 24 hours with respect to all other cases is most likely caused by a layer of PLL which is chemically bound to the GLYMO SAM.

In summary, following conclusions can be made:

- In order to chemically bind PLL on SSO substrates chemically bound GLYMO SAM can be used as a linker molecule.
- PLL deposited on activated SiO_2 without such a linker is completely removed in less than 24 hours.
- PLL coated GLYMO SAMs on SSO substrates are stable and shift the ζ potential positively by 10 mV to a final value of approximately -10 mV.

5.2 Pattering Process

One of the most challenging tasks in this work was the implementation of the lift-off process (see chapter 3.5.1.) for the PLL patterning. In order to analyze the success of the patterning process, several control steps were included between the process steps. The detailed lift-off process extended by the control steps consists of the following parts (Figure 47):

(1) Cleaning and activation of the substrate with ozone
(2) GLYMO deposition
(3) Spin-coating of PMMA
(4) E-beam lithography
(5) Development
    - Optical microscope check
    - 1st fluorescence microscope check
(6) PLL deposition
(7) Lift-off
    - 2nd Fluorescence microscope check
(8) Further experiments (e.g. live-dead imaging)

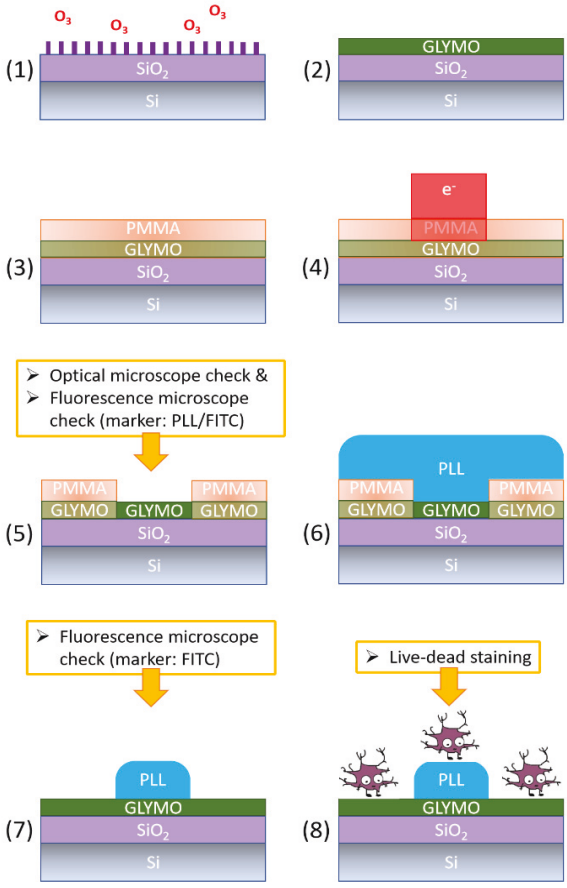

Figure 47: Schematic sketch of the different pattering steps extended by two imaging control procedures after step (4) and after step (6). The last imaging procedure is specified here as live-dead staining (8) shown later in chapter 6.

The complete procedure was performed simultaneously for eight samples, (two samples for the first and two samples for the second check). Although most details of the design were already discussed in chapter 3.5.1 (Figure 32), a brief sketch of the design is always added to the fluorescence microscope images for reason of comparison.

5.2.1 Structure Check after PMMA Development

After e-beam writing and subsequent development of the PMMA, several images were taken with an optical microscope to analyze the results of the lithography (Figure 48).

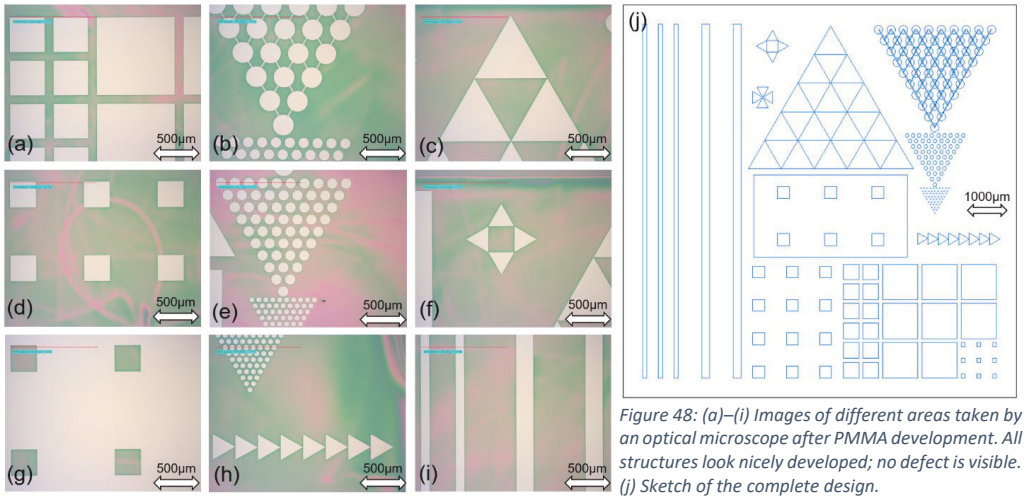

Figure 48: (a)–(i) Images of different areas taken by an optical microscope after PMMA development. All structures look nicely developed; no defect is visible. (j) Sketch of the complete design.

The optimized dose (500 µC/cm^2) for the lithography on SSO substrates was chosen based on the dose test (section 3.3.2). According to the optical microscope pictures this seems to be reasonable as well for SSO substrates with a chemically bound GLYMO SAM. The negative pattern (lift-off) is everywhere clearly noticeable (Figure 48). For further investigations fluorescence microscope pictures were taken after the development of PMMA. For this purpose, the samples were coated with PLL/FITC (according to section 3.4.3). The PLL/FITC marker should only bind to the GLYMO at the open areas, which are visible as brighter structures in Figure 49, whereas it should not bind at areas covered with PMMA leading to darker areas in Figure 49.

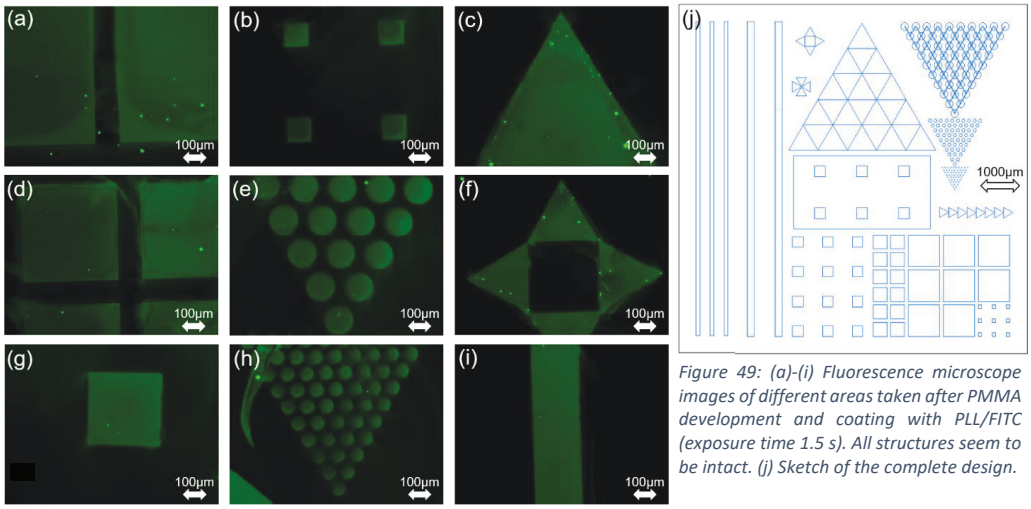

Figure 49: (a)-(i) Fluorescence microscope images of different areas taken after PMMA development and coating with PLL/FITC (exposure time 1.5 s). All structures seem to be intact. (j) Sketch of the complete design.

As observed in Figure 49 the e-beam seems to crack the PMMA polymer structure but doesn't harm the chemically bound GLYMO SAM. The SAM even survived the PMMA development with the developer and propanol. However, this behavior seems to not be valid for all structures as shown in Figure 50.

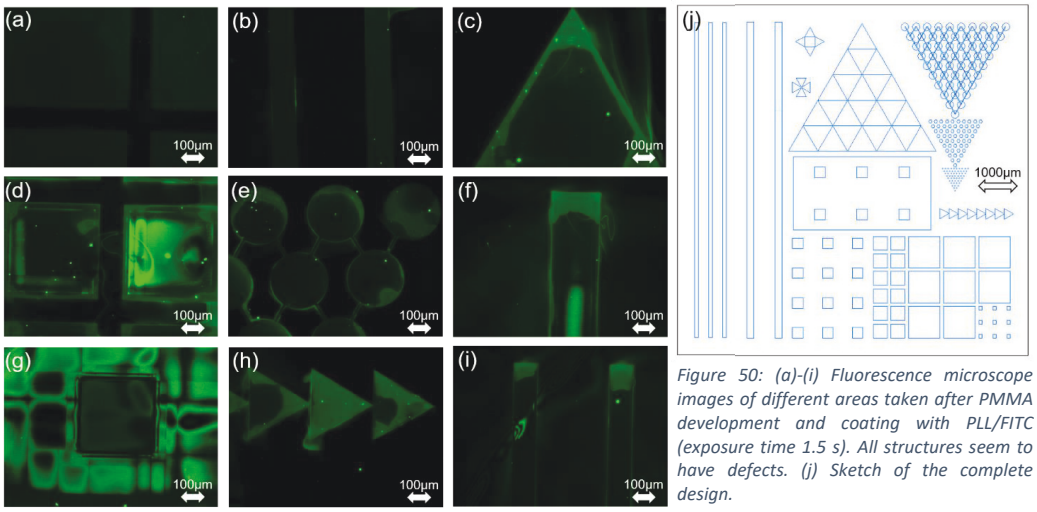

Figure 50: (a)-(i) Fluorescence microscope images of different areas taken after PMMA development and coating with PLL/FITC (exposure time 1.5 s). All structures seem to have defects. (j) Sketch of the complete design.

Two interesting effects are visible on some structures in Figure 50:

- The fluorescence of some PLL/FITC-marked GLYMO areas is nearly invisible which indicates that GLYMO is removed or that there is still a thin PMMA layer on the GLYMO SAM which prevents the binding of PLL to the GLYMO.
- The typically writing structure of the e-beam are visible in some areas where no PMMA should be present. This support the assumption that some PMMA is left over on the GLYMO SAM (Figure 50 (d) and (g)).

One possible explanation for the structural defects might be that GLYMO works as an "epoxy adhesive" layer for the cracked PMMA molecules. Epoxy adhesives are created by polymerizing a mixture of two starting compounds, the epoxy resin in our case GLYMO and the hardener, here cracked PMMA. When epoxy resin is mixed with a specified catalyst, curing is initiated and PMMA therefore could not be removed completely during the development process.

One other explanation might be that due to the dose correction the proximity effect had led to a dose which is too small for large areas and therefore the PMMA molecules were not completely cracked and removed.

5.2.2 Structure Check after Lift-off

As already discussed in the previous section, there is a tendency that some structures are perfectly patterned and other have vanish completely or are not homogenously developed. This can be observed as well in Figure 51. The images were taken after the complete pattering process. For these images the PLL on the GLYMO SAM was marked with FITC. Again, some structural features vanish completely like the larger circles in Figure 51 (e) and others just show features at the structural borders like the triangles in Figure 51 (i). In addition to the explanation given in the previous section, some structural defects can be associated with the PLL coating process itself. The borders of the structures have a higher intensity consequently the amount of PLL might be thicker at structural borders. This might be a consequence of the "coffee ring" effect if PLL sticks to the PMMA at the edge of a structure, cannot be removed by the washing with milli-Q water, and, subsequently, dries to a thick PLL layer.

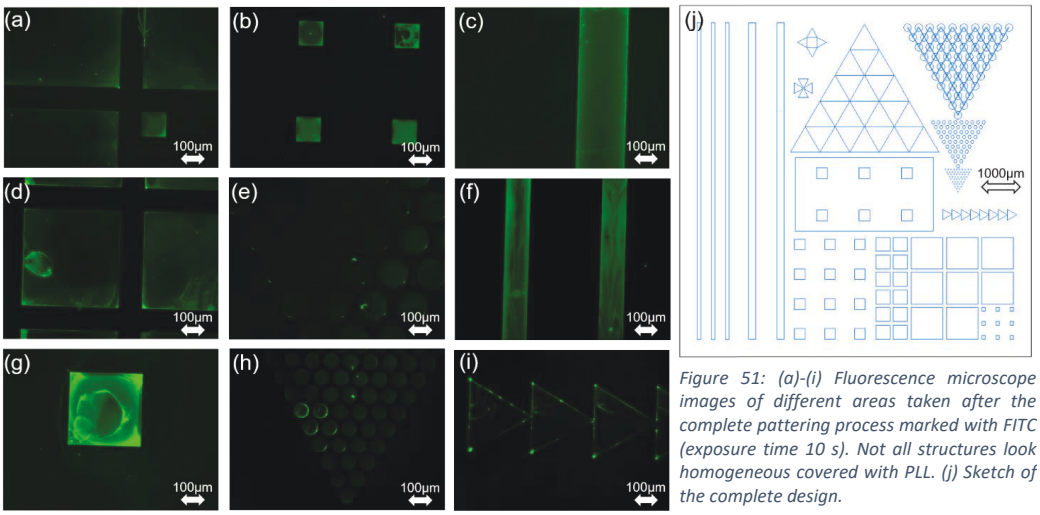

Figure 51: (a)-(i) Fluorescence microscope images of different areas taken after the complete pattering process marked with FITC (exposure time 10 s). Not all structures look homogeneous covered with PLL. (j) Sketch of the complete design.

In order to identify the PLL in the structures, a background correction was performed. For this purpose, the intensity of a 100 µm x 100 µm area without PLL was averaged for each image and defined as an intensity threshold for the presence of PLL. This should make it possible to analyze to what extent PLL still exists within the structures or whether PLL exists at all. In addition, line scans over the structural features were taken which could provide indications for the local PLL density distribution. The results are shown in the following.

Let's start with the analysis of the 100 µm and 200 µm bar structure (Figure 52) which can be summarized in three points, assuming that the fluorescence intensity is related to the PLL density/thickness:

- The bars seem to be homogenously covered with PLL according to the homogenous distribution of the fluorescence intensity.
- However, smaller bars (100 µm) have a higher intensity (average ≈ 60) than bigger bars (200 µm with average ≈ 40).
- Moreover, the edges of the structure show significantly higher intensity compared to the center. This could again be explained by the coffee ring effect.

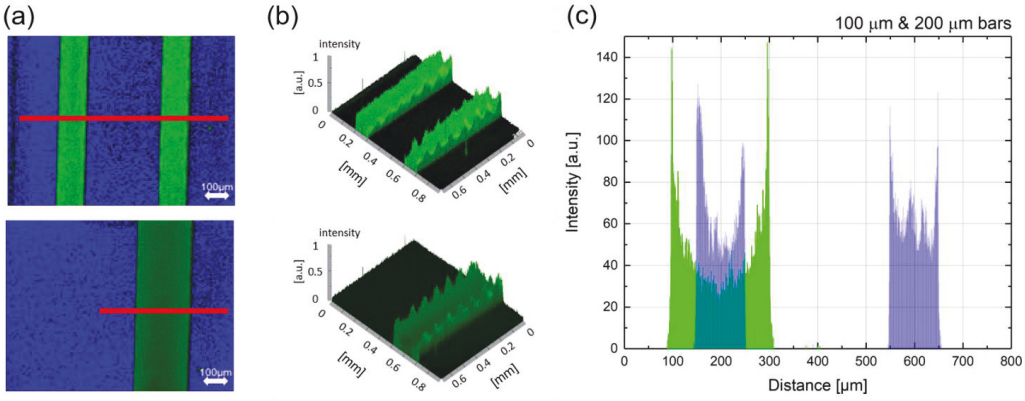

Figure 52: (a) Background subtracted fluorescence microscope images of 100 µm and 200 µm bars recorded after the complete pattering process. The red lines indicate the position of the profile scan line of the intensity which is plotted in (c). Images (b) show a 3D image of the intensity distribution of (a).

Let´s continue with the analysis of the square structures which a side length of 100 µm, 300 µm, 400 µm and 900 µm. Figure 54 shows a comparison of these structures. Based on the intensity profile scan lines in Figure 54 (c), for each side length a profile scan line of 200 µm (located in the middle of the structure) is taken (in the 100 µm square the central 80 µm) and averaged. The resulting intensity thus obtained is plotted in Figure 53 against the side length of the squares. The values obtained are in line with a linear fit.

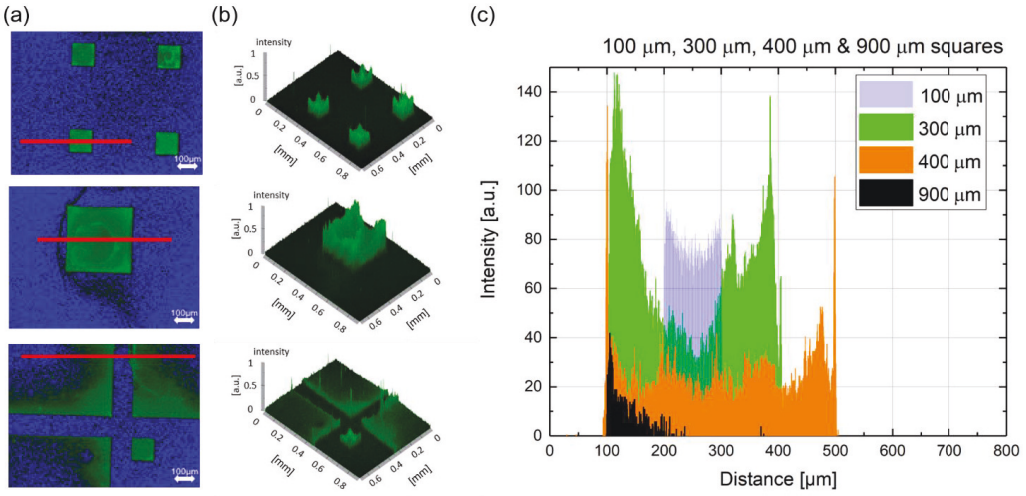

Figure 54: (a) Background subtracted fluorescence microscope images of 100 µm, 300 µm and (partially) 900 µm squares recorded after the complete pattering process. The red lines indicate the position of the profile scan line of the intensity which are summarized in (c). Images (b) show a 3D image of the intensity distribution of (a).

The observations of the squared structures can be summarized in three points:

- 100 µm, 300 µm & 400 µm squares are completely covered with PLL, whereas the large 900 µm squares are not completely covered with PLL. The latter show areas without PLL inside the structure (Figure 54 (a)).
- Smaller squares show a higher intensity than bigger squares (Figure 53). This is similar to the observation for the bars, where also the smaller structures had a higher fluorescence intensity.
- Also, the edges of the structure show a significantly higher intensity ("coffee ring effect").

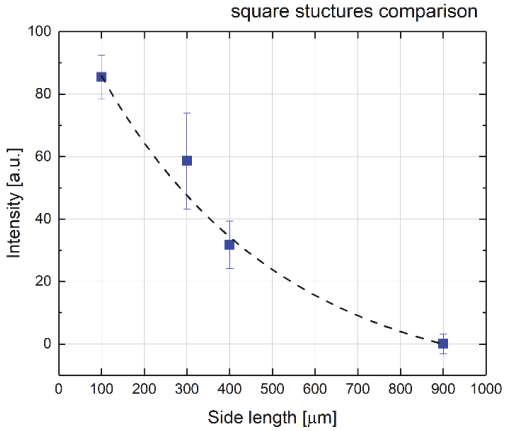

Figure 53: Average fluorescence intensity inside the squared structures plotted as a function of the side lengths for the data shown in Figure 54 (c). Dashed line is the resulting exponential decay fit.

Finally, the analysis of the circles (diameter 120 µm) and of the equilateral triangles (side length 300 µm) (Figure 55) can be summarized in two statements:

- The circle structures show a distribution of measurable PLL. According to the profile scan line of the circle structure in Figure 55, the first circles still have a measurable intensity, however already the 3rd circle shows no measurable intensity. It is not clear what causes this gradual change in the PLL coating.
- The triangle structure shows a significantly higher intensity ("coffee ring effect") at the edges and specially at the corners, whereas no fluorescence intensity can be observed is inside the triangles.

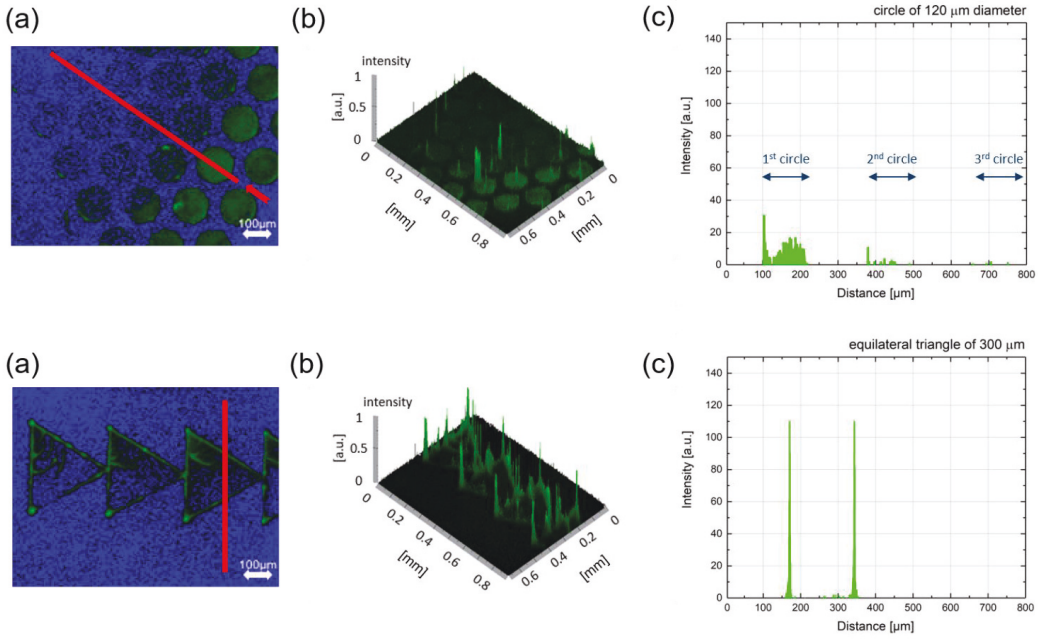

Figure 55: (a) Background subtracted fluorescence microscope images of circle structure (120 µm diameter) and equilateral triangle structure (side length 300 µm) recorded after the complete pattering process. The red lines represent the position of the profile scan line of the intensity in (c). Images (b) show 3D image of the intensity distribution of (a).

5.3 Conclusion

A patterned interface consisting of bio compatible and bio incompatible (even toxic) components is the key to guided cell growth. In this chapter we demonstrated the lithographic patterning of SiO_2 with GLYMO (bio incompatible) and PLL (bio compatible). In terms of this approach of interface tailoring, we can make the following statements to the two major points in this chapter:

PLL on chemically bound GLYMO SAMs:

- In order to bind PLL chemically on SSO substrates, GLYMO SAMs seems to be a perfect choice as linker interface to SiO_2. Furthermore, the PLL on GLYMO SAMs shifts the ζ potential positively by 10 mV to a stable final value of -10 mV which improves the cell adhesion.

Pattering Process:

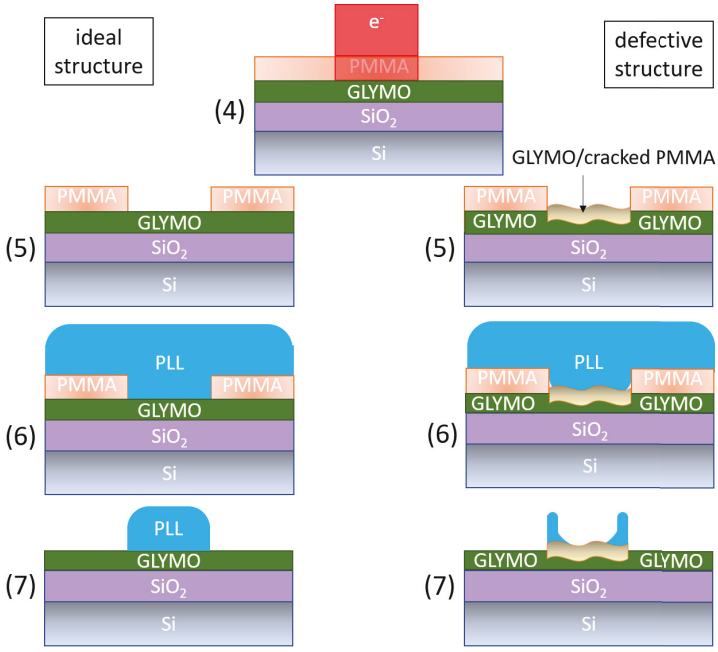

Figure 56: Schematic of the last pattering steps (patterning described in section 3.5.1). The final state of PLL on GLYMO coated SSO after the complete pattering process depends on how many cracked PMMA molecules bind to the epoxy terminated GLYMO SAM. Left the ideal case is shown while on the right side the final state with cracked PMMA leftovers prevents the binding of PLL to the GLYMO SAM.

- With the pattering process introduced in this work we have proven that it is possible to create PLL patterns on GLYMO. The lithographical and lift off process is particularly well suited for structures from 20 µm - 400 µm, while larger structures partially show areas which are not completely covered with PLL. Based on further investigation (via fluorescence microscopy) during the pattering process we assume that some cracked PMMA is left over on the GLYMO SAM which prevents the binding of PLL to the GLYMO (situation sketched Figure 56).

In the next chapter the cell growth on these patterned samples is analyzed. It has to be expected that the cells grow according to the PLL patterned structure, but the cells might also be affected by the structural effects (and defects) which were discussed in this chapter. Therefore, the cell growth experiment will be used on the one hand as an indicator for the quality of the structured layers (of GLYMO and PLL) and on the other hand it can confirm the assumptions that cracked molecular left over of PMMA bind to the epoxy functionalized GLYMO SAM and hinders the formation of bio friendly PLL layers (see Figure 57).

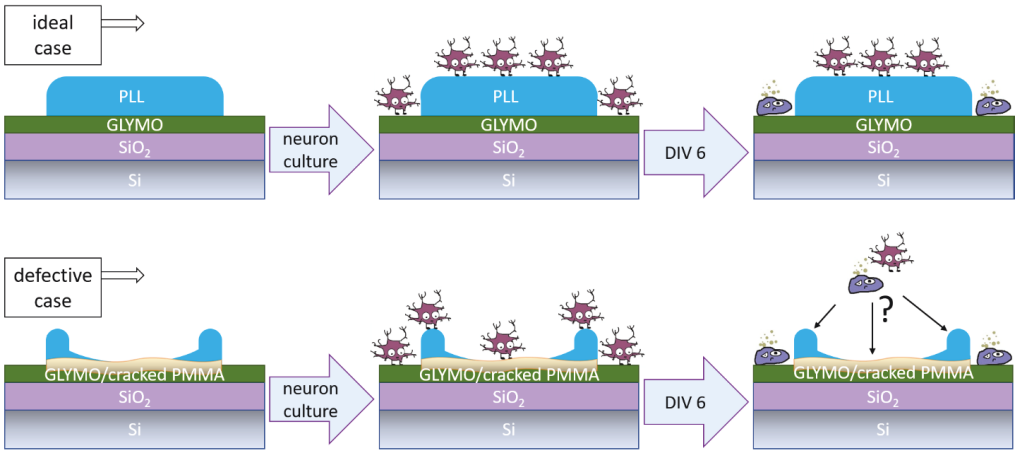

Figure 57: Schematic sketch of the final state after the pattering process, then covered with neuron cells and finally observed after DIV 6. First the ideal case and below the defective case, where the neuron growth can provide further information about structural defects off PLL

6 Guided Neuron Growth

In order to study the cell adhesion, the immobilization of neurons and guidance of neurite outgrowth on the PLL and GLYMO patterned substrates which were in detail discussed in the previous chapter, cortical rat neurons were prepared (section 3.5.2) and placed on the patterned substrates. After day in vitro 6 and live/dead staining (according to section 3.4.3), the neurons were stained and subsequently carefully examined with fluorescence microscopy. It is to be expected that the cells grow according to the PLL patterned structure, but the cells might also be affected by the structural defects which were discussed in the previous chapter. Therefore, cell growth in this chapter is not only used as prove of guided cell growth. It is also used as an indicator for the quality of the (patterned) layers and proof of structuring defects. In the following the resulting images of the neurons are presented.

6.1 Neuron Density

In order to obtain an first idea about the neuron density in our PLL coated structures and thus to make conclusions about biological compatibility, two intact 900 µm x 900 µm ($1.947 \cdot 10^6$ pixels) square structures (Figure 58) were selected.

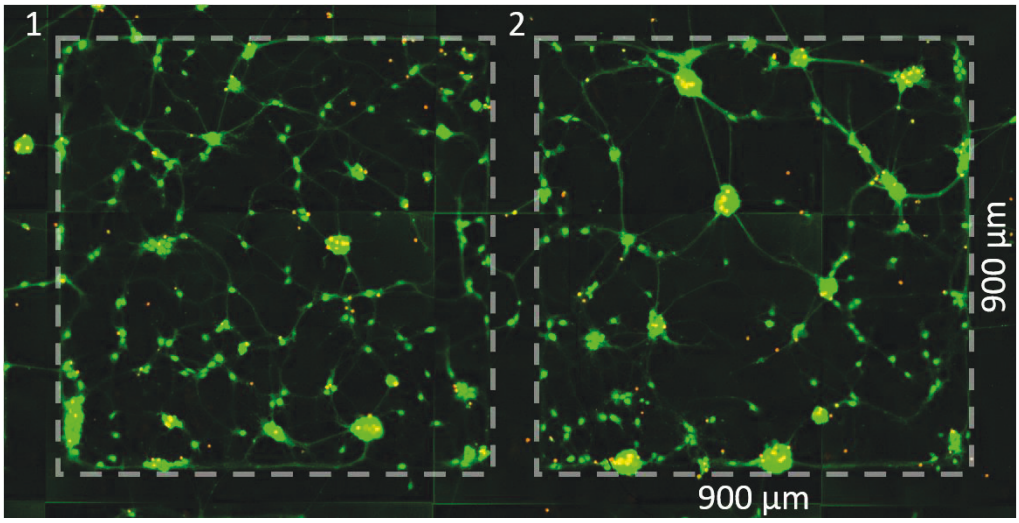

Figure 58 Images of a GLYMO coated and PLL patterned SSO substrate with cortical rat neurons (patterning according to chapter 3.5.1). Live cells are stained with calcein-AM (green), dead cells with ethidium homodimer (orange) after DIV 6. Here the focus lies on two the squares structures with a side length of 900 µm for cell counting. Grey dashed lines symbolize the outline of the expected PLL layer.

The evaluation of the neuron density was performed according to the procedure described in section 3.5.3 (pixels per neuron are 516). An overview of the obtained variables (given in the following table) starts with the number of pixels associated with neurons, followed by the number of neurons in area 1 and 2, and finally the density of the neurons (pixel) is given. This number can be compared with the number of neurons counted by eye. Furthermore, the initial seed density is listed at the end of the table.

	Area 1	Area 2
Pixels above the threshold	$0.238 \cdot 10^6$	$0.348 \cdot 10^6$
Neurons (pixel)	461	675
Neuron density (pixel) [k/cm^2]	56.9	83.3
Neurons (eye)	≈ 440	≈ 520
Neuron density (eye) [k/cm^2]	$\approx$ 54.3	$\approx$ 64.2
Seed density [k/cm^2]	250	250

If we take and average value of the neuron density based on the pixel counting (≈ 70 k/cm^2) or based on the counting by eye (≈ 60 k/cm^2), 24 - 28 % of the nominal seed density (250 k/cm^2) are alive at day in vitro 6. This is in good agreement with the literature [24] and confirms the assumption that the PLL patterned areas can be accepted as bio friendly environment for neuronal cells.

6.2 Guided Growth in Various Structures

Guided Growth in Bar Structures

We start with the analysis of the 100 µm and 200 µm PLL coated bar structures in Figure 59 and Figure 60.

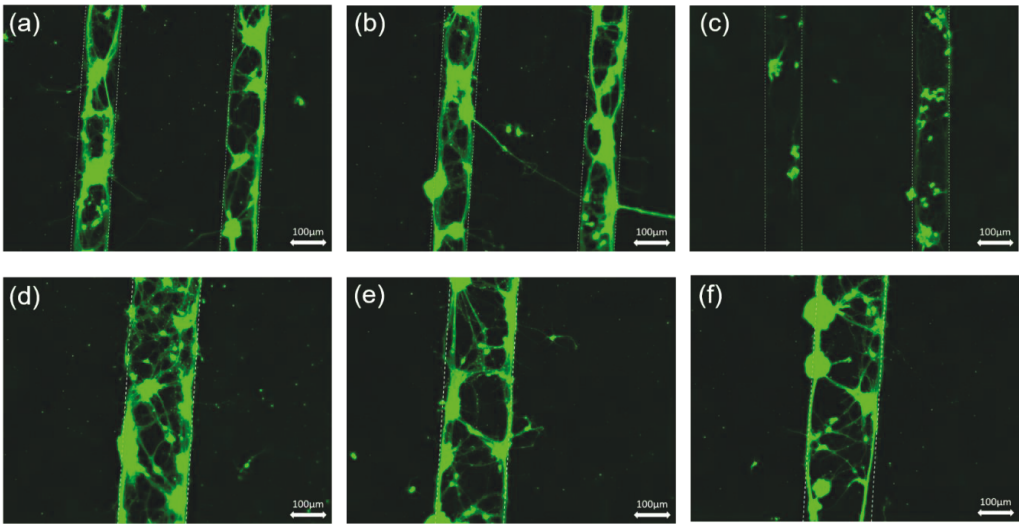

Figure 59: Images (a) to (f) show a 900 µm x 670 µm area of a GLYMO coated and PLL patterned SSO substrate with cortical rat neurons (patterning according to chapter 3.5.1). Only live cells are stained here with calcein-AM after DIV 6. Here the focus lies on the bar structure with a width of 100 µm and 200 µm (complete structural design shown Figure 32). White dashed lines symbolize the outline of the expected PLL layer.

The observations in these bar structures can be summarized in four points:

- Guided neuron growth is observable inside “PLL bars” (with a width of 100 µm and 200 µm) over distances of several millimeter.
- Structural edges have a slightly higher neuron density which coincide with the observance that there is a higher PLL density expected (section 5.2.2).
- Structural defects, as observed in the chapter before, might have reduced the neuron growth which is specially seen in Figure 59 (c) and Figure 60.
- Nearly no living cells exists on areas which are supposed to be covered with GLYMO.

Thus, guided neuron growth is possible in the bar structure (width 100 µm and 200 µm) even over several millimeter (Figure 60). According to the design the bars have a total length of 9 mm. But based on structural defects, which are discussed in the chapter before, it can be observed that the guided growth is terminated if the PLL pattern is interrupted or vanished (Figure 60).

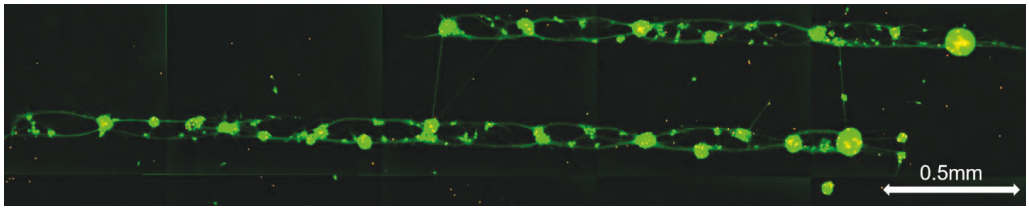

Figure 60: Images of a GLYMO coated and PLL patterned SSO substrate with cortical rat neurons (patterning according to chapter 3.5.1). Live cells are stained with calcein-AM (green), dead cells with ethidium homodimer (orange) after DIV 6. Here the focus lies on the two bars (with a width of 100 µm).

Guided Growth in Square Structures

Now, we continue with the analysis of the square structures (side length from 100 µm to 900 µm). Figure 61, Figure 62 and Figure 64 show an typical example of the guided neuron growth in these structures.

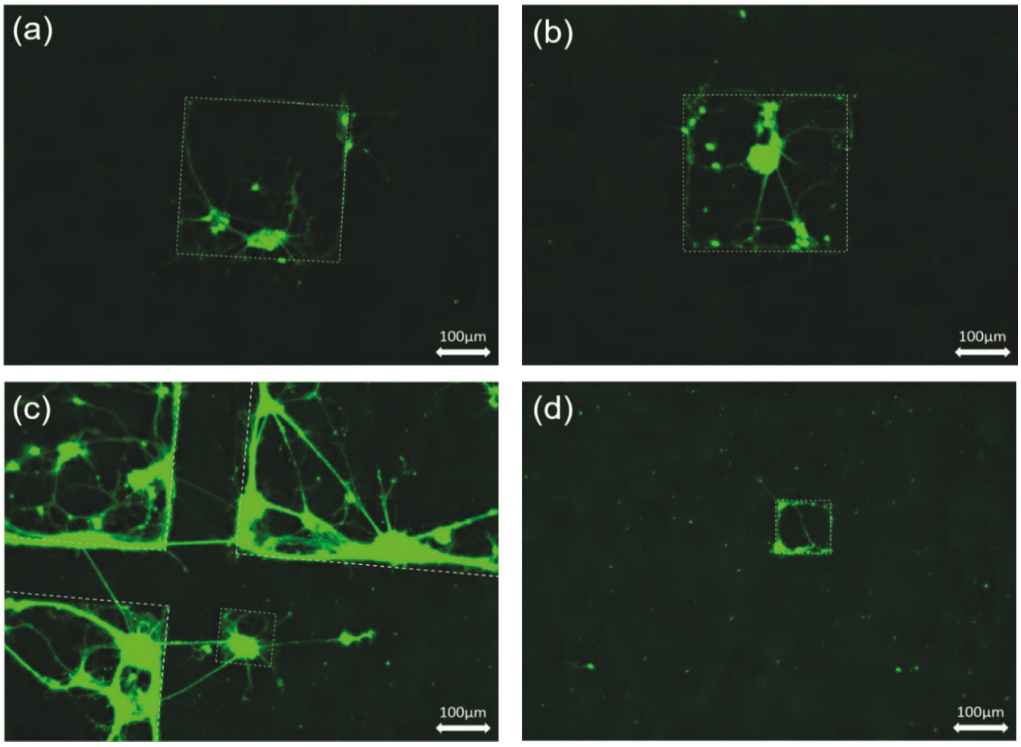

Figure 61: Images show a 900 µm x 670 µm area of a GLYMO coated and PLL patterned SSO substrate with cortical rat neurons (patterning according to chapter 3.5.1). Only live cells are stained here with calcein-AM after DIV 6. The focus lies in (a) and (b) on a square structure with a side length of 300 µm, in (c) corner of three 900 µm squares connected with a complete 100 µm square and in (d) a single 100 µm square covered with neurons. White dashed lines symbolize the outline of the expected PLL layer.

The observations on the squared structures for guided neuron growth, can be summarized as follows:

- Neurons grow inside the small squares (100 µm, 300 µm & 400 µm) which coincides with the observation in the previous section that these structures are completely covered with PLL.
- In contrast the large 900 µm squares are not completely covered with PLL and show consistently some areas without neurons inside the structure (Figure 63). Thus, vanishing of PLL structure details seems to be reproduced (Figure 64 (a) and Figure 63).
- Nearly no living cells on areas which are only covered with GLYMO (i.e. no additional PLL).

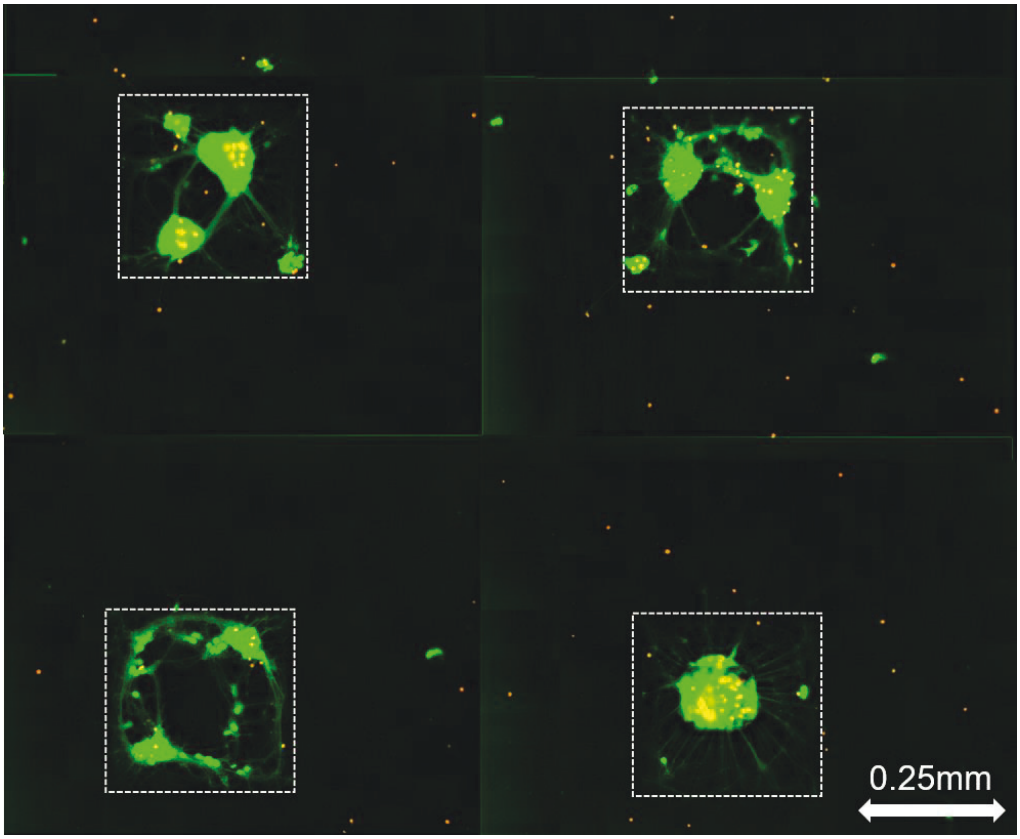

Figure 62: Images of a GLYMO coated and PLL patterned SSO substrate with cortical rat neurons (patterning according to chapter 3.5.1). Live cells are stained with calcein-AM (green), dead cells with ethidium homodimer (orange) after DIV 6. Here the focus lies on four squares with a side length of 300 µm. White dashed lines symbolize the outline of the expected PLL layer.

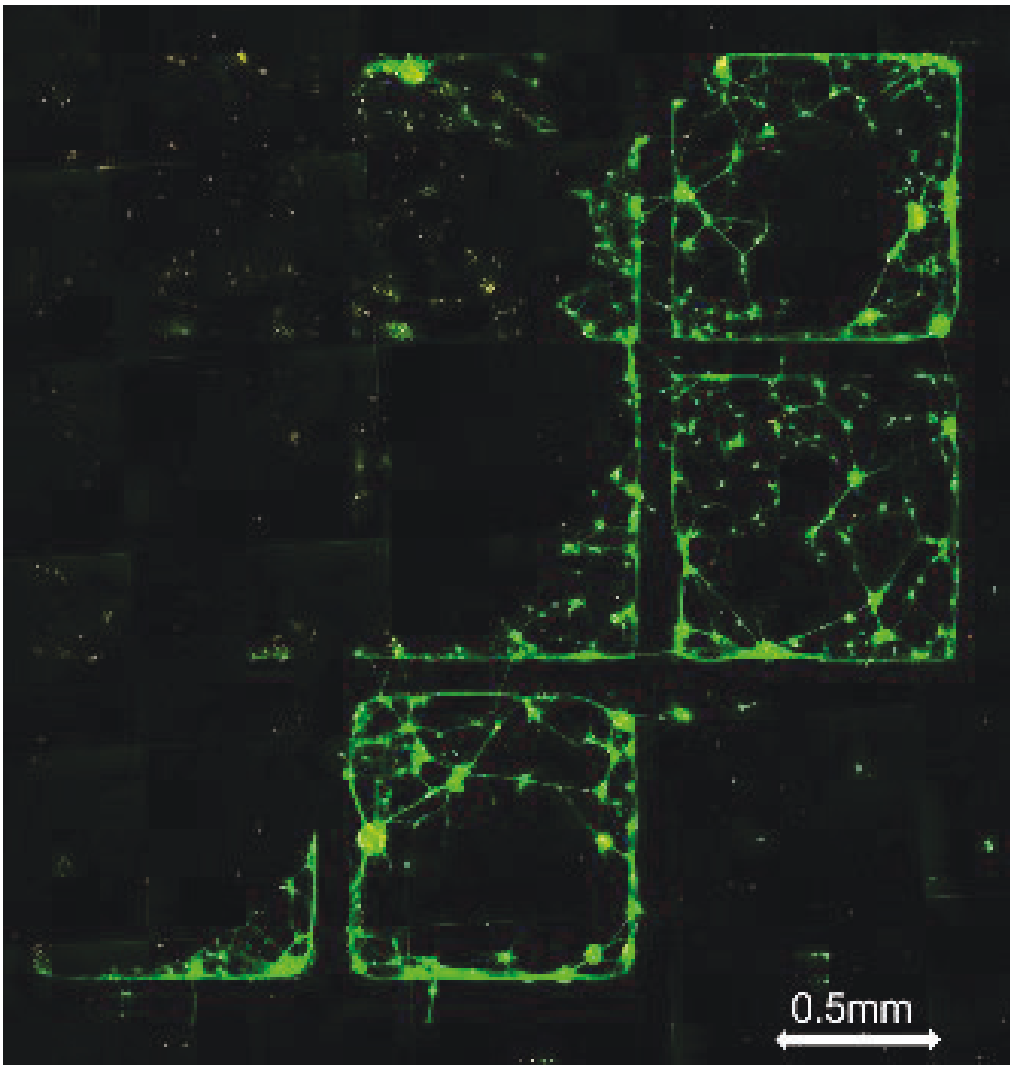

Figure 63: Images of a GLYMO coated and PLL patterned SSO substrate with cortical rat neurons (patterning according to chapter 3.5.1). Live cells are stained with calcein-AM (green), dead cells with ethidium homodimer (orange) after DIV 6. Here the focus lies on the square structures with a side length of 900 µm.

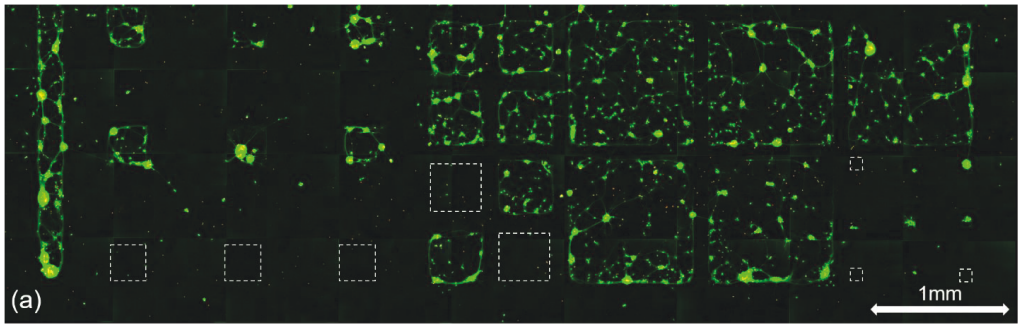

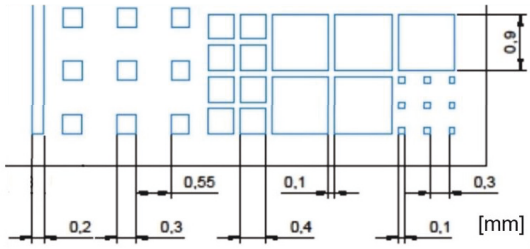

Figure 64: (a) Images of a GLYMO coated and PLL patterned SSO substrate with cortical rat neurons (patterning according to chapter 3.5.1). Live cells are stained with calcein-AM (green), dead cells with ethidium homodimer (orange) after DIV 6. Here the focus lies on the square structures. (b) As an orientation, a cutout of the structuring design.

Guided Growth in circle and triangle Structures

Finally, the analysis of the neuron cell growth inside the circles (diameter 60 µm, 120 µm and 240 µm) and inside the equilateral triangle (side length 300 µm) structures is presented. In contrast to the line and square structures, the circular structures are not so clearly marked, and more structural details are missing (Figure 66). This tendency can be observed in the circles with a diameter of 240 µm (Figure 65).

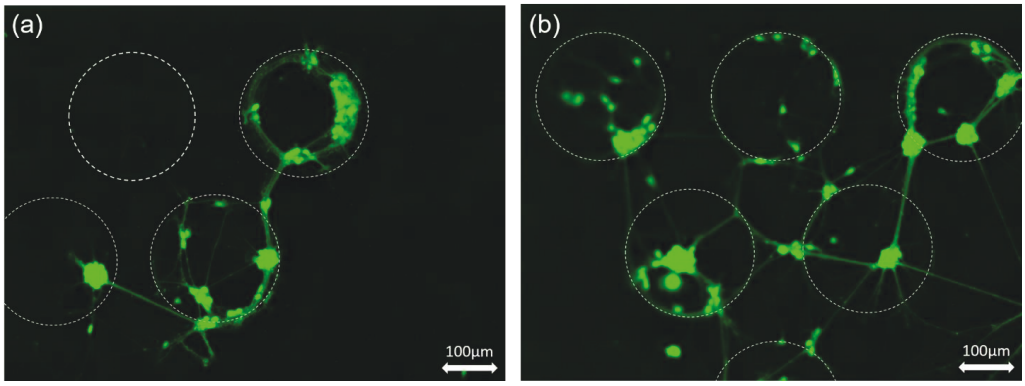

Figure 65: (a) and (b) Images show a 900 µm x 670 µm area of a GLYMO coated and PLL patterned SSO substrate with cortical rat neurons (patterning according to chapter 3.5.1). Only live cells are stained here with calcein-AM after DIV 6. The focus lies on the circle pattern with a 240 µm diameter. White dashed lines symbolize the outline of the expected PLL layer.

Additionally, a figure of guided neuron growth in circles of 60 µm and 120 µm is shown in Figure 66.

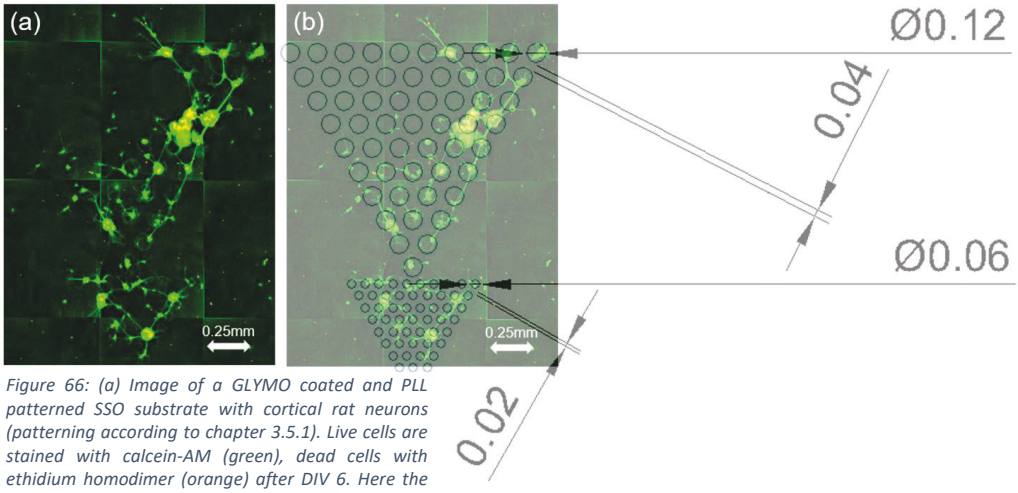

Figure 66: (a) Image of a GLYMO coated and PLL patterned SSO substrate with cortical rat neurons (patterning according to chapter 3.5.1). Live cells are stained with calcein-AM (green), dead cells with ethidium homodimer (orange) after DIV 6. Here the focus lies on the circle structures of 60 µm and 120 µm diameter. (b) Same image with a superimposed template of the expected PLL layer.

To sum up the observations of guided neuron growth in PLL patterned circles in Figure 65 and Figure 66, the following four points can be made:

- A clear guided neuron growth inside circles with 60 µm diameter (comparable to the size of a neuron) with a distance between the circles of 20 µm is hardly possible. The distance is too small, neurons and neurospheres partially occupy several “PLL islands” (Figure 66).
- Guided neuron growth inside circles of 120 µm and 240 µm diameter with a distance between the circles of 40 µm respectively 80 µm is partially realized (Figure 65 and Figure 66).
- However, in accordance with the observation in the previous chapter that some of the PLL structured circles vanished, there is no neuron growth present in some the large circles (Figure 65 and Figure 66).
- Again, hardly any living cells grow on areas which are exclusively covered with GLYMO.

Finally, neuron growth on the PLL coated equilateral triangle (side length 300 µm) are shown (Figure 67).

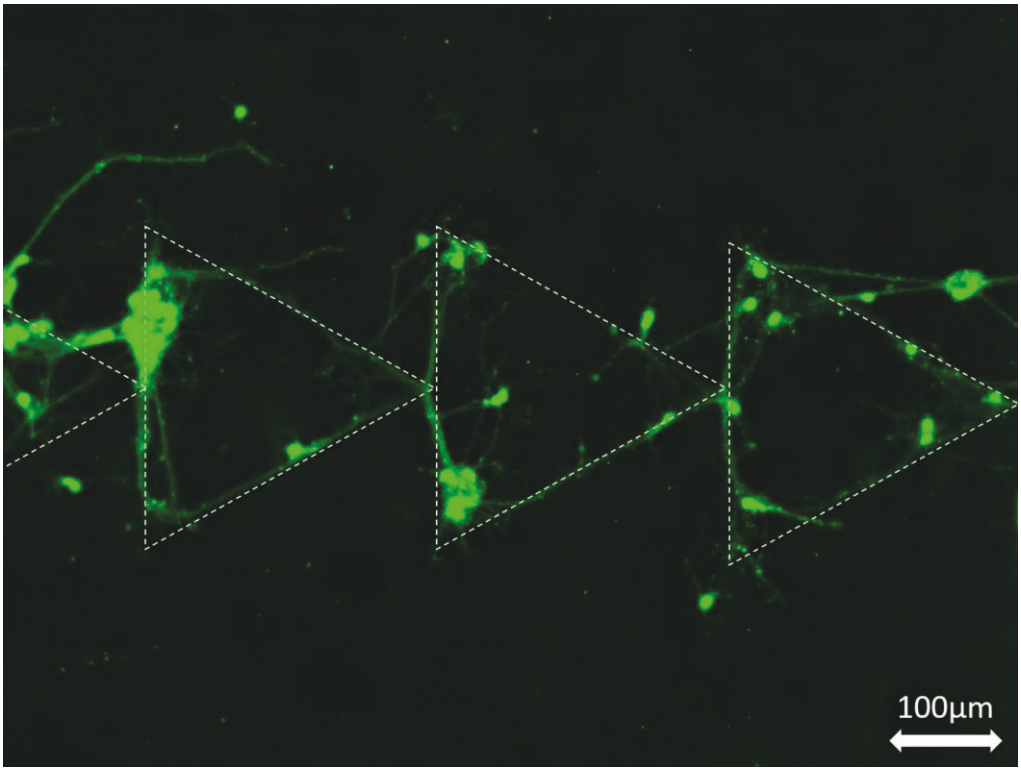

Figure 67: Image shows a 900 µm x 670 µm area of a GLYMO coated and PLL patterned SSO substrate with cortical rat neurons (patterning according to chapter 3.5.1). Only live cells are stained here with calcein-AM after DIV 6. The focus lies on the equilateral triangle pattern with a side length of 300 µm. White dashed lines symbolize the outline of the supposed PLL layer.

The resulting neuron growth is a consequence of the PLL profile shown in the previous chapter (see Figure 55) and leads to the following statement.

Since there is no PLL coating inside the triangles, as shown in the analysis in section 5.2.2, there is almost no neuron growth in the center of the triangle. However, the observed high intensity of PLL at the edges and specially at the corners, is in coincidence with the observed neuron growth at these positions as shown in Figure 67.

6.3 Structural Defects

According to the analysis based on the structures in the previous section, three effects can be observed which seem to affect the structuring process:

i. The epoxy functionalized GLYMO SAM seems to behave as an “epoxy adhesive” layer cracked (e-beam) PMMA molecules and prevents chemically binding of the PLL.
ii. The shape of the structure itself affects the pattern process (round edges of circles vs. sharp angles of triangles or small areas of 0.1 mm^2 vs big areas of 1 mm^2). Depending on the shape, different kinds of “coffee rings” and thicknesses of PLL are formed.
iii. The PLL coating itself creates a “big coffee ring” on the 10 mm x 10 mm SSO sample so that a coffee ring structure of dried PLL is formed close to the edges of the sample.

In the following, the different observations are descriptively explained.

The “epoxy adhesive” effect

The epoxy functionalized GLYMO SAM works as an “epoxy adhesive” layer for the cracked PMMA molecules. As a consequence, cracked PMMA is bound on the GLYMO SAM which actually prevents the binding of PLL to GLYMO (sketched in Figure 68 (a)).

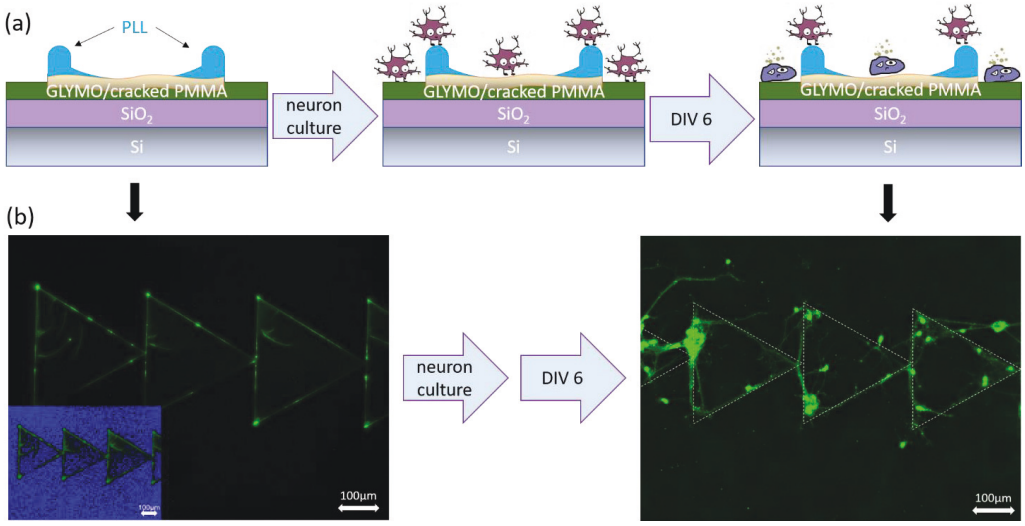

Figure 68: (a) Schematic sketch of the final state after the pattering process, then covered with neuron cells and finally observed after DIV 6. (b) Original fluorescence microscope pictures, where left areas marked with FITC PLL are shown and right stained live neuron cells.

The “small coffee ring” effect

Additionally, edges of the structures have a higher thickness of PLL. This might be a consequence of the “small coffee ring” effect. If PLL sticks to the PMMA at the edges of a structure, it cannot be removed by the washing with milli-Q water, and, subsequently, dries to a thick PLL layer. This effect depends on the structure itself and is larger for edges which sharp angels (triangle structure) than for round shapes (circle structure) or for small areas (0.1 mm^2 compared to larger ones of 1 mm^2). The growth and density of the neurons confirm these observations, both are significantly increased at the structural edges. An example is shown in Figure 68 (b).

The “big coffee ring” effect

As mentioned, the PLL coating itself forms a “big coffee ring” on the substrate. A ring structure of dried PLL is formed during the wet coating process close to the edges of the sample. The wet coating of PLL on GLYMO (section 3.4.3) lasts for 1 hour. During this time the PLL drop shrinks and leaves a dried “big coffee ring” of PLL. For the sake of understanding the situation is slightly exaggerated in Figure 69.

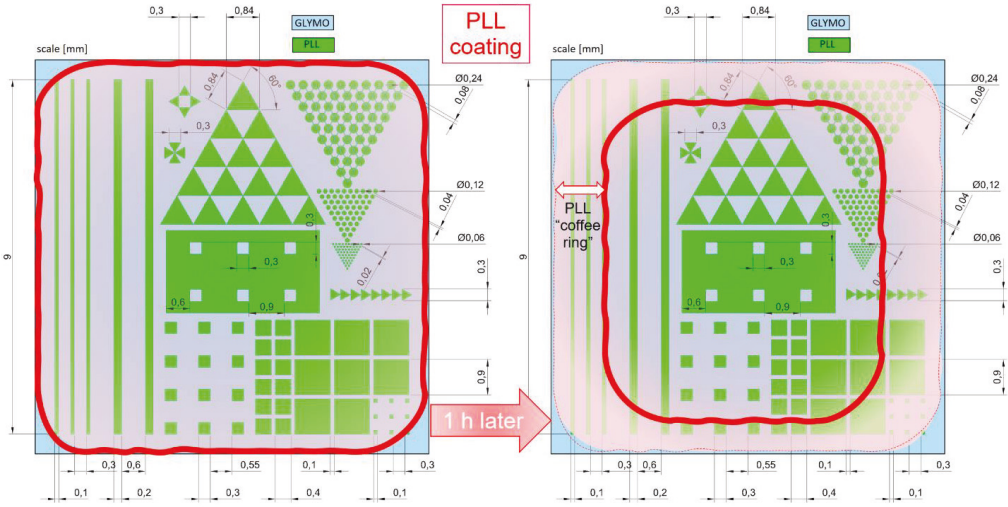

Figure 69: Schematic of the pattering step (6), the PLL coating (process described in section 3.5.1). Left the situation is shown at the beginning of the PLL wet coating and right the same situation after 1 hour, a “coffee ring” of dried PLL is formed. For the sake of understanding the situation is slightly exaggerated sketched.

Structural features that are within the dried "big coffee ring" have a high thickness of PLL. The dried PLL stays on the lithographically opened areas (green areas in Figure 69) while the dried PLL on PMMA (blue areas in Figure 69) was completely removed after PMMA lift-off. The growth of neurons shows that structures close to the "big coffee ring" of PLL are preferred (Figure 70). In contrast, neuronal growth at the center of the test structure was barely noticeable which is in

accordance with the assumption that the cracked PMMA molecules react and bind to the epoxy group of GLYMO and prevents therefore the chemical binding of PLL.

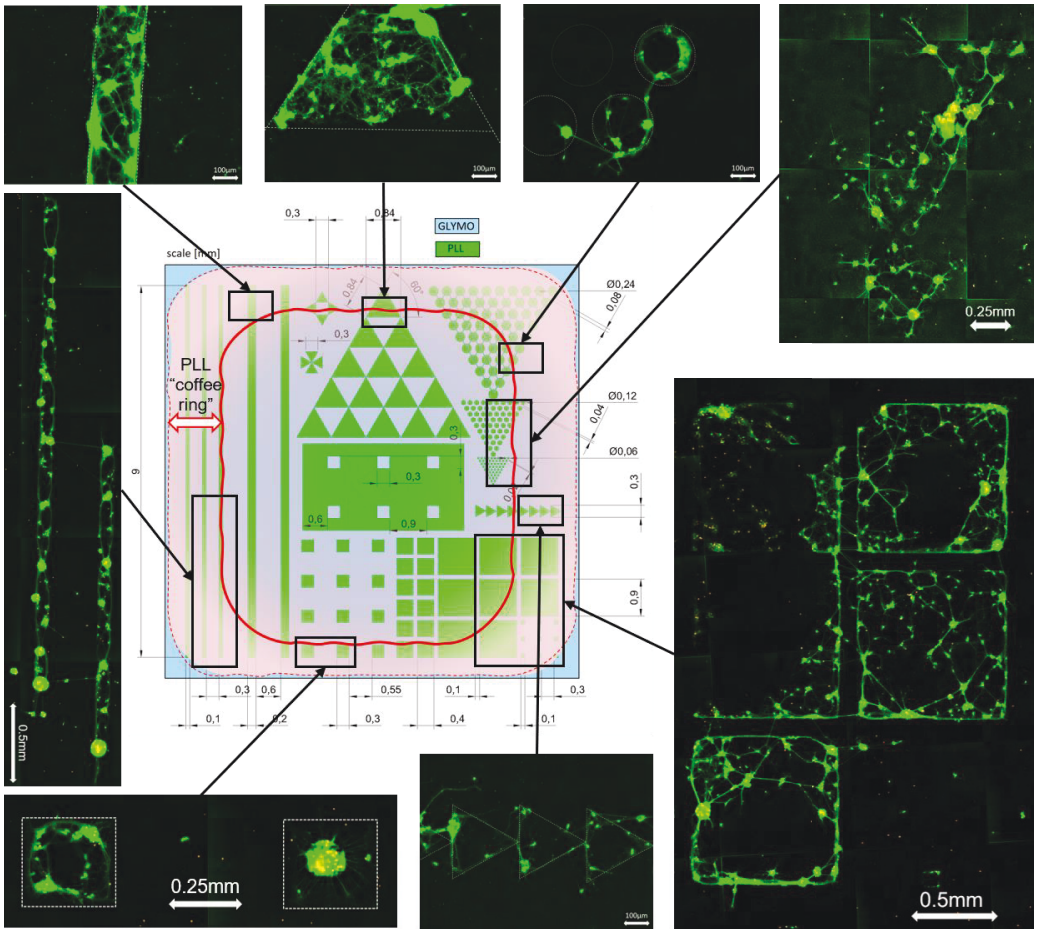

Figure 70: Analog to Figure 69 the "coffee ring" after 1 hour of wet coating shrinks to the center of the test structure. This is symbolized by the red line inside the test structure. Neuron growth was mainly observed close to the drop border of the "big coffee ring" of PLL whereas at the center of the test structure neuronal growth was barely noticeable. In an exemplary way, eight observed areas of guided growth are added. All fluorescence microscope images are close in the vicinity to the "big coffee ring" and show stained neuron after DIV 6.

6.4 Conclusion

In this chapter is could be shown that the in section 3.5.1 presented patterning process might be suitable to bio applications. Nevertheless, there are also some shortcomings. The interface modification via a chemically bound GLYMO SAM in combination with patterned PLL structures on top leads to areas which are toxic (GLYMO) or biocompatible (PLL) for neurons. The results in terms of neuron adhesion and guidance of neuron growth are:

- In general, a strong neuron adhesion and healthy neuron growth on the PLL coated areas is observed, whereas on the areas with only GLYMO SAM no living neuron at all were observed. This proves the good quality of the GLYMO SAM, the (ethylene oxide)-terminated SAM is proven to be toxic for cells.
- Considering the neuron density based on pixel counting (≈ 70 k/cm^2) or based on counting by eye (≈ 60 k/cm^2), 24 - 28 % of the initial neurons (nominal seed density 250 k/cm^2) are alive at day in vitro 6 on PLL areas.
- After staining, the live-dead cell distribution is completely in perfect agreement with the pattern of biofriendly (PLL) and toxic (GLYMO SAM) areas. Therefore, guided neuron growth is observable in different formation (bars, squares, circles, triangles, etc.), for example for bars with a width of 100 µm even over distances of several millimeter.
- A slightly higher neuron density is observed at structural edges (or corners) which coincide as well with the observation higher PLL density at these positions. The higher PLL density at edges and corners is most likely an artefact of the patterning process. PLL is kept at these positions due to the PMMA and dries similar to the “coffee ring” in unpatterned areas (see Figure 45) (“coffee ring” effect).
- Furthermore, it can be stated that a “big coffee ring” structure of dried PLL is formed during the 1-hour wet coating process. The PLL drop shrinks and leaves a dried “big coffee ring”. The growth of neurons shows that structures close to that ring of dried PLL are preferred (Figure 70). By contrast, neuronal growth at the center of the test structure was barely noticeable which is in accordance with the assumption that the cracked PMMA molecules react and bind to the epoxy group of GLYMO and prevents therefore the chemically binding of PLL.

7 Summary

The general tasks in this work were as follows:

- to improve the existing molecular layer deposition (MLD) process by integrating a heater to the setup
- to design, create and prove a patterning method which allows guided cell growth
- to study the cell adhesion, the immobilization of neurons and guidance of neurite outgrowth on the patterned substrates

MLD

By integrating a heater to the deposition setup, the MLD process could be improved. The enhancement and optimization of the deposition temperature has led to an improvement of the gas phase deposition process of GLYMO yielding:

- a faster formation of SAMs (reduction of the PDT from 24 h to 1 h, even faster processes might possible) and
- a better quality of the resulting monolayer.

Generally, it could be shown that the process temperature plays a crucial role in the formation of silane SAMs. Similar to other organic molecular layers (see Figure 71 (b)), their stability and density depends strongly on the process temperature. With increasing deposition temperature their quality improves (Figure 71 (a)) up to an optimum at about 110°C, Above this temperature Si-C bonds in the GLYMO SAM are broken and only Si or C is deposited on the surface. This temperature behavior is similar to that shown in Figure 71 (b) for a thiol on gold.

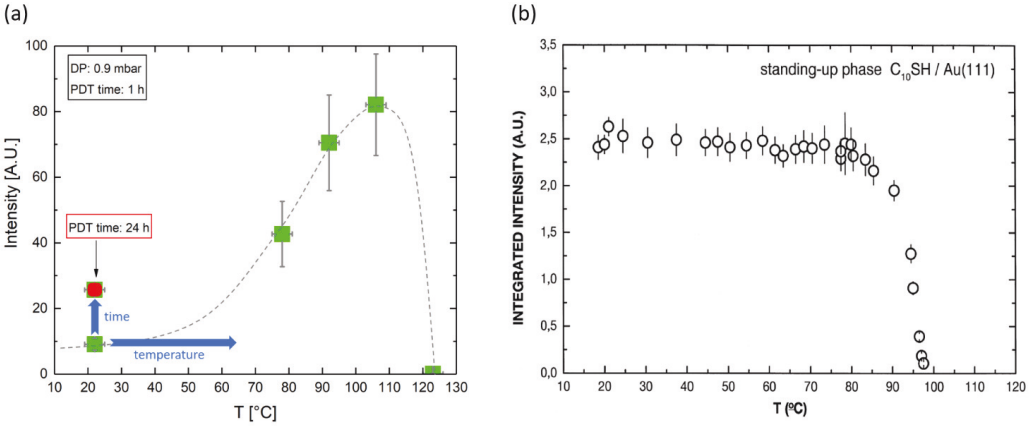

Figure 71: (a) Fluorescence intensity of the PLL/FITC marked GLYMO as a function of deposition temperature (dashed line guide for the eye). (b) Melting of decanethiol SAM on Au obtained from GIXD taken from [13].

Patterning Method

This extremely thin SAMs of GLYMO were then used to obtain a patterned surface that allows a directed cell growth (guided growth), using the toxic properties of GLYMO and the biocompatibility of PLL which can be bound to GLYMO. A pattering method was developed based on a combination of electron beam lithography and lift-off technique. The results obtained in this research are very promising:

- In order to bind PLL chemically on SSO substrates, GLYMO SAMs seems to be a perfect choice as linker interface to SiO_2. Furthermore, the PLL on GLYMO SAMs shifts the ζ potential positively by 10 mV to a stable final value of -10 mV which improves the cell adhesion. (In a physiological environment (ζ potentials ranging from −187 and +6 mV) increased surface potential promoted cell attachment and hence increased the initial cell density [25] [26].)
- With the pattering process introduced in this work we have proven that it is possible to create PLL patterns on GLYMO. The lithographical and lift-off process is particularly well suited for structures from 20 µm to 400 µm. Based on further investigation (via fluorescence microscopy) during the pattering process we assume that some cracked PMMA is left over on the GLYMO SAM which prevents the binding of PLL to the GLYMO.

Guided Neuron Growth

Finally, the guide grow is demonstrated on the GLYMO-PLL patterned structure.

In order to study the cell adhesion, the immobilization of neurons and guidance of neuron and neurite outgrowth according to the developed pattering process, cortical rat neurons were placed on the patterned substrates. The results (based on the analyzed neuron growth) demonstrated that the presented patterning process might be suitable to bio applications. Nevertheless, it also showed some shortcomings, especially that GLYMO seem to serve as an adhesive layer for cracked PMMA which prevents the binding of PLL. The neuron growth supported this assumption.

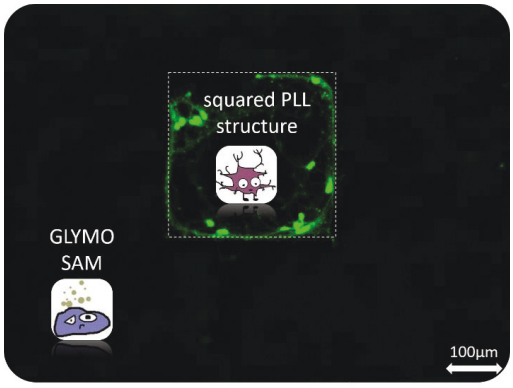

Figure 72: Images of a 900 µm x 670 µm area of a GLYMO coated and PLL patterned SSO substrate with cortical rat neurons, demonstrate the guided neuron growth in the PLL coated square.

The interface modification via a chemically bound GLYMO SAM in combination with patterned PLL structures on top leads to areas which are toxic (GLYMO) orbiocompatible (PLL) for neurons (see Figure 72). The results in terms of neuron adhesion and guidance of neuron growth are:

- A strong neuron adhesion and healthy neuron growth (≈ a third of the initial neuron density was alive at DIV 6) on the PLL associated structures is observed, whereas on the areas covered with a GLYMO nearly no living neurons were observed (which is another perfect proof for the good quality of the GLYMO SAM.).
- Guided neuron growth is observable in different formation and structures (bars, squares, circles, triangles, etc.) and could be realized in small bar structures in the micrometer range even over distances of several millimeter.
- The neuron distribution confirmed the previously observed PLL distribution and thus the assumption of undesired binding between the broken PMMA molecules and the epoxy group of GLYMO SAM (Figure 73).

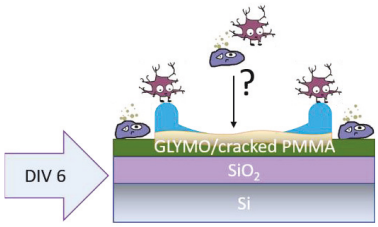

Figure 73: Sketch the neuron growth after DIV 6 on a GLYMO and PLL patterned sample. Neuron grow is mainly restricted to the edges ("coffee ring") of the structures and depending on the dimension of the structure.

A small Outlook

For prospective applications a slightly modified patterning process (according to process in section 3.5.1) might overcome the shortcoming connected to the layer of cracked PMMA which seems to block the binding of PLL and GLMO in the e-beam exposed areas (see Figure 74).

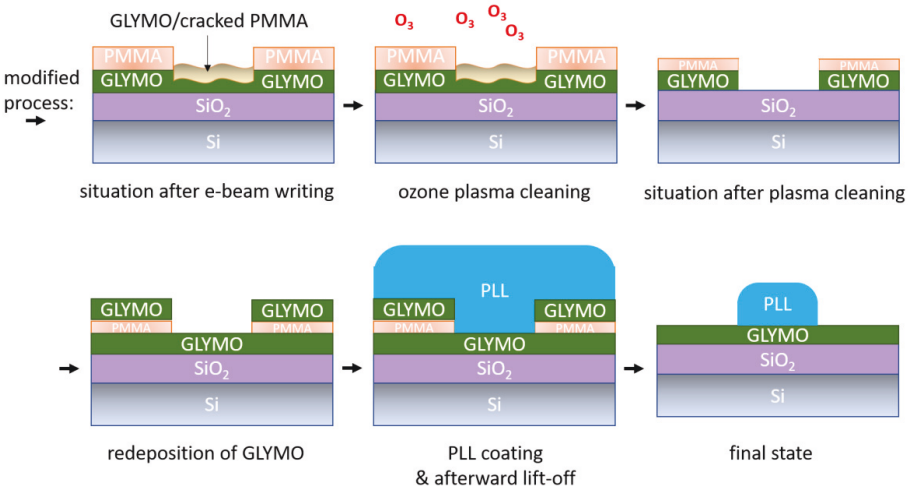

Figure 74: Schematic of the modified patterning steps which would allow to remove the cracked and bound PMMA molecules from the sample. And could lead to a perfect PLL-GLYMO pattern for guided neuron growth.

After electron lithography, an additional ozone plasma cleaning would remove the cracked and bound PMMA molecules and most likely the GLYMO molecules at the lithographic opened areas. These areas would be automatically activated again and a PLL coating would yield the desired bio compatible coating for the guided neuron growth. Unfortunately, the time was too short to test this promising recipe for obtaining a pattern with chemically bound thin PLL on GLYMO for guided cell growth.

8 References

[1] L. Hao, X. Fu, T. Li, N. Zhao, X. Shi, F. Cui, C. Du and Y. Wang, "Surface chemistry from wettability and charge for the control of mesenchymal stem cell fate through self-assembled monolayers," *ELSEVIER, Bd. Colloids and surfaces B: Biointerfaces,* pp. 549-556, 22 September 2016.

[2] S. Gilles, "Chemical Modification of Silicon Surfaces for the Application in Soft Lithography," Forschungszentrum Jülich, Jülich, 2007.

[3] R. G. Acres, A. V. Ellis, J. Alvino, C. E. Lenahan, D. A. Khodakov, G. F. Metha and G. G. Andersson, "Molecular Structure of 3-Aminopropyltriethoxysilane Layers Formed on Silanol-Terminated Silicon Surfaces," *The Journal of Physical Chemistry C,* pp. 6289-6297, 1 February 2012.

[4] D. Brian, B. Reddy, I. Block, P. Mathias, S. Clare, B. Cunningham and D. Bergstrom, "Vapor-Phase Deposition of Monofunctional Alkoxysilanes for Sub-Nanometer-Level Biointerfacing on Silicon Oxide Surfaces," *Birck and NCN Publications,* pp. 87-95, 28 December 2009.

[5] A. Cossaro, R. Mazzarello, R. Rousseau, L. Casalis, A. Verdini, A. Kohlmeyer, L. Floreano, S. Scandolo, A. Morgante, M. Klein and G. Scoles, "X-ray Diffraction and Computation Yield the Structure of Alkanethiols on Gold(111)," *Science,* pp. 943-946, 15 August 2008.

[6] M. Lessel, O. Bäumchen, M. Klos, H. Hähl, R. Fetzer, R. Seemann and K. Jacobs, "Self-Assembled Silane Monolayers: A Step-by-Step High Speed Recipe for High-Quality, Low Energy Surfaces.," *Surface and Interface Analysis,* p. 29–31, 17 April 2015.

[7] Y. Liang, J. Huang, P. Zang, J. Kim and W. Hu, "Molecular layer deposition of APTES on silicon nanowire biosensors: Surface characterization, stability and pH response," *Applied Surface Science Volume 322,* pp. 202-208, 15 December 2014.

[8] A. Markov, N. Wolf, X. Yuan, D. Mayer, V. Maybeck, A. Offenhäusser and R. Wördenweber, "Controlled Engineering of Oxide Surfaces for Bioelectronics Applications Using Organic Mixed Monolayers," *ACS Applied Materials & Interfaces,* pp. 29265-29272, 7 August 2017.

[9] E. Van den Berg, L. Bertilsson, B. Liedberg, K. Uvdal, R. Erlandsson, H. Elwing and I. Lundström, "Structure of 3-Aminopropyl Triethoxy Silane on Silicon Oxide.," *Journal of Colloid and Interface Science,* p. 147(1):103, 1991.

[10] R. Gross and A. Marx, Festkörperphysik, Berlin: De Gruyter, 1999.

[11] G. T. Hermanson, Bioconjugate techniques, third edition, Academic Press, 2013.

[12] D. Kim and A. E. Herr, "Protein immobilization techniques for microfluidic assays," *Biomicrofluidics,* 30 July 2013.

[13] F. Schreiber, "Structure and Growth of Self-Assembling Monolayers," *Progress in Surface Science,* pp. 151-256, 1 November 2000.

[14] S. Frank, "Structure and growth of self-assembling monolayers," *Progress in Surface Science,* pp. 151-257, December 2000.

[15] M. Zhu, M. Z. Lerum and W. Chen, "How To Prepare Reproducible, Homogeneous, and Hydrolytically Stable Aminosilane-Derived Layers on Silica," *Langmuir,* pp. 416 - 423, 10 January 2012.

[16] A. J. Worthen, V. Tran, K. Cornell, T. M. Truskett and K. P. Johnston, "Steric stabilization of nanoparticles with grafted low molecular weight ligands in highly concentrated brines including divalent ions," *Soft Matter,* pp. 2025-2039, 7 January 2016.

[17] A. N. Broers, A. C. F. Hoole and J. M. Ryan, "Electron beam lithography—Resolution limits," *Microelectronic Engineering - Elsevier,* pp. 131-142, 1 September 1996.

[18] Y. Dai, *Dissertation: Tailoring the Electronic Properties of Epitaxial Oxide Films via Strain for SAW and Neuromorphic Applications,* Jülich: Universität zu Köln, 2017.

[19] K. Greben, P. Li, D. Mayer, A. Offenhäusser and R. Wördenweber, "Immobilization and Surface Functionalization of Gold Nanoparticles Monitored via Streaming Current/potential Measurements," *J. Phys. Chem. B,* pp. 5988-5994, 23 April 2015.

[20] R. J. Hunter, Zeta Potential in Colloid Science: Principles and Applications, London: Academic Press, 1981.

[21] B. Thomas, R. F. Carver, R. D. Farlee and G. D. Stucky, "Solid-state silicon-29 NMR and infrared studies of the reactions of mono-and polyfunctional silanes with zeolite Y surfaces," *Journal of the American Chemical Society,* pp. 4546-4553, 1 July 1988.

[22] X. Yuan, N. Wolf, D. Mayer, A. Offenhäusser and R. Wördenweber, "Vapor-Phase Deposition and Electronic Characterization of," *Langmuir,* p. 8183−8190, 30 May 2019.

[23] M. Westwood, T. Noel and R. Parker, "The effect of poly-L-lysine structure on the pH response of polygalacturonic acid-based multilayers," *Carbohydrate polymers,* pp. 137-146, 15 April 2013.

[24] A. Markov, V. Maybeck, N. Wolf, D. Mayer and A. Offenhäusser, "Engineering of Neuron Growth and Enhancing Cell-Chip Communication via Mixed SAMs," *ACS Applied Materials & Interfaces,* pp. 18507-18514, 15 May 2018.

[25] W.-L. Kao, H.-Y. Chang, K.-Y. L. Y.-W. Lin and J.-J. Shyue, "ffect of Surface Potential on the Adhesion Behavior of NIH3T3 Cells Revealed by Quartz Crystal Microbalance with

Dissipation Monitoring (QCM-D)," *The Journal of Physical Chemistry C,* pp. 533-541, 01 12 2017.

[26] H.-Y. Chang, C.-C. Huang, K.-Y. Lin, W.-L. Kao, H.-Y. Liao, Y.-W. You, J.-H. Lin, Y.-T. Kuo, D.-Y. Kuo and J.-J. Shyue, "Effect of Surface Potential on NIH3T3 Cell Adhesion and Proliferation," *The Journal of Physical Chemistry C,* pp. 14464-14470, 10 06 2014.

[27] N. Wolf, In-situ Monitoring and Controlling the Growth of Organic Molecular Monolayers Using a Resistive Sensor, Jülich: Universität zu Köln, 2017.

[28] A. Markov, *Dissertation: Tailoring and characterisation of bioelectronic interfaces,* Universität zu Köln, 2017.

[29] V. Vito DePalma and T. Nolan, "Friction and wear of self-assembled trichlorosilane monolayer films on silicon," *Langmuir,* pp. 868-872, 1 May 1989.

[30] G. M. Laibinis and E. Paul, "Wet chemical approaches to the characterization of organic surfaces: self-assembled monolayers, wetting, and the physical-organic chemistry of the solid-liquid interface," *Langmuir,* pp. 87-96, 1 January 1990.

[31] M. A. Murphy, C. E. Nordgren, R. F. Fischetti, J. K. Blasie, L. J. Peticolas and B. J. C., "Structural Study of the Annealing of Alkylsiloxane Self-Assembled Monolayers on Silicon by High-Resolution X-ray Diffraction," *The Journal of Physical Chemistry,* pp. 14039-14051, 1 September 1995.

[32] J. Sagiv, “Organized monolayers by adsorption. 1. Formation and structure of oleophobic mixed monolayers on solid surfaces.,” *Journal of the American Chemical Society,* pp. 92-98, 1 January 1980.

[33] S. R. Wasserman, Y. T. Tao and G. M. Whitesides, "Structure and reactivity of alkylsiloxane monolayers formed by reaction of alkyltrichlorosilanes on silicon substrates," *Langmuir,* pp. 1074-1087, 1 July 1989.

[34] C. Mingyu, K. Gong, J. Li, G. Yandao, N. Zhao and Z. Xiufang, "Surface Modification and Characterization of Chitosan Film Blended with Poly-L-Lysine," *Journal of biomaterials applications,* pp. 59-75, 1 August 2004.

[35] D. O., B. M. and G. M., "Self-Assembly of n-Alkanethiols: A Kinetic Study by Second Harmonic Generation," *The Journal of Physical Chemistry B ,* pp. 2202-2213, 11 March 1999.

[36] M. Mehrali, S. Bagherifard, M. Akbari, A. Thakur, B. Mirani, M. Mehrali, M. Hasany, G. Orive, P. Das, J. Emneus, T. L. Andresen and A. Dolatshahi-Pirouz, "Blending Electronics with the Human Body: A Pathway toward a Cybernetic Future," *Advanced Science,* 01 August 2018.

Acknowledgements

This thesis is a summary of my work in Institute of Complex Systems (ICS-8) in Forschungszentrum Jülich.

Prof. Dr. Roger Wördenweber, a brilliant group leader, thank you for providing a platform for success in the academic environment. I appreciate the endless support that you offered me and the fact that you always see the positive part in any situation.

Prof. Dr. Öffenhäuser, the head of the institute, thank you for the organization of the working process, creating a convenient environment in ICS-8.

Nikolaus Wolf, my supervisor, thank you for all your patience, advices and support.

Rolf Kutzner, the engineer of our group, thank you for the technical support.

I appreciate the time spent in the group – Functional Oxides and Molecule – which were always open for discussions and created a pleasant working atmosphere. Therefore, I would like to express my thanks to *Dennis Finck*, *Sijia Liang* and *Xiaobo Yuan*.

The HNF-Facility thank for the use of devices and personal responsiveness when problems arise: *Research Center Juelich GmbH. (2017). HNF - Helmholtz Nano Facility. Journal of large scale research facilities, 3, A112. http://dx.doi.org/10.17815/jlsrf-3-158*

Band / Volume 201
Crystal structures and vibrational properties of chalcogenides: the role of temperature and pressure
M. G. Herrmann (2019), xi, 156 pp
ISBN: 978-3-95806-421-8

Band / Volume 202
Current-induced magnetization switching in a model epitaxial Fe/Au bilayer
P. Gospodarič (2019), vi, 120, XXXVIII pp
ISBN: 978-3-95806-423-2

Band / Volume 203
Network architecture and heme-responsive gene regulation of the two-component systems HrrSA and ChrSA
M. Keppel (2019), IV, 169 pp
ISBN: 978-3-95806-427-0

Band / Volume 204
Spin-orbitronics at the nanoscale: From analytical models to real materials
J. Bouaziz (2019), 228 pp
ISBN: 978-3-95806-429-4

Band / Volume 205
Advanced methods for atomic scale spin simulations and application to localized magnetic states
G. P. Müller (2019), xx, 194 pp
ISBN: 978-3-95806-432-4

Band / Volume 206
Different growth modes of molecular adsorbate systems and 2D materials investigated by low-energy electron microscopy
J. E. Felter (2019), vi, 114, XXXIV pp
ISBN: 978-3-95806-434-8

Band / Volume 207
NADPH-related studies performed with a SoxR-based biosensor in *Escherichia coli*
A. Spielmann (2019), IV, 73 pp
ISBN: 978-3-95806-438-6

Band / Volume 208
Chemisorption aromatischer Moleküle auf Übergangsmetalloberflächen: Bildung molekularer Hybridmagnete
S. Schleicher (2019), 109 pp
ISBN: 978-3-95806-442-3

Band / Volume 209
Regulatory interactions between *Corynebacterium glutamicum* and its prophages
M. Hünnefeld (2019), IV, 209 pp
ISBN: 978-3-95806-445-4

Band / Volume 210
Quantum Technology
Lecture Notes of the 51st IFF Spring School 2020
23 March – 03 April 2020, Jülich, Germany
ed. by H. Bluhm, T. Calarco, D. DiVincenzo (2020), ca. 700 pp
ISBN: 978-3-95806-449-2

Band / Volume 211
Interaction of physical fields with nanostructured materials
(2020), 255 pp
ISBN: 978-3-95806-450-8

Band / Volume 212
First-principles study of collective spin excitations in noncollinear magnets
F.J. dos Santos (2020), 270 pp
ISBN: 978-3-95806-459-1

Band / Volume 213
Direct measurement of anisotropic resistivity in thin films using a 4-probe STM
T. Flatten (2020), viii, 129 pp
ISBN: 978-3-95806-460-7

Band / Volume 214
The guided self-assembly of magnetic nanoparticles into two- and three- dimensional nanostructures using patterned substrates
W. Ji (2020), VI, 140 pp
ISBN: 978-3-95806-462-1

Band / Volume 215
Molecular layer deposition and protein interface patterning for guided cell growth
M. Glass (2020), iv, 81 pp
ISBN: 978-3-95806-463-8

Weitere ***Schriften des Verlags im Forschungszentrum Jülich*** unter
http://wwwzb1.fz-juelich.de/verlagextern1/index.asp

Schlüsseltechnologien / Key Technologies
Band / Volume 215
ISBN 978-3-95806-463-8

Mitglied der Helmholtz-Gemeinschaft

JÜLICH
Forschungszentrum